
DISS. ETH No. 18947

Controlled Single-Walled Carbon Nanotube Growth for Sensing Applications

A thesis submitted to the
ETH ZURICH

for the degree of
DOCTOR OF SCIENCES

presented by

Lukas Durrer

MSc. Chem., University of Bern

born March 14th 1978

Citizen of Switzerland

Prof. Dr. C. Hierold, examiner

Prof. Dr. László Forró co-examiner

Zurich, 2010

to my wife Roswitha,
who supported me during the whole PhD

Abstract

Single-walled carbon nanotubes (SWNTs) are tubular molecules with diameters between 0.4nm and 4nm and lengths from a few nm up to several tenths of microns. SWNTs consist only of carbon atoms arranged in a single layer honeycomb lattice structure which is wrapped around onto it to form a tube. These molecules were discovered by Sumio Iijima in 1991 and show exceptional mechanical, electrical and electromechanical properties, making them promising candidates for future applications: as transducers in chemical, biochemical, and electromechanical sensors, as interconnects and transistors in computer chips, and as stabilizer in composite materials.

A major impediment to the introduction of SWNTs to these technologies is the lack of reproducibility in SWNT-based device production and in SWNT synthesis. Particularly, the production of SWNT-based field effect transistors (CNFETs) with reproducible threshold values or off-state potentials, on-state currents, and on- to off-state ratios would be required.

With the aim to improve device production for sensing applications, the focus must be on the growth of absolutely clean and straight individual SWNTs of low structural defects, with a controlled diameter of around 2 nm (for ohmic contacts to Pd which is the best suited contact metal), a narrow diameter distribution (for band gap control), and a controlled site density. Furthermore integration processes are required that do not damage or contaminate the SWNTs in any way.

Of great importance is also the development of a batch SWNT integration processes that can give high yields of single-bridging individual SWNTs. The current integration processes suffer from many problems including integration control, the production of CNFETs with high quality contacts and the applicability for standard MEMS batch processing.

This thesis focuses on the controlled growth of SWNTs by chemical vapor deposition (CVD) and on the development of a batch integration process based on standard UV lithography for the production of high quality CNFETs that consist of individual SWNTs to be used for sensing applications.

Using the Fe storage protein ferritin for catalyst preparation and by optimizing the CVD growth parameters, it was possible to grow clean SWNTs on 200nm thick silicon gate oxide. The control of the ferritin density on the SiO₂ surfaces was achieved by adjusting the concentration of the ferritin in the solution from which these proteins were adsorbed onto

the SiO₂ surface. In this manner, it was possible to control the resulting SWNT density on the surface, enabling the growth of only individual SWNTs. It is known that the SWNT diameter depends on the size of the catalyst diameter. Therefore SWNTs with controlled diameters were grown by controlling the size of the catalyst nanoparticles: first by adjusting the duration of the catalytic loading of iron into ferritin, and subsequently by velocity centrifugation of iron-loaded ferritin proteins, thus separating the proteins according to the amount of loaded Fe in their core. Using these size-controlled proteins for catalyst nanoparticle formation, SWNTs were grown with narrow diameter distributions (~0.3nm) at the desired mean diameters (~2nm). Furthermore, the narrow diameter distribution enabled the growth of purely straight SWNTs because according to their stiffness SWNTs with diameters >0.9nm are straight while SWNTs with diameters <0.9nm are often curved.

A batch integration process based on standard UV lithography was developed, which results in the integration mainly single-bridging individual SWNTs with an integration yield of 22% (only 2.5% double bridging events, 1.5% multiple bridging events and 2.5% bridged SWNT bundles were observed). To build upon the achievements in controlled SWNT growth described above, this process was founded on the patterning of ferritin-based catalysts and the subsequent growth of SWNTs from these structured growth islands in random directions. Therefore, the integration yield of single-bridging individual SWNTs can be tuned by the SWNT density. The SWNTs were contacted by structuring electrodes on top of each growth island. To enable low contact resistances, a special UV lithography process was investigated resulting in residual free electrode patterns that provide undisturbed contacts of the SWNTs to the contact metals. Electrical measurements of clean SWNTs with a mean diameter of 2.1nm ±0.32nm integrated by the developed process showed reproducibility in the off-state potential (threshold value) of CNFETs. This result is mainly related to the cleanliness of the SWNTs in combination with an annealing step and subsequent device protection from environmental influences by atomic layer deposited Al₂O₃. The electrical measurements showed that the off-state potential value is independent of the SWNT band gap, at least for large diameter SWNTs. This suggests that the chirality is only of minor importance for the production of reproducible CNFETs from semiconducting or small band gap semiconducting SWNTs.

Zusammenfassung

Einwandige Kohlenstoffnanoröhrchen (SWNTs) sind rohrförmige Moleküle mit Durchmessern zwischen 0.4nm und 4nm und können Längen von ein paar Nanometern bis mehreren Millimetern aufweisen. SWNTs bestehen ausschliesslich aus Kohlenstoff-Atomen, welche zu einer einschichtigen wabenförmigen Struktur zusammengereiht und zu einer Röhre geformt sind. Diese Makromoleküle wurden 1991 von Sumio Iijama entdeckt und weisen aussergewöhnliche mechanische, elektrische und elektromechanische Eigenschaften auf. Auf Grund dieser Eigenschaften sind SWNTs vielversprechende Bausteine für zukünftige Anwendungen. Vor allem als Sensorelemente in biochemischen-, chemischen- und elektromechanischen Sensoren, als Verbindungsdrähte und Transistoren für Computerchips und als Stabilisatoren in neu entwickelten Materialien werden SWNTs als vielversprechend beurteilt.

Der Hauptgrund dass SWNTs noch nicht in diesen Produkten zum Einsatz kommen, ist die schlechte Reproduzierbarkeit in der Herstellung von SWNT Bauelementen und in der Synthese von SWNTs. Insbesondere das Herstellen von SWNT Feldeffekttransistoren (CNFETs) mit reproduzierbaren Schwellenspannungen und reproduzierbaren Verhältnissen von Strömen im „an“ und „aus“ Zustand wäre von Nöten.

Um dem Ziel der reproduzierbaren Herstellung von CNFETs für Sensoranwendungen etwas näher zu kommen, wäre es wichtig, saubere, gerade und einzelne SWNTs, welche nur geringe Strukturfehler aufweisen, herzustellen. Sie sollten mit einem kontrolliertem Durchmesser von 2nm (das ist wichtig für ohmsche Kontakte zu Pd, dem zurzeit besten Material zur Kontaktierung von SWNTs), mit geringer Streuung des Durchmessers (für die Kontrolle der Bandlücke) und mit kontrollierter Dichte des Wachstums auf der Oberflächen zu synthetisieren sein. Zusätzlich müssten Integrationsprozesse, welche keine Fehler in der Struktur (Defekte) und Verunreinigungen auf der Röhre verursachen, entwickelt werden.

Ebenfalls von grosser Wichtigkeit ist die Entwicklung eines skalierbaren Integrationsprozesses mit einer hohen Ausbeute an CNFETs, bestehend aus einer einzelnen SWNT als Kanal. Die zurzeit bekannten Integrationsprozesse weisen Mängel wie zu geringe Integrationskontrolle oder zu hohe Kontaktwiderstände auf oder sind nicht massenanfertigungstauglich.

Diese Doktorarbeit fokussiert auf das kontrollierte Wachstum von SWNTs mittels chemischer Gasphasenabscheidung (CVD) und in einem zweiten Teil auf einen neuartigen Integrationsprozesses, welcher auf Standardlithographie (DUV) aufbaut. Dieser Prozess

sollte die Massenanfertigung von qualitativ hochwertigen CNFETs, die zum grössten Teil aus einer einzelnen SWNT bestehen, für Anwendungen als Sensoren ermöglichen.

Durch die Benützung des eisenoxidspeichernden Proteins Ferritin zur Präparation von Nanopartikeln, welche der Katalyse der Dissoziation von Kohlenwasserstoffen dienen, und durch die Optimierung der CVD Wachstumsparameter wurde es möglich, absolut saubere SWNTs auf 200nm dickem Gateoxid zu wachsen. Durch die Kontrolle der Ferritindichte auf der SiO₂ Oberfläche über die Konzentration der Lösung, von welcher das Ferritin absorbiert wird, war es möglich, die SWNT Dichte auf der Oberfläche zu kontrollieren. Durch eine drastische Reduktion der SWNT Dichte konnte das Wachstum von ausschliesslich einzelnen SWNTs beobachtet werden. Es ist bekannt, dass der SWNT Durchmesser stark von der Grösse des Katalysatornanopartikels abhängt. Durch die Herstellung von Katalysatoren mit kontrollierten und unterschiedlichen Grössen, welche über die Ladezeit des Ferritins variiert wurden, konnten SWNTs mit kontrollierten Durchmessern hergestellt werden. Durch die Einführung einer neuen Methode, bei der Ferritin aufgrund der Grösse des geladene Eisenoxidpartikels separiert wird, konnten Katalysatornanopartikel mit kleinen Durchmesserverteilungen gewonnen werden. Das bewirkte, dass die SWNT Durchmesserverteilungen für SWNTs auch mit grösseren Durchmessern um die 2nm drastisch reduziert werden konnten. Für SWNTs mit Durchmessern um die 2nm konnten Durchmesserverteilungen um die 0.3nm erreicht werden. Dieses Resultat bewirkte auch das selektive Wachstum von geraden SWNTs. Es wurde auch beobachtet, dass SWNTs mit Durchmessern, die grösser als 0.9nm sind, gerade wachsen, wahrscheinlich bedingt durch ihre Steifheit.

Es wurde ein Integrationsprozess zur Massenfertigung von CNFETs, hauptsächlich bestehend aus einzelnen SWNTs unter Anwendung von DUV-Lithographie, entwickelt. Eine Integrationsausbeute von 22% von SWNT Transistoren mit nur einer Nanotube wurde gemessen (die Ausbeute an Transistoren bestehend aus 2 SWNTs war nur 2.5%, aus 3 SWNTs war 1.5% und aus SWNT Bündel war 2.5%). Um die hohe Qualität der Wachstumskontrolle aufrechtzuerhalten, gründet dieser Prozess auf dem Wachstum von SWNTs von vorstrukturierten (Lift-Off) Ferritin-Inseln an vordefinierten Stellen. Dadurch kann die Integrationsausbeute über die SWNT Dichte kontrolliert werden. Die SWNTs wurden dann durch die Strukturierung von Elektroden auf diesen Wachstumsinseln kontaktiert. Ein spezieller DUV Lithographieprozess ermöglichte es, Kontaktstrukturen im Photolack zu generieren, welche frei von Photolack-Rückständen waren, was eine optimale Kontaktierung ohne Blockaden durch Verunreinigungen von der SWNT zum Kontaktmetall ermöglichte.

Statistische Auswertungen von elektrisch gemessenen CNFETs welche durch die entwickelte Methode hergestellt wurden, zeigten, dass die Schwellenspannung reproduzierbar ist. Dieses Resultat basiert vor allem auf der Verwendung von absolut sauberen SWNTs in Kombination mit einer Temperung und dem anschliessendem Abscheiden einer Al₂O₃ Schutzschicht mittels Atomlagenabscheidung (ALD). Es hat sich

herausgestellt, dass die Bandlückengrösse keinen Einfluss auf die Schwellenspannung hat. Daraus wird geschlossen, dass die Kontrolle der Chiralität der SWNT nur eine geringe Rolle bei der reproduzierbaren Herstellung von CNFETs aus halbleitenden SWNTs hat.

Contents

Abstract.....	i
Zusammenfassung	iii
Contents	vi
List of Abbreviations and Symbols	viii
1 Introduction	1
1.1 CARBON NANOTUBES: DEFINITION, PROPERTIES AND APPLICATIONS	2
1.1.1 Definition.....	2
1.1.2 Properties	3
1.1.3 Applications.....	4
1.2 SINGLE-WALLED CARBON NANOTUBES FOR SENSING APPLICATIONS.....	5
1.2.1 Sensing based on the Fermi level shift in a SWNT-based Field effect transistor (CNFET)	6
1.2.2 Piezoresistive sensing due to straining SWNT in nano electromechanical systems (NEMS).....	7
1.2.3 Challenge of using SWNTs for sensing applications.....	8
1.3 REQUIREMENTS ON THE SWNT MATERIAL FOR THE USE IN SWNT-BASED SENSORS.....	11
1.3.1 Synthesis of SWNTs that are free of contaminations	12
1.3.2 Control of the SWNT type.....	13
1.3.3 Synthesis of straight SWNTs.....	14
1.3.4 Synthesis of individual SWNTs.....	14
1.3.5 Control of the SWNT density	16
1.3.6 Synthesis of SWNTs with controlled average diameter and narrow diameter distribution	17
1.3.7 Control of the SWNT position and alignment for large scale SWNT integration.....	23
1.4 OBJECTIVES	27
2 Theory.....	28
2.1 STRUCTURAL PARAMETERS OF SWNTS.....	28
2.2 ELECTRICAL TRANSPORT IN SWNTS	30
2.2.1 Electronic properties of SWNTs.....	30
2.2.2 SWNT based field effect transistors (CNFET).....	31
2.3 SWNT SYNTHESIS	35
2.3.1 SWNT synthesis techniques	35
2.3.2 SWNT growth model.....	39
2.3.3 Thermodynamic and kinetic considerations in SWNT growth.....	42
2.3.4 Ferritin: A protein helps to form the catalyst nanoparticle	43
3 Experimental.....	46
3.1 GENERAL CONSIDERATIONS.....	47
3.2 SUBSTRATE PREPARATION	49

3.3	CATALYST PREPARATION	50
3.4	CATALYST SIZE SEPARATION	52
3.5	SWNT GROWTH	54
3.6	SWNT INTEGRATION BY E-BEAM LITHOGRAPHY, METAL EVAPORATION AND LIFT-OFF	56
3.7	CATALYST ISLANDS AND ELECTRODE PAD STRUCTURING BY UV LITHOGRAPHY AND LIFT-OFF	56
3.7.1	Alignment markers	57
3.7.2	Patterning of catalyst islands and growth of SWNTs from these islands	58
3.7.3	Structuring of the electrodes	59
3.7.4	Post-treatments	60
3.8	ANALYSIS	61
3.8.1	AFM	61
3.8.2	SEM and TEM	61
3.8.3	Raman spectroscopy	62
3.8.4	Transistor measurements	62
4	Results and discussions	65
4.1	GROWTH OF STRAIGHT, CLEAN AND INDIVIDUAL SWNTS	65
4.1.1	SWNTs grown from ferritin based catalyst nanoparticles	65
4.1.2	Control of the SWNT density	71
4.1.3	CNFETs-based on SWNTs grown from ferritin-based catalyst nanoparticles	73
4.1.4	Discussion	75
4.2	SWNT DIAMETER CONTROL AND NARROWING SWNT DIAMETER DISTRIBUTION	81
4.2.1	Controlling the mean SWNT diameter by the loading time of the ferritin proteins	81
4.2.2	Narrowing SWNT diameter distribution using size-separated ferritin-based Fe catalysts	82
4.2.3	Discussion	88
4.3	BATCH INTEGRATION OF INDIVIDUAL SWNTS BY UV LITHOGRAPHY	90
4.3.1	Design	90
4.3.2	Growth of SWNTs from structured catalyst islands	93
4.3.3	Integration yield	94
4.3.4	Production of CNFETs with low contact resistance	99
4.3.5	Production of CNFETs with reproducible off-state potentials (threshold values)	101
4.3.6	Discussion	105
5	Conclusions and Outlook	111
6	Appendix	114
6.1	NOVEL QUANTITATIVE MODEL BASED ON THERMODYNAMIC AND KINETIC CONSIDERATIONS FOR SWNT GROWTH	114
6.1.1	Determination of the model	115
6.1.2	Discussion	120
6.1.3	Conclusion	122
	Bibliography	124
	Acknowledgments	141
	Publications	142
	Curriculum Vitae	146

List of Abbreviations and Symbols

Abbreviations:

3D	Tree dimensional
a-C	Amorphous carbon
ads	adsorbed
AFM	Atomic force microscope
ALD	Atomic layer deposition
chemFET	Chemical Field effect transistro
CMOS	complementary metal–oxide–semiconductor
CNFET	Single-walled carbon nanotube –based field effect transistor
CNT	Carbon nanotube
CVD	Chemical vapour deposition
DOS	Densities of states
DWNT	Double-walled carbon nanotube
FET	Field effect transistor
g	Gaseous
HuHf	human Hanukah factor
HiPCO	High-pressure CO conversion
HRTEM	High resolution transmission microscope
ICP	Inductively coupled plasma
IT	Information technology
LPCVD	Low pressure chemical vapour deposition
MEMS	Micro electromechanical system
MOCVD	Metal organic chemical vapor deposition
MWNT	Multi-walled carbon nanotube
m-SWNT	Metallic single-walled carbon nanotube
NEMS	Nano electromechanical systems
PMMA	Polymethyl methacrylate
PVD	Physical vapor deposition
PVP	pPolyvinylpyrrolidone
RH	Relative Humidity
SB	Schottky barrier

SDS	Sodium dodecyl sulphate
SDBS	Sodium dodecylbenzene sulphonate
SEM	scanning electron microscopy
SGS-CNFET	Field effect transistor consisting of a small-gap-semiconducting SWNT
SGS-SWNTs	Small-gap semiconducting single-walled carbon nanotubes
s-CNFET	Field effect transistor consisting of a semiconducting SWNT
s-SWNT	Semiconducting single-walled carbon nanotube
SWNT	Single-walled carbon nanotube
TEM	Transmission electron microscope
UV	Ultra violet

symbol	unit	description
a_1 and a_2		Unit vectors
a_{c-c}	0.124nm	C-C bond length
a	Mol/l	Activity
A	Reaction dependent	prefactor
A	m ²	Area
C	Mol/l	concentration
C_h		Chiral vector
d	m	Diameter
e	1.602×10^{-19} C	Elementary charge
E_a	kJ/mol	Activation energy
E_g	eV	Band gap
E	J	Energy
E_F	J	Fermi-level
ϕ_{SB}	eV	Schottky Barrier
F	C/mol	Faraday constant
ΔG	J/mol	Gibbs free energy
ΔG^*	J/mol	Standard Gibbs free energy
ΔH	J/mol	Enthalpy
h	6.626×10^{-34} J·s	Planck constant
I	A	Electrical current
I_{on}	A	On-state current
I_{off}	A	Off-state current
I_{sd}	A	Source-drain current
j		Integer $j=0,1,2,3,\dots$
k	Mol ⁻¹ s ⁻¹	Kinetic constant

List of Abbreviations and Symbols

k_b	1.380 J/K	Boltzmann constant
l	l	Liter
L	m	length
M	Mol	Molar mass
(m,n)		Chiral indices
N_A	1/mol	Avogadro constant
P	bar	Pressure, partial pressure
P	W	Power
Q	C	Total charge
R	8.314J/Kg/mol	Gas constant
q	C	Charge of carrier
R	Ω	Electrical resistance
ΔS	J/mol	Entropy
t	s	Time
T		Transition vector
T	K	Temperature
U	V	Voltage
V_b	V	Bias voltage
V_G	V	Gate voltage
V_{sd}	V	Source-drain voltage
ρ	Ωm	resistivity
σ	S/m	electrical conductivity
ϕ	V	electric potential

1 Introduction

“The steel of Damascus blades, which were first encountered by the Crusaders when fighting against Muslims, had features not found in European steels — a characteristic wavy banding pattern known as damask, extraordinary mechanical properties, and an exceptionally sharp cutting edge.

By empirically optimizing their blade-treatment procedure, craftsmen ended up making nanotubes more than 400 years ago. Thermal cycling and cyclic forging below the cementite formation temperature (about 800°C) cause catalytic elements to segregate gradually into planar arrays parallel to the forging plane. These elements may give rise to the growth of carbon nanotubes. [1]”

This discovery published in Nature magazine, highlights one of many exceptional material properties of carbon nanotubes (CNTs). CNTs are tubular molecules, consisting only of carbon atoms, with diameters in the nanometer regime and lengths up to several micrometers. Due to their extremely high strength, these macromolecules are used today as they were 400 years ago, as additives in materials to increase their mechanical stability. Beside the good mechanical properties, CNTs have exceptional electrical and electromechanical properties [2]. Therefore, they are considered for many potential applications. Micro and Nanosystems group at the ETH Zurich is developing the use of CNTs for sensing applications. For this purpose, the integration of CNTs in electrical and nanoelectromechanical systems (NEMS), and their capability as transducers, are investigated. For the fabrication of high performance CNT-based sensors, the CNTs themselves need to be of high quality. In particular, synthesis of CNTs with controlled and reproducible properties is necessary. Producing CNTs which can be integrated in sensor systems resulting in high quality device properties is the main scope of this thesis. Like the craftsmen used to do 400 years ago, the CNTs are synthesized at 850°C by using Fe as catalyst material. Fe catalyzes the dissociation of the carbon feed stock gas resulting in pure carbon atoms, which are rearranged in a growing CNT. This synthesis method is called chemical vapour deposition (CVD). However, unlike 400 years ago, where the material was developed just by trial and error, high tech analysis methods like atomic force microscopy (AFM), scanning electron microscopy (SEM), transmission electron microscopy (TEM) and Raman spectroscopy, which allow analyzing the material in the nanometer range, were used for process optimization in this work.

The introduction starts, with the definition, the specification and the description of the properties of CNTs. Then the use of SWNTs for sensor applications is discussed, which

leads to the determination of the requirements for producing high quality CNT-based sensors, from which the objectives of the thesis are determined.

1.1 Carbon Nanotubes: Definition, Properties and Applications

1.1.1 Definition

CNTs were first discovered by Iijima in 1991 [3]. He analyzed arc-discharge products by transmission electron microscopy (TEM) and found beside other carbon molecular products also tubular molecules consisting of several carbon shells, which were named multi-walled carbon nanotubes (MWNTs). Two years later, the synthesis of single-wall carbon nanotubes (SWNTs) was reported [4-5]. SWNTs consist only of one carbon layer wrapped into a tube. The third type of CNT consists of two carbon sidewall layers, and is therefore a double-walled carbon nanotube (DWNT). The structures of the three types of CNTs are shown in Figure 1.1. The molecular unit of the CNT is a benzene ring. These rings are assembled to a honeycomb structure (a graphene sheet) which is wrapped into a cylinder.

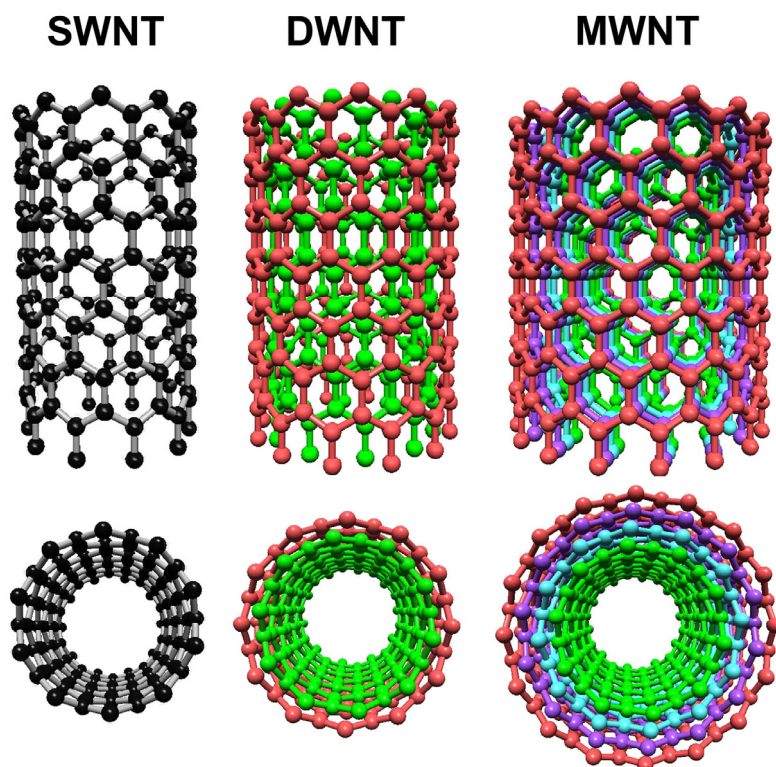


Figure 1.1: Molecular structure of the three different types of CNTs. SWNTs consist of one (single) carbon layer, DWNTs of two and MWNTs of multiple carbon layers.

1.1.2 Properties

As already mentioned, CNTs have outstanding characteristics. The most impressive properties of MWNTs and SWNTs, and their comparison with materials well known for their desired properties for particular applications, are listed in Table 1.1.

Beside the high aspect ratio and the high surface to volume ratio, CNTs have a Young's modulus which are 5 to 10 times higher than that of steel combined with a tensile strength 20 to 50 times higher than steel. This means, a CNT is at least 5 times harder, and it can withstand 20 times more stress than steel before it breaks.

The thermal conductivity is a factor 3 to 5 higher than Cu, which is the material mainly used in applications where high thermal conductivities are required.

Most promising are the electrical properties of CNTs. They show current densities which are 100 to 1000 times higher than today's best monocrystalline Au nanowires with a similar radius. Additionally two third of the SWNTs are semiconducting, and can therefore be used for CNT-based transistors.

Last but not least, SWNTs show extremely high gauge factors. This factor is a measure of the change of the resistance due to straining of the material. Measured gauge factors are by a factor 2 to 4 higher than the best known common piezoresistive semiconducting materials [6]. Extractions from measurements of prestrained and suspended SWNTs show gauge factors, which are even 10 times higher [7].

Table 1.1: Properties of carbon nanotubes

	MWNT	SWNT	comparison
Mechanical properties			
Young's modulus	~1.8TPa [8]	~1TPa [8]	~0.2TPa (Steel) [9]
Tensile strength	~50GPa [9]	~150GPa [9]	~2.5GPa (Steel) [9]
Thermal property			
Thermal conductivity	~1400W/K/m[10]	~2400W/K/m [10]	401W/K/m (Cu) [11]
Electrical properties			
Current density	$2 \cdot 10^{10}$ A/cm ² [12]	$1 \cdot 10^9$ A/cm ² [13]	$2.5 \cdot 10^7$ A/cm ² (Au wire, $\varnothing=9$ nm) [14]
Semiconducting properties	No (conducting)	Yes (2/3 of all the SWNTs are semiconducting) [15]	-
Electromechanical property			
Gauge factor	~50 [16] (MWNT films)	600-1000 [17]	80-200 (doped semiconductors) [17]

1.1.3 Applications

Considering these outstanding properties, it is not surprising that the discovery of carbon nanotubes initiated a wave of enthusiasm in research and industry. There are countless possible applications for this material. The most important fields of applications are shown in Table 1.2.

Table 1.2: The exceptional properties of CNTs result in many potential applications

	Principle	Required material properties	Examples	Ref.
Field-emitter	Emission of electrons from a sharp tip by applying an electrical field.	-High aspect ratio -High current density	-Flat panel displays -Electron Microscopy	[18]
Composite material	Mixing of CNTs with polymers or other materials to improve the stability, conductivity, or weight of the material.	-High aspect ratio -Low weight -High mechanical stability -High conductivity	-Automotive, Airplane -Sport equipment -Conductive polymers	[9]
Field-effect transistor	On-off switch of semiconducting SWNTs due to an electrical field	-High aspect ratio -Semiconducting properties -Diameter below 10nm	-Computer processors	[19] [20]
Interconnects	Electrical connections between transistors.	-High aspect ratio -Diameter below 10nm -High current densities	-Computer processors	[19]
Sensors	Detection due to changes in the electrical resistivity	-High surface to volume ratios -Mechanical and chemical stability -Transducer capabilities (high gauge factor, FET, chemo-resistor, etc)	-NO ₂ sensor -Cancer diagnostic -Pressure sensor	[21] [22] [23]

Vertically aligned CNTs have the perfect shape for field emission [18]. Even a weak electric field is sufficient make electrons to propagate from the CNT tip. This technique could lead to low power flat panel displays or low power electron microscopes.

So far, the only conventional application of CNTs is their use in composite materials. In 2005, the first bicycles made of materials containing CNTs were built by the Swiss company BMC and introduced by the Phonak team at the Tour de France [24].

To comply with the information technology (IT) roadmap, the features on semiconducting chips should become smaller than 15nm until 2020 [19]. Therefore, the IT industry puts a lot of hope in nanotechnology, particularly in CNTs for the use as interconnects and as transistors. For example, researchers from IBM have already succeed in building a ring oscillator based on CNTs [20].

The high surface to volume ratio, the high sensitivity of SWNTs to strain as well as the high sensitivity of semiconducting SWNTs (s-SWNTs) to an external electrical field, make them very interesting for sensing applications [23]. Since this thesis focuses on the production of CNTs for sensors, this topic will be described in more detail in the next chapter.

1.2 Single-Walled Carbon Nanotubes for Sensing Applications

Sensors transform physical, chemical or biological environmental conditions into a quantitative output signal [25]. In most cases, the output signal is an electrical signal. The element which fulfills the transformation is called a transducer. Today's life is aided by an immense number of sensors. The main sensor application field are: automotive, manufacturing quality and process control, aerospace, medical and healthcare and environmental monitoring [26]. Customer's demand for sensors which are smaller, cheaper, more sensitive and/or have a lower power consumption, is increasing. Many of these needs could be fulfilled by using nanomaterials. However defects in molecular or crystalline structures can no longer be neglected due to the less dominant bulk properties with the entrance into the nanometer regime. Therefore, downscaling of transducers to the nano regime requires materials with exceptional mechanical properties and chemical inertness. Additionally, in order to achieve a high sensitivity in chemical sensing, transducers having high surface to volume ratios and showing strong transduction capabilities due to molecular adsorption, are needed. For piezoresistive sensors, high gauge factors are required. According to the properties discussed in chapter 1.1.2, SWNTs fulfill all these demands and are therefore optimal for nanoscale size transducers.

Following, the basic principle of sensing due to a shift of the Fermi level or changes of the resistivity are shown and explained through examples. Further, the problems and challenges of producing SWNTs devices in general, and SWNT devices for sensing applications in particular, are discussed.

1.2.1 Sensing based on the Fermi level shift in a SWNT-based Field effect transistor (CNFET)

Micro machined field effect transistors for chemical sensing applications (chemFETs) are well known and investigated thoroughly [25]. The basic sensing principle of conventional FET sensors and CNFETs is similar [27]. However, CNFETs have the potential of being more sensitive, smaller and having lower energy consumption than conventional chemFETs. Figure 1.2 shows the effect of NO_2 adsorption on a CNFET as an example for the transducing principle of CNFET-based sensors [28]. Figure 1.2 a) shows a state-of-the-art CNFET architecture for sensing investigations and applications consisting of one individual s-SWNT contacted by a source and a drain electrode. In this particular case, a back gate configuration is presented with a 200nm thick gate oxide lying between the tube and the gate. Investigations have shown that the coating of the device by Al_2O_3 decreases hysteresis effects, noise, and prevents the contacts from oxidizing, which improves the long-term stability [29]. When this device is exposed to polar molecules such as NO_2 , they adsorb on the SWNT surface and cause a shift of the Fermi level (Figure 1.2 b). [28, 30-31]. This shift results in a detectable shift of the threshold voltage in the CNFET device characteristics (Figure 1.2 c).

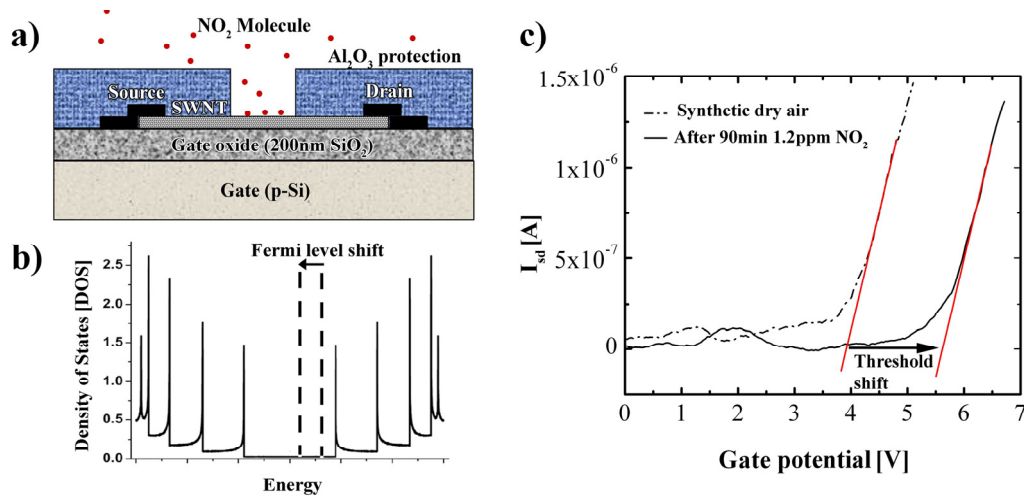


Figure 1.2: Sensing principle for CNFET-based sensors. a) The state-of-the-art CNFET setup for the investigation of CNFET based sensing. b) Density of states of a s-SWNT (Van Hove singularities). c) CNFET Gate sweep characteristics prior and after exposure to NO_2 . When polar molecules adsorb on the s-SWNT surface a) an electrical field is implemented by this molecules, which leads to a shift of the Fermi level b). This causes a shift in the threshold voltage of the CNFET c) [28, 30].

CNFETs are highly sensitive to wide range of chemical [32] and biochemical [22] molecules, and are therefore promising candidate for future diagnostic and gas sensing applications.

For example, it has been shown that it is possible to detect NO_2 concentrations in the ppm regime (see Figure 1.2 c). This sensitivity is comparable to state-of-the-art metal-oxide-semiconducting NO_2 sensors used in fire detectors. However, CNFETs work at room temperature, while the conventional sensors have to be operated at elevated temperatures. By attaching bimolecular linkers to SWNTs, they become capable for enzyme-linked immunoadsorbent assay (ELISA) diagnostics. For example, detection of tumor markers in the pg/ml regime has been shown and could allow early cancer diagnostic in future [33].

1.2.2 Piezoresistive sensing due to straining SWNT in nano electromechanical systems (NEMS)

Here, the principle of sensing strain [34] is explained by the example of a SWNT-based pressure sensor shown in Figure 1.3 [6, 35-36]. A metallic SWNT (m-SWNT), with a channel length L_o lying on an atomic layer deposited (ALD) membrane, is contacted by a source and a drain electrode (a). When a pressure is applied, the membrane is bulged (c), and the tube on the membrane is strained to the length $L_o + \Delta L$ (a). This results in a breaking of symmetry in the m-SWNT structure. The π -orbitals in a m-SWNT overlap each other. Straining the SWNT changes the symmetry and results in fewer overlapping π -orbitals. Hence, a small band gap is formed (b), which results in a detectable change of the resistance (d).

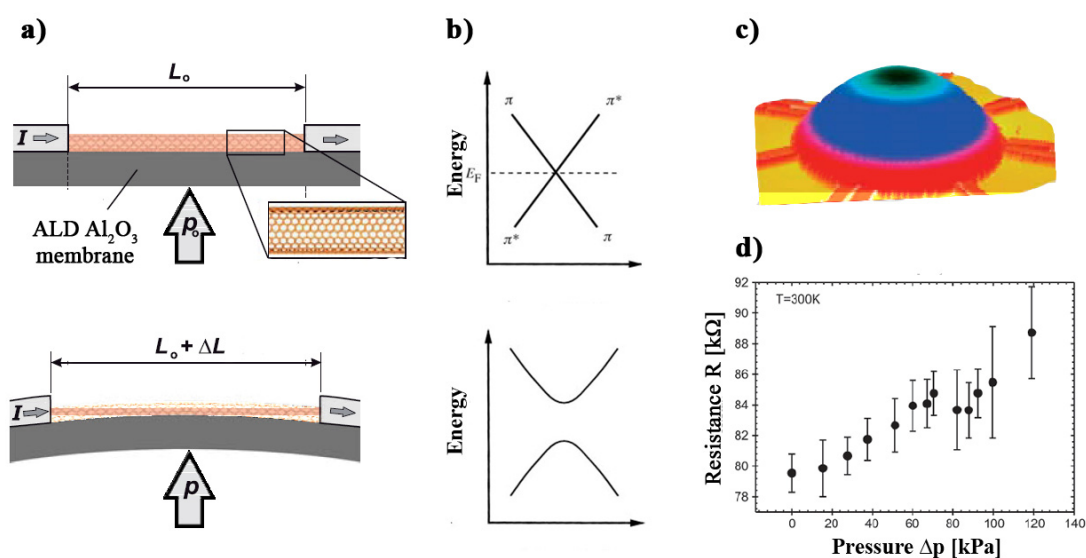


Figure 1.3: a) Schematic setup of a SWNT-based pressure sensor: A contacted m-SWNT lying on an ALD Al_2O_3 membrane is strained due to bulging of the membrane by an applied pressure. b) Straining of the SWNT results in a band gap opening because the symmetry of the m-SWNT structure is broken. c) White-light interferometer image of a bulged membrane with contacted SWNTs on top. d) According to the band gap opening, the resistance of the contacted m-SWNT increases with increasing pressure. Adapted from [35-37].

The first investigations of a pressure sensor on a similar construction were made by Grow et al. [38]. The use of SWNTs as strain gauge transducers were additionally demonstrated in ultra sensitive displacement sensors [7].

1.2.3 Challenge of using SWNTs for sensing applications

In spite of the promising properties of SWNTs and over 10 years of research, there is still a lack of CNT-based devices on the market. There are several reasons for this.

First of all, large scale production processes yielding high numbers of SWNT-based devices do not exist so far because the transition from micro- to nano-scale comprehend many problems to be solved first. Major problems include the proper placement of SWNTs and contacting them by conventional methods. As a practical example, in conventional complementary metal oxide semiconductor (CMOS) processes, O₂ plasma is applied to remove photoresist residuals from the surface after each UV lithography development. However, since nanomaterials are damaged by the highly oxidative O₂ plasma, this method cannot be used. Therefore, the resist residuals remain on the substrate and on the SWNT as shown in Figure 1.1. This can affect the contact between the nanomaterial and the metal electrode and therefore, the electrical transport properties.

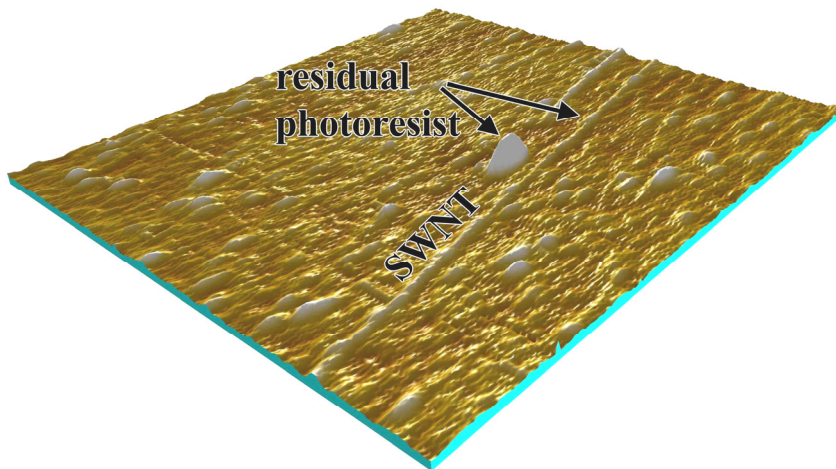


Figure 1.4: 3D AFM image recorded after the development of UV exposed areas showing a substrate with a SWNT and remaining photoresist residuals on the substrate and on the tube, color range: 5nm, image size: 1x1 μm^2 .

Second, reproducibility in SWNT devices has not yet been achieved. One key factor which is still under investigation is the reproducible production of the SWNT material. It is required that all the SWNTs have the same electrical properties. Therefore, they need to be clean, individual, straight, monodispersed in diameter (or even better, of the same chirality), and well-aligned at the desired position.

However, even if SWNT synthesis control is achieved, SWNT-devices still might show different behavior. Defects in the nanomaterial and influences from the direct vicinity are much weightier than it is known from bulk materials. Therefore, these influences can have huge effects on the electrical properties. A practical example which reflects that fact nicely from our lab is shown in Figure 1.5. Depending on the arrangement of the carbon hexagons along the tube axis, SWNTs can have different chiralities defined by the chiral indices (n,m) , and therefore different electrical properties [2]. Calculations of the electronic structure have shown that one third of the SWNTs are metallic and two third are semiconducting. Metallic tubes with diameters below 1.5nm and the chiral indices $(n-m)=3j$, where j is an integer, have a small band gap due to curvature effects [39] and are called quasi-metallic or small-gap-semiconducting SWNTs (SGS-SWNTs). Theoretically, the transconductance of metallic SWNTs is independent of an external electrical field (gate voltage). However, individual SWNTs grown by chemical vapor deposition contacted directly on the substrate measured in our group, show only semiconducting or small band gap semiconducting transport behavior similar to the example shown in Figure 1.5 (including the tubes having mainly diameters around 2nm). Assuming, that not only s-SWNTs and SGS-SWNTs but also m-SWNTs were grown it can be concluded, that the band gap of this m-SWNTs originates from environmental circumstance. It is known that defects in metallic nanotubes change their electrical properties towards semiconducting behavior [15, 40-41]. Another possible explanation of this observation is that small deformations like twists or small kinks on the carbon nanotube caused by a slightly nonplanar substrate changes the orientation of the π -orbital, which results in the formation of a small band gap [42]. This shows that already small influences from the environment can completely change the electrical behavior of SWNTs.

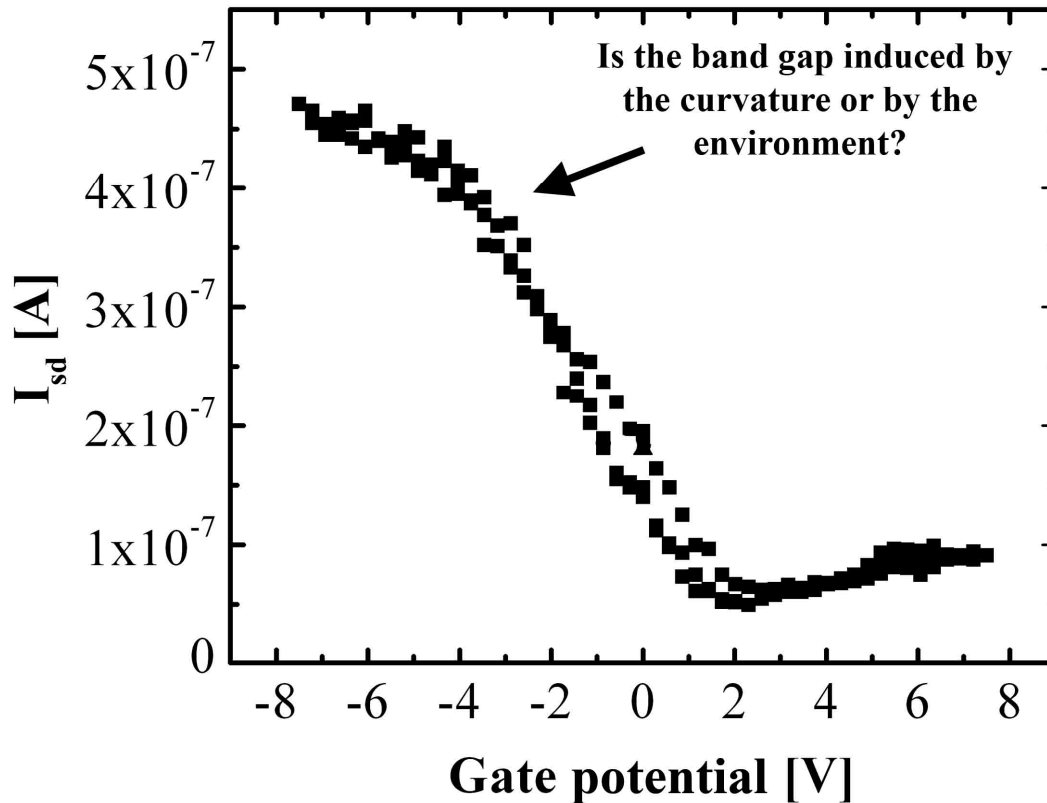


Figure 1.5: Electrical gate sweep measurements of a SWNT with a small band gap. The SWNT could have been metallic for its structure while the band gap was induced by the rough surface, defects or torsion during processing.

Further device parameters, which are not easily controlled but may change the device properties are: channel length, gate oxide thickness, gate-oxide quality, quality of the contacts to the SWNT, and the molecules from the environment [43].

Third, physics and chemistry of CNTs are not yet completely investigated. The theoretical physics of perfect CNTs are studied thoroughly, however, for the calculations approximation models were often applied [2], which do not reflect the conditions in a real system. Further, the influence of defects, grain size of contact metals, molecular adsorption, interaction with chemicals, etc. in real systems are extremely complex and still under investigation.

1.3 Requirements on the SWNT material for the use in SWNT-based sensors

To date, the requirements of SWNTs for device integration, e.g. for the building of SWNT-based sensors, are still not fully known and defined. One of the major problems might be that the properties of SWNTs change with their chirality. Since chirality assignment is not straightforward, and limited to TEM diffraction methods [44] (TEM requires a free pathway for the electron beam), the comparison between device characteristics and the SWNT chirality is often not possible. Therefore, studies are mainly limited to device prototyping. A change in the device properties or functionality from one device to the other is often explained by the lack of chirality control. A second problem, correlated to the first one, is that electrical transistor measurements on single individual SWNTs are only done by a few groups. The main reasons for that are the challenging fabrication of devices consisting of only one SWNT and the difficulty in electrical measurement of such SWNT devices. However, since this is not easy, electrical investigations are mainly focused on the measurements of SWNT devices consisting of multiple individual and bundled SWNTs. Especially groups that are mainly focusing on SWNT growth often perform electrical measurements on multiple SWNTs in addition to spectroscopic and TEM characterization [45-48]. The electrical properties of SWNT are affected by kinks, bends, cross junctions and by the appearance in bundles and by the SWNT environment [15]. These factors can often not be avoided. Therefore, the influence of the SWNT diameter, the channel length, the growth conditions, etc. on the device properties are difficult to determine.

With the increasing interest from the IT industry in CNFETs over the last few years, investigations towards device reproducibility and quality overall, became an important issue. Therefore, the device construction, channel length, gate material and thickness, as well as the diameter and quality of the SWNTs, has turned out to be evenly important as the chirality or type control of the SWNT [49-53].

This thesis was carried out in strong collaboration with Thomas Helbling, Moritz Mattmann and Cosmin Roman who were using the grown SWNTs for, device and sensor studies [6, 28, 30-31]. Therefore, the capability of the grown SWNTs for the use in SWNT-based devices has been verified from time to time electrically, and the requirements on the SWNTs have been discussed thoroughly and further develop all the time.

These requirements were determined with regard to large scale wafer-based device production implemented in standard silicon on insulator (SOI) wafer-based micro electromechanical systems (MEMS) processing. Today's SWNT integration is mainly based on electron beam (e-beam) lithography. In this process, SWNTs with the desired diameters, lengths and shapes were selected for contacting. Contacts were formed by e-beam lithography, metal evaporation and lift-off [30]. This serial process is well suited for

prototyping purposes. In a large scale integration process, selection of SWNTs will no longer be possible. In order to maintain the quality of the serial integration process in a batch integration process, the SWNTs need to fulfill some additional requirements. The overall goals in batch SWNT-based sensor production are reproducibility and reliability. Reproducibility means that each produced device has similar device characteristics with regards to the threshold shift¹ and the ratio between the on and the off current $I_{\text{on}}/I_{\text{off}}$.

For the production of reproducible SWNT-based sensors consisting of only one SWNT as a transducer element, the following points are important:

- Synthesis of SWNTs that are free of contaminations
- Control of the SWNT type
- Synthesis of straight SWNTs
- Synthesis of individual SWNTs
- Synthesis of SWNTs with controlled average diameters and narrow diameter distribution
- Control of the SWNT density
- Control of the SWNT position and alignment

In the following sections, these requirements are discussed in detail.

1.3.1 Synthesis of SWNTs that are free of contaminations

For many applications, SWNTs have superior properties compared to double- or multi-walled CNTs, as already discussed in chapter 1.1.3. In particular, only SWNTs show semiconducting behavior (CNFET-based sensors), and only SWNTs have high gauge factors (piezoresistive sensors). Therefore, a process in which only SWNTs are synthesized is crucial. The cleanliness of a SWNT is very important. Amorphous carbon contamination from pyrolysis of the carbon feed stock gas can contaminate the SWNT and the surrounding surface, which could reduce the quality of the contacts and change the electrical behavior of a CNFET. Strong amorphous carbon contamination can even disable NEMS processing steps, like HF release for suspending structures [54]. Another contamination source is the catalyst. Catalysts covering the surface by a whole layer contaminate the grown SWNTs during and after growth.

¹ As explained in the previous section, also metallic SWNTs show quasi-metallic behavior in transistor measurements (Figure 1.5). Therefore, a threshold-like value can be determined by taking the voltage where the minimum current occurs as “off-state potential”.

State-of-the-art

The growth of primarily SWNTs has been reported in the early stage of CNT research. Co-evaporation of catalytic metals e.g. Ni, Cu, Fe, Co, enabled the growth of SWNTs by arc-discharge and laser ablation [4-5, 55]. CVD grown SWNTs were first presented by Dai et al. [56]. The production of high quality SWNTs with low amorphous carbon contamination in CVD SWNT growth is mainly related to the use of an appropriate surface and the use of gases or vapors (e.g. H₂, H₂O, CO₂, H₃C₂OH) for cleaning the catalyst and avoiding amorphous carbon formation [54, 57-61]. In laser ablation and arc-discharge growth, post purification processes are required to obtain clean SWNT structures [62-63]. The formation of catalysts which form individual catalysts on the surface resulting in a reduced contamination of the SWNTs is often related to catalyst diameter and density control (see therefore section 1.3.5 and 1.3.6).

1.3.2 Control of the SWNT type

As already mentioned, SWNTs can either be metallic, small band gap semiconducting or semiconducting. For many applications, only one type is required. For example, in CNFET based sensing, the use of s-SWNT is favorable [30], while best gauge factors were achieved with SGS-SWNTs [38]. Therefore, controlling the SWNT type is important.

State-of-the-art

So far, there exist five methods resulting in either only metallic or only semiconducting SWNTs.

- By alternating current (AC) dielectrophoresis, where an alternating current is applied between two electrodes, SWNTs can be selectively deposited by their differences in polarity. Hence, metallic SWNTs are preferentially deposited on the electrodes [64].
- There exist several post processing steps for sorting metallic from semiconducting SWNTs [65]. For example, it is possible to separate them by density gradient centrifugation [66] or, even more easily, metallic SWNTs can be destroyed by an electrical breakdown [67].
- The growth of only semiconducting SWNTs was achieved by plasma enhanced CVD growth [40]. The drawback of growing semiconducting tubes by this method tends to be due to defects induced by the plasma [68]. Such defects are not controllable and therefore unwanted.
- Within the last year, several groups have shown that it is possible to grow mainly s-SWNTs with a CVD growth process resulting in narrow diameter distributions [45, 69-70].

1.3.3 Synthesis of straight SWNTs

The SWNTs must be straight, especially if the tubes will be suspended or used for NEMS sensing applications. For example, in SWNTs based resonators, slack reduces the device performance and reproducibility. Additionally, strong bends or kinks can change the electrical properties of the SWNT [42].

State-of-the-art

So far, few investigations have been reported on the synthesis of straight SWNT. Since they are rather stiff, most SWNTs grow straight anyway. There might be a difference in base-grown and tip-grown SWNTs. Since in base-growth the catalyst particle is fixed to the growth surface, the SWNTs growth is straight away from the surface as shown in Figure 1.6 a) [71]. SWNTs which are growing along the substrate by tip-growth might adapt the shapes of the steps on the monocrystalline surface as shown in Figure 1.6 b) [72-73].

SWNTs deposited on the substrate from a solution or a suspension (HiPCO, laser ablation, and arc-discharge SWNTs) are more often bent due to non-proper alignment.

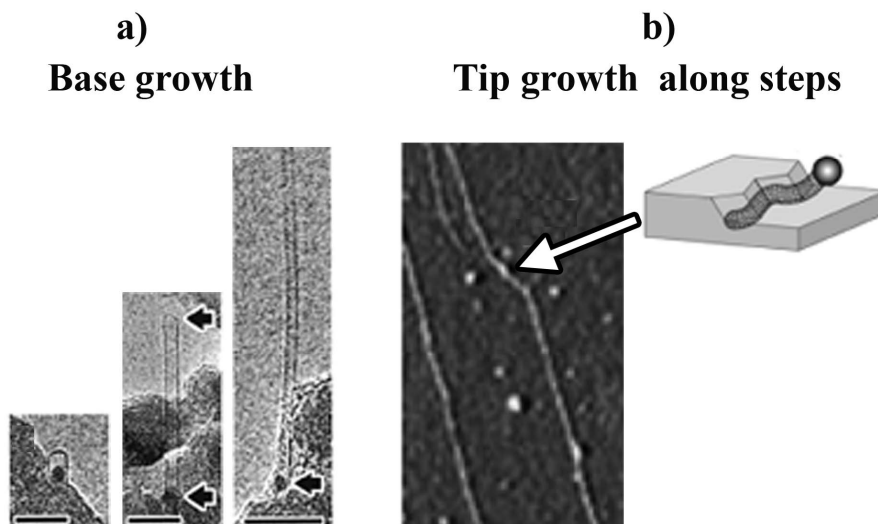


Figure 1.6: a) Tip- and b) base-growth of SWNTs. SWNTs grown by base-growth are mainly straight, while the straightness of tip-grown SWNTs can depend on the substrate, adapted from [71-73]. a) Scale bars: 10nm b) Image size: ca. 1 μ m x 2 μ m.

1.3.4 Synthesis of individual SWNTs

It is necessary to produce individual SWNTs. If two or more SWNTs stick together one speaks of a bundle of SWNTs (see Figure 1.7 a). Since the type and the amount of the SWNTs in the bundle can not be controlled, the electrical behavior of the bundle will change from bundle to bundle. Not only the overall electrical behavior, but also the

behavior of one tube in the bundle, is changed by neighboring tubes due to the breaking of symmetry, which results in a band gap opening [37]. Therefore, it is important to produce individual SWNTs as shown in Figure 1.7 b).

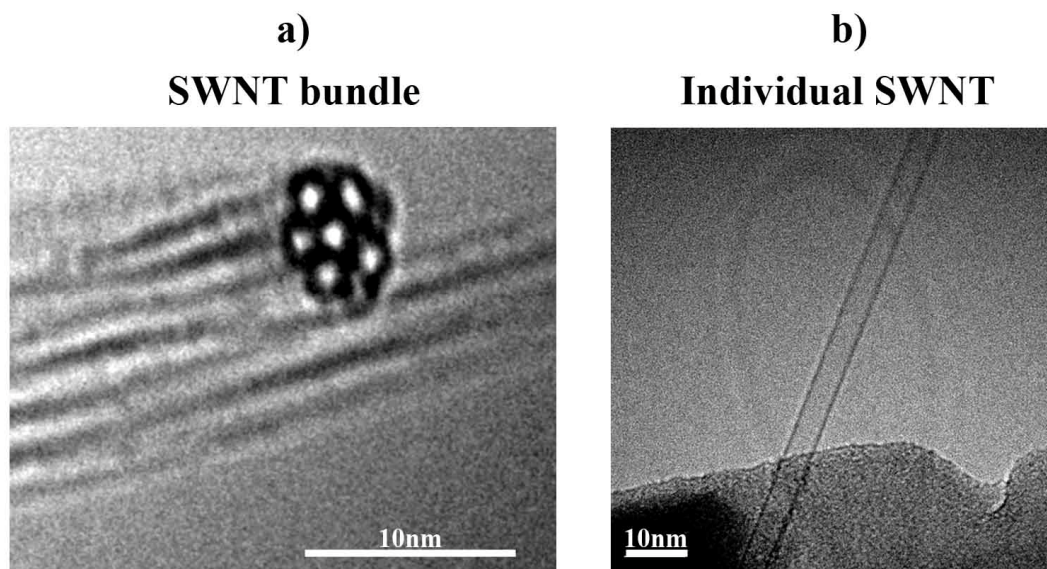


Figure 1.7: TEM image of a SWNT a) bundle and b) an individual SWNT

State-of-the-art

So far, it is not yet thoroughly investigated how SWNTs form bundles. Most of the SWNT growth processes yield only, or mainly, bundled SWNTs. Iijima explained the growth of only bundles in the laser evaporation and arc-discharge techniques by a correlated growth, resulting from the connection of the SWNTs on open ends by metal atoms [15]. Kong et al. [74] recognized that SWNTs grown by CVD on Al_2O_3 supported catalysts tend to form less bundles than SWNTs grown from SiO_2 supported catalysts. This observation is explained with the size and distribution of the catalysts. While the SiO_2 supported catalysts are uniformly distributed and of similar size, the Al_2O_3 supported catalysts are not. Therefore, the bundle formation process on SiO_2 supported catalysts can be explained by Van-der-Waals interactions, which cause SWNTs grown from neighboring catalysts to stick together. On the other hand, the use of well separated Al_2O_3 supported catalysts in patterned electrode structures resulted in the growth of mainly individual SWNTs [75]. Presently, this sticking model appears to be correct. With the progress in aligned growth in combination with a low SWNT density, bundle formation seems to no longer be an issue [47, 70]. So far, there is no way to avoid bundle formation by laser ablation and arc-discharge. Therefore, post treatments like ultra-sonification in the presence of surfactants [76] and subsequent centrifugations [66] are required.

1.3.5 Control of the SWNT density

The control of the SWNT density on the surface is very important for the production of devices consisting of only one SWNT. A high SWNT surface density results in unwanted device shorting by other tubes. The crossing of SWNTs can change their electrical properties [15]. Additionally, as discussed in the previous section, CVD growth of reduced SWNT densities can further prevent bundle formation.

State-of-the-art

Here, recent approaches for CNT density control of CVD grown CNTs directly on the surface is discussed.

The CNT density on a surface can be varied in two ways: first by the amount of catalysts, as initially shown by Tu et al. [77], who were able to control the MWNT density by the electrochemical deposition pulse time for catalyst formation, and second by the parameters in the CVD growth process. Table 1.3 shows parameters, which tend to influence the CNT density on the surface. It has been shown that increasing the growth time and temperature can lead to higher CNT densities on the surface [78-79]. More common for density control, are variations in catalyst preparation. Fu et al. [80] have shown that the density can be changed by a special catalyst preparation procedure, where Fe is encapsulated by micelles. The catalyst density is changed by the ratio of Fe/PVP² initially put into the solution for catalyst formation. Unfortunately, the diameter of the catalysts increases also with increasing Fe/PVP ratio; hence the SWNT density is not independent on the SWNT diameter. Jeong et al. [81] showed that the SWNT density depends on the dilution of the Ferritin solution, which is spin coated on the surface. But also in this process, dependence between SWNT diameter and density has been observed.

All these investigations only show trends. A method, resulting in real SWNT density control has not been shown so far. Therefore, the SWNT density is mainly controlled by patterning the catalyst on the surface [21, 75, 82-83], i.e. the SWNT density can be controlled by the catalyst pattern size and the pattern density on the surface. However, without catalyst density control, the pattern size has to be extremely small providing the formation of only one catalyst per growth spot and this requires e-beam processing which is not compatible with batch processing [84].

² PVP means polyvinylpyrrolidone and is a block polymer.

Table 1.3: State-of-the-art SWNT surface density control

Catalyst	Observed density change	Density control ³	Diameter control	Reference
Dependence on the growth parameters				
Fe sputtering	Increase of the growth Temp. leads to an increase of the MWNT Density	No investigations	No investigations	O.A.Nerushev (2002) [79]
Floating catalyst Fe(CO) ₅	Increase in the growth time leads to an increase in the SWNT density	No investigations	No investigations	S. Huang (2003) [78]
Dependence on the SWNT catalyst density				
Fe from micelles	Fe/PVP ratio: decreasing PVP content decreases the catalyst density on the surface.	No investigations	by the Fe:PVE ratio	Q.Fu. (2004) [80]
Fe from Ferritin (spin coated)	Increasing ferritin conc. increases the SWNT density	No investigations	by the amount of loaded iron.	G. Jeong (2005) [81]
Co evaporation	Increasing catalyst layer thickness increases the SWNT density	No investigations	No investigations	A. Iai (2006) [83]
Fe sputtering on Ir or Al	Increasing the catalyst support thickness increases the SWNT density. Adding Mo to the Fe catalysts increases the SWNT density.	No investigations	No investigations	L. Delzeit (2001) [82]

1.3.6 Synthesis of SWNTs with controlled average diameter and narrow diameter distribution

Controlling the SWNT diameter and producing SWNTs with narrow diameter distributions is one of the key factors for the production of reproducible SWNT-based devices. The diameter of the tube determines whether the metal-SWNT contact is a Schottky contact or a ohmic contact, and it also defines the size of the band gap. Therefore, the diameter determines the I_{on}/I_{off} ratio of a CNFET, while the I_{on} is defined by the contact resistance to the contact metal and the I_{off} by the width of the band gap. The diameter distribution on the other hand defines the distribution of the band gaps. Their influence on the threshold potential of a CNFET has not been investigated yet.

Ohmic contact resistance to SWNTs

Two studies reported the influence of the SWNT diameter on the on-state current of s-SWNTs, as shown in Figure 1.8.

³ No investigations means, that it has been shown, that the described procedure influences the SWNT density but it has not been investigated in which range the density can be controlled, how strong is the influence of the used parameters and can the density be reproduced.

Chen et al. made measurements with s-SWNTs grown by laser ablation [49], while Kim et al. used individual CVD grown SWNTs for the investigations [52]. The study of Chen et al. showed that the maximum CNFET on-state current depends on the interface barriers (Schottky barriers (SB)) between the SWNT and the metal. Pd, Ti and Al were tested for contact metals, where Pd showed the smallest contact barrier heights. The diameter dependence measurements (see Figure 1.8 square dots) show that the on-state current in CNFETs is monotonically increasing with increasing SWNT diameter. The authors fitted an extended SB model, which considers gating of the contacts. With this model, no SB occur for SWNT diameters $>1.5\text{nm}$. Therefore it is concluded that all SWNTs with larger than 1.5nm make ohmic contacts to Pd. Unfortunately, this study only shows investigations on SWNTs up to 1.5nm , probably limited by SWNTs grown by the laser ablation technique.

Kim et al verified the trend for better contacts in large diameter semiconducting and metallic SWNTs [52]. Regarding s-SWNTs, they observed a drastic increase in the on-state current with an increase in the tube diameter for diameters below 1.6nm (see Figure 1.8 round dots). For diameters between 1.6nm and 2nm , the current increase is more gradually with increasing diameter, while for diameters above 2nm , the current-diameter curve saturates. In the case of m-SWNTs (see Figure 1.8 triangles), where no SBs are formed at the interface, a diameter dependent contact resistance similar to the s-SWNTs was obtained. Pure tunneling barriers in m-SWNTs with diameters $<1.7\text{nm}$ are the reason for this observation.

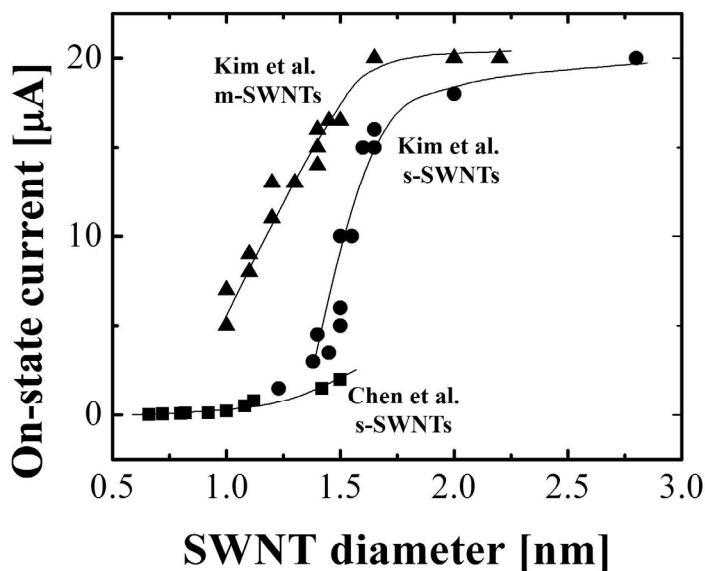


Figure 1.8: Dependence of the on-state current on the m-SWNT and the s-SWNT diameters. Measurements from individual CVD grown SWNTs (Kim et al. [52]) are compared with measurements from SWNTs produced by laser ablation (Chen et al. [49]). Channel length: 200nm - 300nm , gate thickness (SiO_2): 10nm , source-drain voltage: 1V (Kim et al.), 0.5V (Chen et al.).

Kim et al. applied a different model for the SB height calculation than the one used Chen et al. did. According to that model, a diameter of 1.6nm is still at the lower limit for the production of devices with low contact resistances. SWNTs with diameters around 1.6nm still yield a barrier height of $\sim 70\text{meV}$ for their contact to Pd, while the barrier height for s-SWNTs with diameters $>2\text{nm}$ was estimated to be 0meV .

Band gap in CNFET sensors

For SWNT-based chemical and biochemical sensors in FET-based architecture, the use of SWNTs resulting in a sufficient I_{on}/I_{off} ratio is crucial for the sensitivity of a sensor based on current readout. As discussed above, the on-state current mainly depends on the tube diameter and on the type of contact metal. The off-state current is determined by the thermal activation and therefore by the size of the band gap, E_g , of the s-SWNT as shown in the thermally activated transport model [85].

$$I_{ds} = \frac{2e^2}{h} |t|^2 \left(\frac{2}{1 + \exp(E_g / k_B T)} \right) V_b \quad (1.1)$$

I_{ds} is the source-drain current, e is the elementary charge, h and k_B are the Planck and the Boltzmann constants, respectively, V_b is the bias voltage and t is the average transmission amplitude for electrons through the SWNT channel. From this formula it can be obtained that with decreasing band gap the off-current increases.

The band gap itself is determined by the SWNT diameter, d , by the following relation, which is plotted in Figure 1.9:

$$E_g = \frac{0.9eV}{d} \quad (1.2)$$

This results in band gaps of 0.9eV , 0.45eV and 0.3eV for s-SWNTs with diameters of 1nm , 2nm and 3nm respectively. Javey et al. showed in first CNFET measurements for a SWNT with a diameter of 3.5nm , an off-state current below 10^{-12}A and an on-state current of 10^{-6}A . This I_{on}/I_{off} ratio of 10^6 should be acceptable for CNFET sensors. Therefore, for CNFET sensing application and with regards to the I_{on}/I_{off} ratio, a SWNT band gap of 0.3eV has still enough resolving power for good sensor performances.

Whether the band gap on the other hand has an influence on the off-state or threshold potential of a CNFET is not known yet. Nevertheless it might be important to have SWNTs with narrow band gap distributions. Since the band gap decreases with the relationship $1/d$, the band gap deviation decreases with increasing SWNT diameter. Therefore, SWNTs with small mean diameters have much larger band gap deviations than SWNTs with larger mean diameters but the same diameter distributions. For example, a diameter of 1.5nm and a diameter distribution of 0.3nm results in a band gap of 0.6eV $\sigma^+ = 0.15\text{eV}$ and $\sigma^- = 0.1\text{eV}$,

while the same deviation for a diameter of 2nm results in a band gap of 0.45eV $\sigma^+=0.08\text{eV}$ $\sigma^-=0.06\text{eV}$.

Figure 1.9 displays the desired SWNT diameter and diameter distribution for CNFET based sensors. The black curve shows the decrease in band gap with increasing SWNT diameter. As discussed earlier, the minimum SWNT diameter for adequate contact resistance is 1.5nm (solid line across the graph), while the maximal diameter cannot be defined exactly. However, the device performance is slightly decreasing with increasing diameter due to the effects of the thermal activation model (indicated by the color gradient). Most synthesis methods yield SWNTs whose diameter distributions are Gaussian in nature. Assuming an optimal average diameter of 2nm (not investigated yet) and a deviation of $\sigma=0.3\text{nm}$, only 5% of all SWNTs would have diameters below 1.5nm. With a deviation of $\sigma=0.2\text{nm}$, the amount of SWNTs with diameter below the lower limit decreases to 1.5%. Considering these distributions in large scale SWNT integration process only 5% or 1.5% of all contacted SWNTs would not make ohmic contacts to Pd.

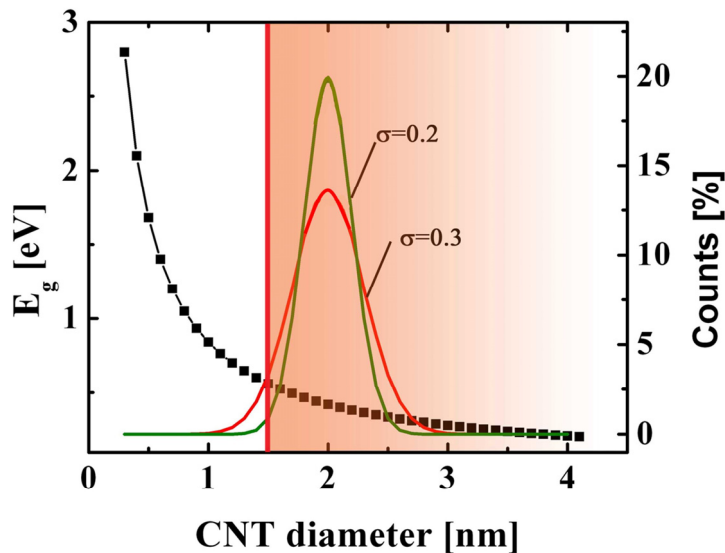


Figure 1.9: Required SWNT diameter and diameter distribution for CNFET based sensors: The diagram shows the dependence of the band gap on the CNT diameter (dotted curve). The lower diameter limit for SWNTs in CNFETs determined by the contact resistance is indicated by the solid line at 1.5nm. The CNFET quality decrease due to increasing thermal activation is indicated by the color gradient. Considering the production of devices having ohmic contacts in combination with the thermal activation and small band gap distributions, an optimal mean SWNT diameter is assumed to be around 2nm, while the distribution should be $<0.3\text{nm}$ as indicated by the two Gaussian distributions.

State-of-the-art

In Figure 1.10, the state-of-the-art SWNT diameters and diameter distributions are compared. The mean SWNT diameters are plotted vs. the SWNT diameter distributions. To highlight the usability of the SWNTs for high quality device production in large scale integration processes, the region of SWNTs making Schottky contacts and the region of SWNTs making ohmic contacts to Pd are colored white and grey, respectively. The transition region, with up to 10% of the SWNTs making Schottky contacts or 90% making ohmic contacts, is highlighted by the color gradient. Once again it has to be mentioned that these boundary conditions were defined according to Chen et al. [49]. With regards to the work of Kim et al. [52], the border between Schottky and ohmic contacts has to be shifted by 0.5nm towards larger SWNT diameters.

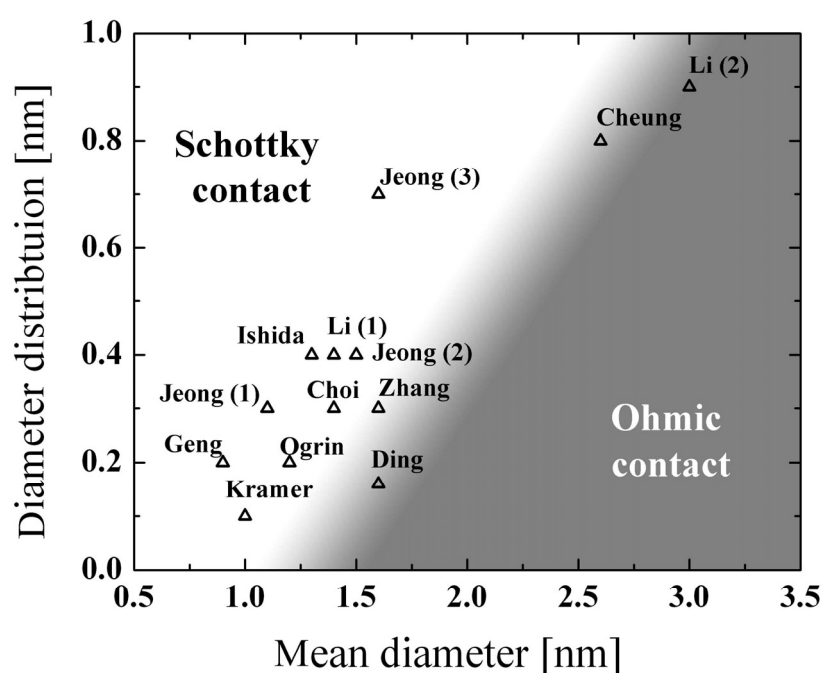


Figure 1.10: State-of-the-art SWNT synthesis with regards to the SWNT diameter and diameter distribution. SWNTs situated in the white area would make Schottky contacts to Pd, while the SWNTs situated in the grey area would result in ohmic contacts to Pd according to the studies of Chen et al [49]. References: Li [71], Cheung [86], Jeong [81, 87], Ishida [88], Choi [89], Zhang [90], Geng[91], Ogrin [92], Ding [45] and Kramer [93].

SWNTs formed by laser ablation [55] or arc-discharge [5] can have a narrow diameter distribution, but mean diameters are typically between 1nm and 1.4nm. Zhang *et al.* [90] were able to increase the mean diameter of SWNTs formed by laser ablation to 1.6nm \pm 0.3nm by adding Fe to a NiCo catalyst. The HiPCO SWNT synthesis process is not mentioned in the figure, because it results in only procedures SWNTs with diameters below 1nm [94].

In CVD growth of SWNTs, the diameter depends strongly on the catalyst size [86, 95]. Using catalyst particles of the appropriate size, it is possible to grow SWNTs with larger diameters. However, due to the difficulties in controlling the size distribution of the catalyst, the resulting SWNT diameter distribution increases with increasing mean diameter, as shown in Figure 1.10. Therefore, in most investigations that claim the growth of SWNTs having narrow diameter distributions ($\sigma < 0.5\text{nm}$), the mean SWNT diameter is below 1.5nm [87-89, 91-93]. The growth of SWNTs with larger diameters mainly results in drastically increased diameter distributions ($\sigma > 0.5\text{nm}$) [71, 81, 86, 96]. The growth of SWNTs from catalysts formed by a cavity, like dendrimers [89, 91, 97], proteins [71, 93] or particles protected by ligands [86] is promising. Differing from vapour or liquid phase deposition, the catalyst is already formed prior of the deposition, which results in more defined and well separated catalysts. Therefore, the size of the catalyst and hence the diameter of the SWNT can be controlled. However, real catalyst size control has only been shown by the use of Ferritin proteins [71, 81, 87] and the use of iron pentacarbonyl with different sorts of Fe ligands. In the first case, the size is adjusted by the amount of loaded Fe in the protein core, and in the second case, the type of ligand defines the size of the particle.

It is known that the type or composition of the catalyst and the CVD growth condition can have an impact on the SWNT diameter and diameter distribution as well. Such studies were mainly made with sputtering or liquid phase deposition techniques, where the analysis of the catalyst size due to their high density on the surface is not possible. Therefore, a correlation between SWNT diameter and catalyst size has only been made by Lu et al. [98]. Since the SWNT density and SWNT diameter are both dependent on the SWNT growth conditions, changing the SWNT diameter will also change the SWNT density. Additionally, in these techniques, the diameter control is limited to a certain range.

Recently, Ding et al. [45] have grown SWNTs with a mean diameter of approximately 1.6nm and a remarkably narrow diameter distribution of $\pm 0.16\text{nm}$ using Cu catalysts and a mixture of methanol and ethanol as carbon source. This investigation was performed on a crystalline quartz substrate. However, considering the requirements determined above, a diameter of 1.6nm is still at the lower limit for the production of devices with low contact resistances.

A process yielding SWNTs around 2nm with diameter distributions $< 0.5\text{nm}$ has not been shown so far.

As already discussed, the SWNT diameter is not the only important issue for the production of CNFETs with contacts of high quality. Providing a direct (clean) metal-SWNT contact is evenly important. Table 1.4 shows the on-state resistances of different CNFET production processes from different groups. The data were taken from gate sweep characteristics shown in the publications or if mentioned, directly from the author's text. Processes, which are based on CVD grown SWNT directly on the surface show on-state resistances below 100k Ω , while integration processes based on SWNT deposition from solution (colored in

grey) result in resistances $>100\text{k}\Omega$ and SDS or SDBS coated SWNTs often in resistances $>1000\text{k}\Omega$ (see Vijayaraghavan [99]).

Table 1.4: On stat resistances of CNFETs from different integration processes and different groups

V_{sd} (V)	On-state current (A)	On-state resistance (k Ω)	SWNT Material	SWNT diameter (nm)	Ref.
-	-	>100 (min. 17)	CVD	1	Yao [12]
0.03	0.65×10^{-6}	46	CVD	~ 2	Helbling [29]
1	20×10^{-6}	50	CVD	~ 2.7	Kim [52]
0.5	2.5×10^{-6}	200	Laser ablation	~ 1.5	Chen [49]
-	-	260 (mean)	CVD from solution	~ 1.8	Burg [100]
-	-	300	HiPCO	-	Stampfer [7]
0.4	0.65×10^{-6}	400	CVD	~ 1.5	Schwalke [101]
0.1	8×10^{-7}	1000	Laser ablation	-	Vijayaraghavan [99]

1.3.7 Control of the SWNT position and alignment for large scale SWNT integration

For statistical analysis and industrial production of SWNT-based sensor devices, a large scale integration process is required. Therefore, the growth position and direction has to be defined. For batch fabrication, the integration process is preferably based on standard UV lithography. To have a high yield of high quality devices with only single-bridging individual SWNTs, all the discussed requirements in SWNT synthesis control are crucial.

State-of-the-art SWNT integration

SWNT devices were first produced by spin coating of dispersed SWNTs on a surface decorated with electrodes [102]. This method was improved by writing the electrode structures on top of the spin coated SWNTs by e-beam lithography [103], metal evaporation and lift-off. This method allows the fabrication of suspended NEMS structures [104]. For the production of devices showing ohmic contacts, SWNTs grown on the substrate can be used instead of SWNTs from solutions which are often encapsulated by strong binding sodium dodecyl sulphate (SDS) or sodium dodecylbenzene sulphonate (SDBS) surfactants [30]). ALD Al_2O_3 encapsulation results in SWNT devices with long-term stability [29]. However, these methods are time consuming and therefore no suitable for statistical investigations on CNFET or large scale CNFET sensors production.

The fabrication of a large number of devices on one wafer was demonstrated by the use of dielectroforetic [64] or self assembled [105-106] SWNT deposition from solution. However, as already discussed, due to the use of surfactants in the solutions, the contact resistances are at least a factor 10 higher [99-100] compared to devices consisting SWNTs directly grown on the surface.

Most promising methods for large scale SWNT device fabrication are achieved using CVD for SWNT synthesis. With this growth method, SWNTs can be grown, well aligned, directly on the substrate at defined positions.

Figure 1.11 summarizes the state-of-the-art of in large scale integration techniques. In the upper part, state-of-the-art growth alignment and position control are described, which are requirements for large scale device production. The device fabrication processes are described in the lower part of the figure.

Control of the growth position can be achieved by the structuring of catalyst islands. The SWNTs then grow from these defined areas. This has been shown first by Soh et al. [107], who was using e-beam lithography for catalyst patterning and electrode structuring on top of these growth islands after the SWNTs were grown. Disadvantage of this method is that e-beam lithography is not suitable for large scale processing. Therefore, Marty et al. [108-111] introduced a one-step deep DUV technique for electrode and catalyst structuring. In this process, electrodes were structured by deep UV lithography and metal evaporation. A thin layer of Co catalysts was evaporated on the contact metal prior to the lift-off. SWNTs then bridge, by chance, from one electrode to the other. Since the SWNT grow from a metallic substrate, density and diameter control might be limited. Most convenient for large scale SWNT device production is the use of standard DUV lithography for both catalyst and electrode structuring. SWNT integration with this technique has already been proven by several groups [33, 112-113]. However, statistics on the integration yield is often missing. Rispal and Schwalke [101, 114] presented a simple one step integration method by just structuring electrode pads on a surface on which SWNT were growth globally. Their CNFET device yield is around 70% resulting in approximately 1000 devices per 4" wafer. All state-of-the-art processes might yield individual SWNTs, bundled SWNTs, single as well as multiple bridging SWNTs. Therefore the yield of devices consisting of only individual single-bridging SWNTs might be low. Also diameter-controlled integration has not been considered so far. Rispal and Schwalke [101, 114] claimed in their papers to produce only single-bridging SWNT devices. However, they mentioned also, that this has not been proven by SEM or AFM.

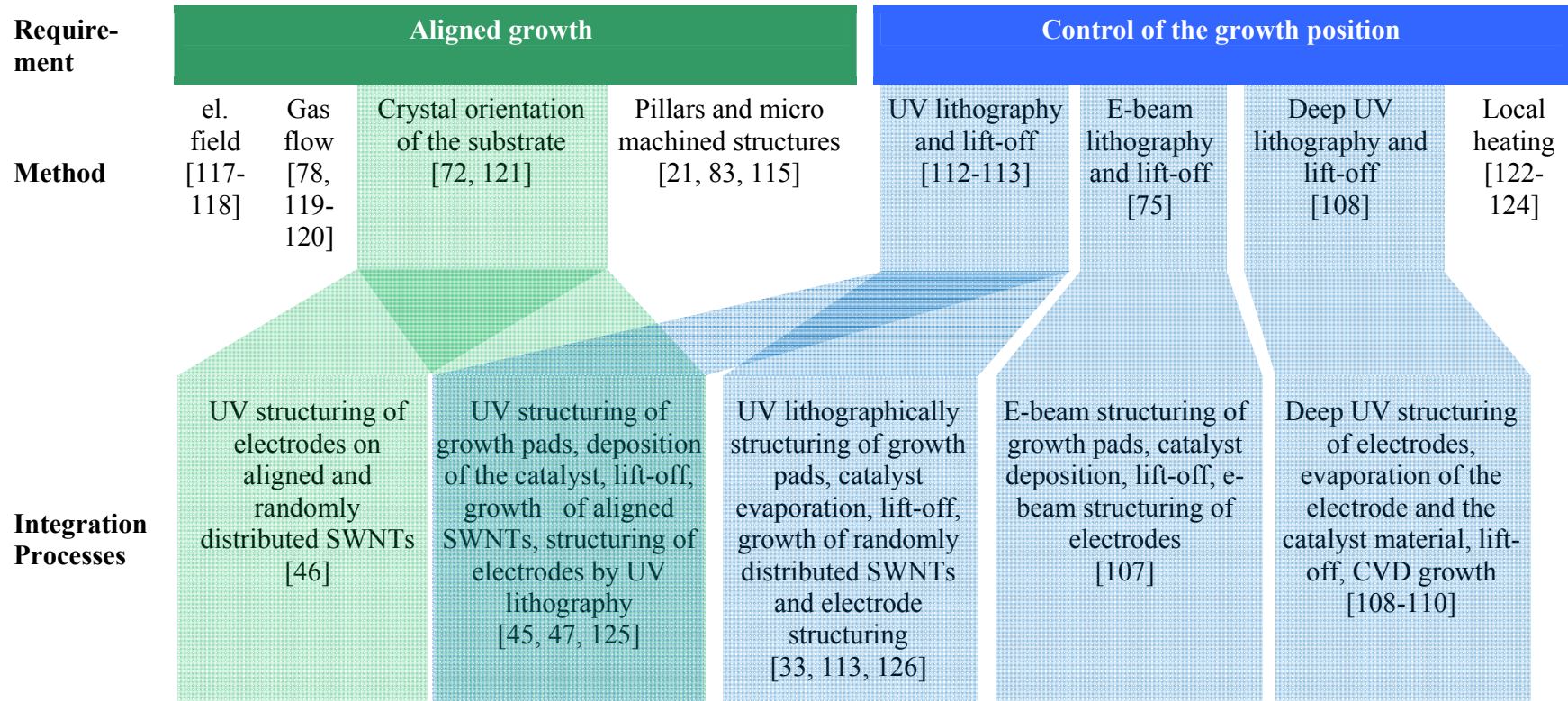


Figure 1.11: State-of-the art SWNT large scale integration using CVD for SWNT synthesis.

For an increased integration probability of individual SWNTs, control of the growth direction is required. This has been achieved by different growth techniques. In electrical field assisted growth, an alternating electrical field is applied during the growth to guide the growing SWNTs. Using a laminar gas flow during SWNT growth also results in well aligned SWNTs. Investigations have shown that SWNTs growing from a free standing structure or pillar will attach most likely to the next neighboring pillar [21]. This effect has been used to integrate SWNTs into MEMS structures [115-116].

A simple but powerful approach for aligned SWNT growth is to use monocrystalline substrates. Guided by the crystal orientation, SWNTs all grow in the same direction. Therefore, this method has been used for large scale device fabrication with and without catalyst structuring previous to growth [46-47, 125]. However, only devices with multi arrays of SWNTs were produced so far. The fabrication of devices consisting of only one individual SWNT has not yet been shown.

1.4 Objectives

The general objective of this project is to advance SWNT growth to a level where functional CNFETs for sensing applications can be produced while contributing to the basic understanding of controlled SWNT growth. To reach these goals, investigations into the growth of SWNTs in a controlled manner need to be done.

Therefore the following will be investigated:

- Basic understanding of the SWNT growth process by CVD on SiO₂ surfaces
- Synthesis of SWNTs that are free of contaminations
- Synthesis of straight SWNTs
- Synthesis of individual SWNTs
- Synthesis of SWNTs with controlled average diameters and narrow diameter distribution
- Control of the SWNT density
- Investigation of a large scale integration process

Basic understanding of SWNT growth by CVD on SiO₂ surfaces

A model will be determined that explains the effect of CVD parameters such as temperature, carbon source gas partial pressure, H₂ pressure, and catalyst size on the SWNT nucleation yield and amorphous carbon formation. Furthermore the growth and termination of SWNTs on SiO₂ substrates will be investigated.

Controlled SWNT growth by CVD

A SWNT synthesis process will be investigated (catalyst preparation process and CVD growth parameter determination) that yields **clean individual straight SWNTs**. Such a process will require independent control of **SWNT density** and **SWNT diameter**. In addition, it will be critical to be able to grow SWNTs with **mean diameters around 2nm** and **diameter distributions below 0.5nm** in order to provide high quality CNFETs with **system resistances below 100kΩ** (for channel lengths of around 1 μm).

Investigation of a large scale integration process

State-of-the-art catalyst position control is mainly based on E-beam lithography. A goal of this thesis is to establish a method based on a high-throughput compatible photolithography process, which is compatible with all of the objectives in SWNT growth control described above. Furthermore, this new process should have a high yield of single-bridging individual SWNTs so that statistical investigations on the integration process and on the SWNT synthesis are possible.

2 Theory

In this chapter, the SWNT structure is defined first, followed by a description of its electrical transport properties. In a second part, the SWNT synthesis is discussed in detail. Besides the most important synthesis methods and the basic model for SWNT growth, a new model is determined. The influence of growth parameters on the SWNT nucleation and growth by chemical vapour deposition is described. Furthermore, a short summary about the mechanism of iron loading and storage of this protein is provided at the end of this chapter.

2.1 Structural parameters of SWNTs

This chapter is mainly based on the basic background part of a book written by Dresselhaus et al. [15]. The structure of a SWNT is defined by the chiral indices (n,m) , which determine the chiral vector \mathbf{C}_h and the transition vector (\mathbf{T}) orthogonal to \mathbf{C}_h . The chiral vector itself is defined by the relation $\mathbf{C}_h = n\mathbf{a}_1 + m\mathbf{a}_2$, which connects to the crystallographic equivalent sites on a 2D graphene sheet shown in Figure 2.1. \mathbf{a}_1 and \mathbf{a}_2 are unit vectors of the hexagonal honeycomb lattice of the graphene sheet. The chiral angle θ is the angle between \mathbf{C}_h and the “zigzag” direction ($\theta = 0$) shown in Figure 2.1 a) and b). Warping a graphene sheet defined by the chiral vector \mathbf{C}_h to a cylinder, results in the SWNT with the chiral indices (n,m) . Therefore, three types of SWNTs can be distinguished as shown in Figure 2.1 c): Armchair SWNTs have chiral indices (n,n) , zigzag SWNTs have chiral indices $(n,0)$ and chiral SWNTs have chiral indices (n,m) with $m \neq 0$ and $n \neq m$.

SWNTs can either be metallic, small-gap semiconducting or semiconducting. All armchair SWNTs are metallic. Small-gap semiconducting SWNTs are defined over the relation $n - m = 3j$, where j is an integer. At room temperature, these SWNTs behave like metallic SWNT. In Figure 2.1 all the metallic and small-gap SWNTs are colored green Semiconducting SWNTs with $n - m = 3j + 1$ are colored pink and the $n - m = 3j + 2$ are colored purple.

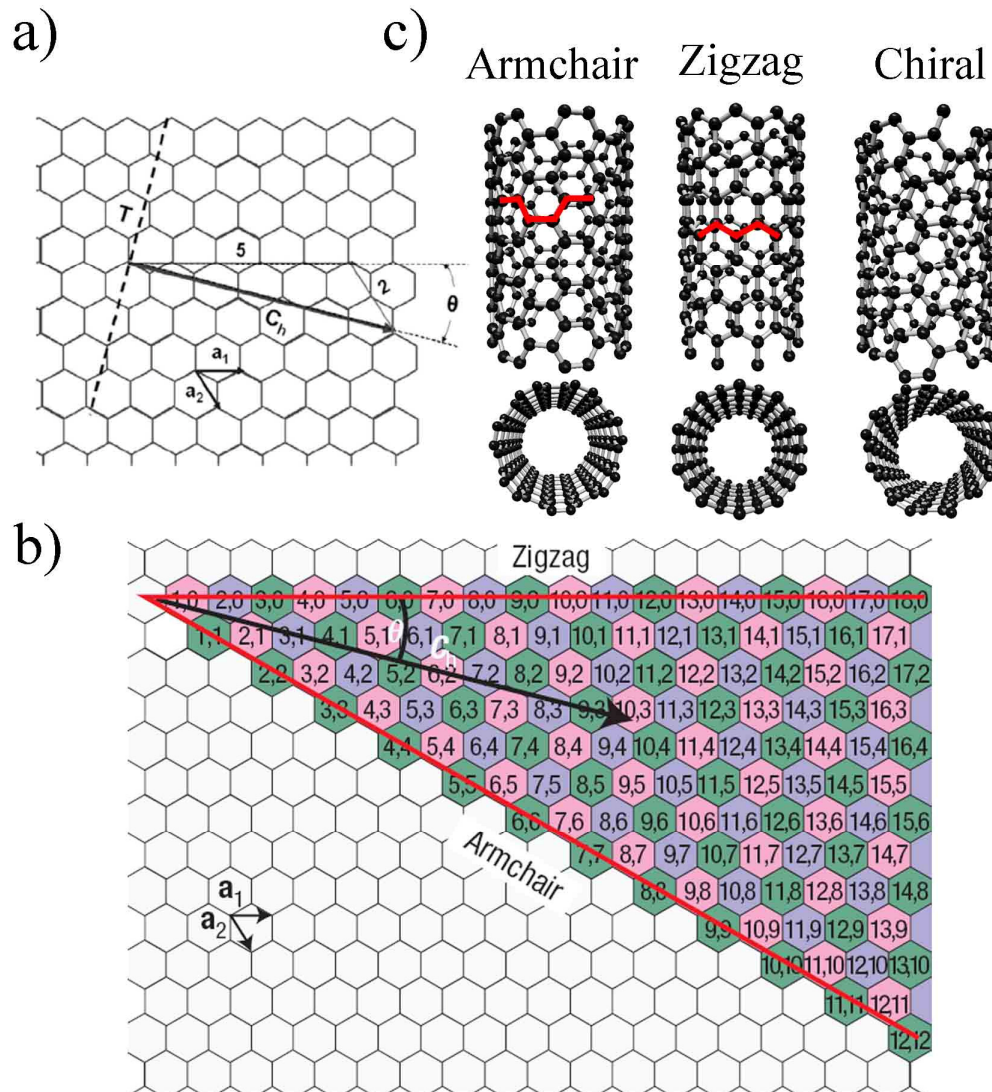


Figure 2.1: a) SWNTs are defined by warping a graphene sheet along the chiral vector. The circumference is defined by the C_h , where (m,n) is the chirality of the SWNT and a_1 and a_2 are unit vectors of the graphene sheet. b) θ is the chiral angle. For zigzag tubes θ is 0° , for chiral tubes θ is between 0° and 30° and for armchair SWNTs θ is 30° . These three types of the SWNT are shown in c) and the armchair as well as the zigzag structure is highlighted in red., adapted from [65]

One important structural parameter for this thesis is the diameter d of the SWNT.

$$d = \frac{\sqrt{3}a_{c-c} \sqrt{m^2 + mn + n^2}}{\pi} \quad (2.1)$$

It depends on the carbon-to-carbon bond length a_{c-c} (0.142nm) and the chirality (m,n) of the SWNT.

2.2 Electrical transport in SWNTs

Electrical transport in SWNTs is most important for sensor applications, in particular when the main sensing principle is based on the change of the electrical transport properties due to environmental influences. A short introduction into electrical transport in SWNTs is given in the following section.

2.2.1 Electronic properties of SWNTs

As described in the previous chapter, SWNTs are either metallic, small-gap semiconducting or semiconducting. Since graphene is a conducting layer, the warping of the graphene to a cylinder causes a band gap opening in the case of semiconducting and small-gap semiconducting SWNTs. This was first shown by tight binding calculations [127-129]. The calculations show that the width of the band gap is strongly diameter dependent and decreases by $1/d$ for semiconducting and $1/d^2$ for small-gap semiconducting SWNTs with increasing diameter as shown in Figure 2.2 [42].

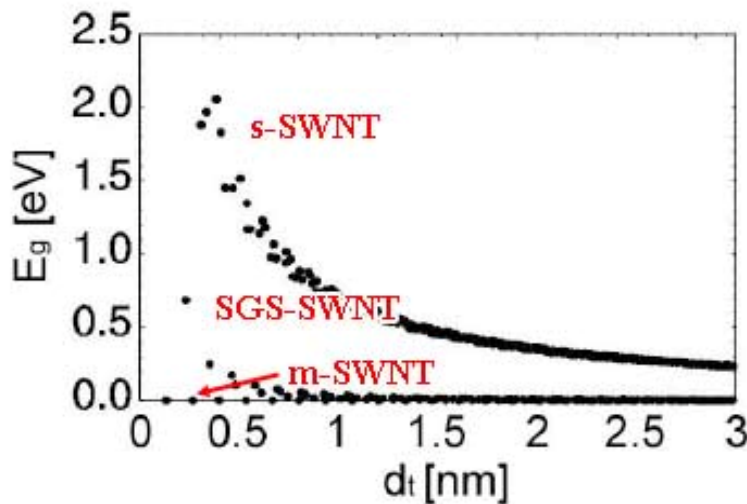


Figure 2.2: Diameter dependency of the band gap in SWNTs, adapted from [42].

Figure 2.3 shows the density of states of a (10,0) SWNT. Since this SWNT is semiconducting, no states occur between the valence and the conduction band in the band gap region (E_g). The characteristic peaks are called Van Hove singularities. The calculation of the densities of states for SWNTs is described in detail in the review paper of Charlier et al. [130].

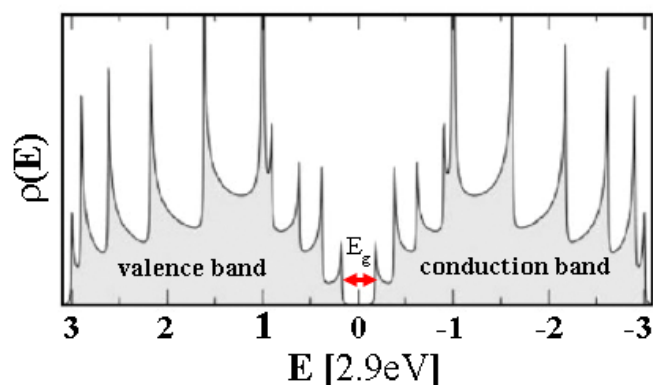


Figure 2.3: Density of states ($\rho(E)$) of a (10,0) semiconducting SWNT, adapted from [130].

2.2.2 SWNT based field effect transistors (CNFET)

As already mentioned in section 1.2.1 CNFET consist of a SWNT contacted by a source and a drain electrode as well as a gate electrode insulated from the SWNT by a dielectric. In an intrinsic CNFET the Fermi level is assumed to be in the middle of the gap and will be shifted towards the conduction band (electron conduction \rightarrow n-type) or valence band (hole conduction \rightarrow p-type) by applying a positive or negative gate voltage.

Figure 2.4 shows the sketch of an expected intrinsic CNFET source drain current response to a gate sweep (gate sweep measurement). At zero gate potential, the Fermi level is in the middle of the gap where the lowest current flow occurs. Unlike in MOSFETs, threshold values in CNFETs can sometimes not be determined due to significant off-state currents (especially SGS-SWNTs show high off-state currents) or bipolar gate sweep responses (as sketched in Figure 2.4). Wherever applicable, the position of the minimum current, defined here as “off-state potential”, was used in this thesis for Fermi level shift determinations. The saturation currents for hole and electron conduction are called p- on-state and n- on-state current, respectively.

Considering the whole CNFET system including SWNT channel and contacts, the current response of a gate sweep may not be fully determined by the SWNT alone. Ilani et al. [131] compared capacitance measurements with gate sweep measurements of the same device (Figure 2.5). While already small gate potentials led to a shift of the Fermi level into the first Van Hove singularity (Figure 2.3) determined by the measured charge load at the SWNT, the current remained still at off-state position in the gate sweep measurement. Only by shifting the gate potential further towards the second Van Hove singularity, currents started to flow through the SWNT channel, but the current increase at positive and negative gate voltages was not symmetric. A symmetric increase was expected because the capacitance measurements showed a symmetric charging of the SWNTs for positive and negative charge carriers.

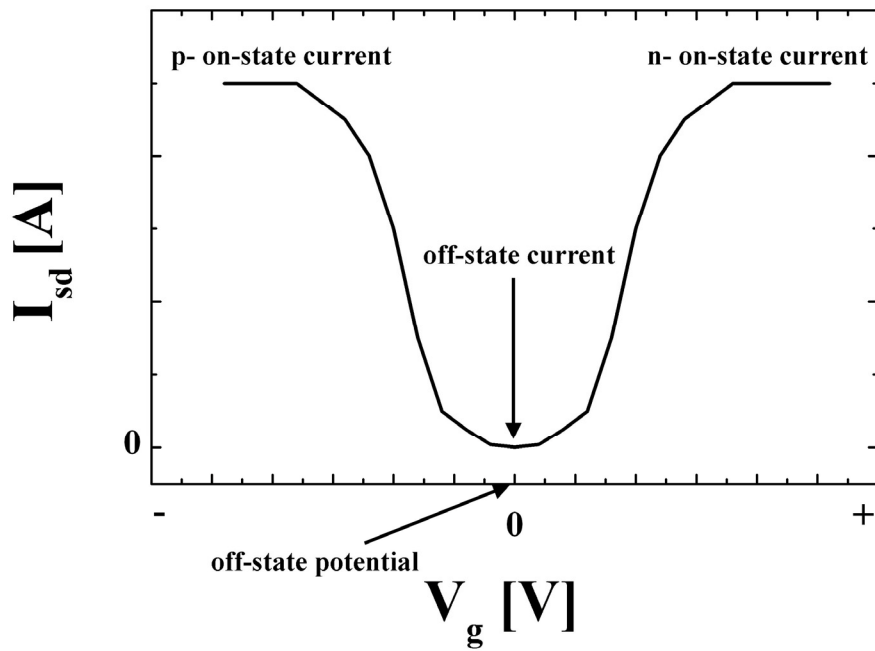


Figure 2.4: Sketch of an expected intrinsic gate sweep curve of a semiconducting SWNT.

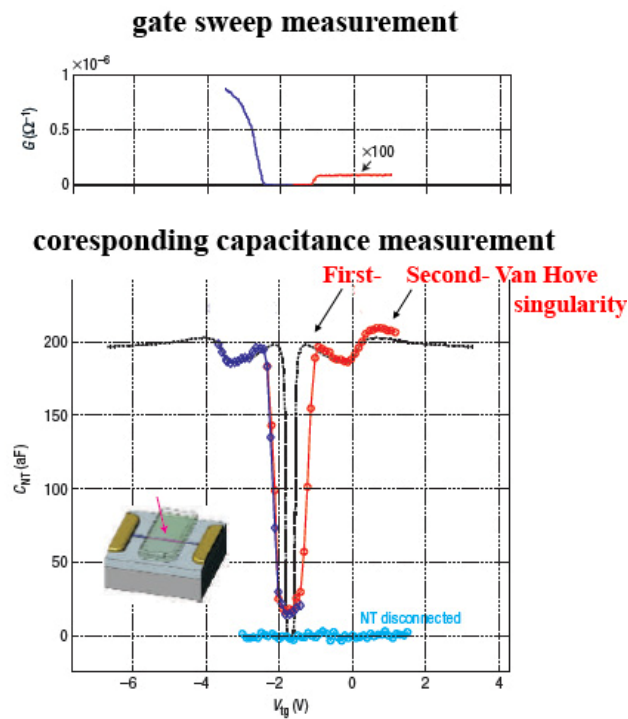


Figure 2.5: SWNT conductance and capacitance as a function of the top gate voltage. In the capacitance measurements the Van Hove singularities are pronounced, while they are suppressed by an additional mechanism in the conductance measurements, adapted from [131].

These results indicate clearly that a second mechanism in a CNFET system influences the gate voltage current response, which is responsible for the broadening of the gate sweep curve and for its asymmetric behavior.

It is well known that the s-SWNT-metal contact is a Schottky contact [132]. Therefore, two parts in the CNFET system are influencing the CNFET characteristics: First, the SWNT channel (field effect transistor behavior) and 2. the metal-SWNT contact (Schottky transistor behavior). Recently, Heller et al. [133] determined the influence of the contact part and the SWNT part on the gate sweep characteristic experimentally. They studied the change in the gate sweep characteristic in a biosensor CNFET setup as a function of the addition of two kinds of proteins. The first protein influences the work function of the contacts and the second one influences the Fermi level of the SWNT channel. With respect to these investigations, the influences of the contact part can be separated from the one of the SWNT part and the following conclusions can be made:

Influence of the SWNT Fermi level shift

In the first experiment it was observed that strong electronic gating by the adsorption of poly-L-lysine at the SWNT channel causes a potential shift of the whole gate sweep while the shape of the curve remained unchanged. Therefore, as shown in Figure 2.6 a), the shift of the off-state potential is caused by the shift of the conduction and valence band in the channel part relative to the Fermi level as depicted in Figure 2.6 b). Furthermore the contact part remains constant, because the metal work function has not been changed. Therefore, the curve maintains its shape and the on-state currents remain unchanged

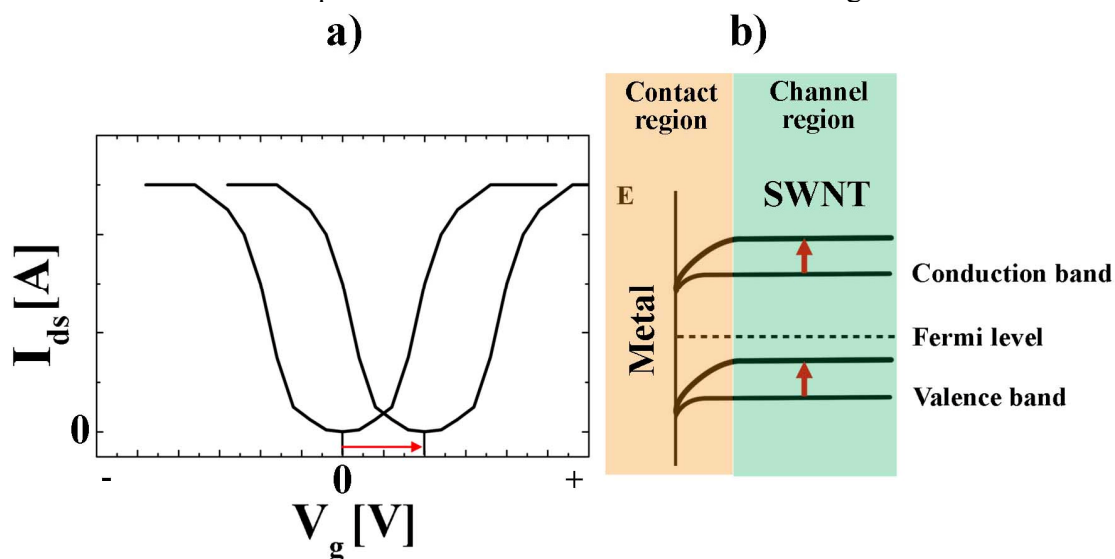


Figure 2.6: The shift of the off-state potential of a gate sweep measurement is caused by the shift of the conduction and valence bands relative to the Fermi level in the SWNT channel region. The position of the Fermi level does not influence the shape of the gate sweep curve.

Influence of the contact metal work function

In the second experiment, an increase of the n- on-state current and a decrease of the p- on-state current were observed upon to the addition of cytochrome-c to the system consisting of a CNFET with a very small channel length. The off-state potential remained unchanged. From this experiment the following mechanism shown in Figure 2.7 can be put forward. A modulation of the Schottky barrier in the contact region due to changes in the metal work function (for example caused by the adsorption of molecules on the contact metal) changes the depletion at the metal-SWNT interface and therefore the on-state current. With a shift of the depletion towards lower energies, the conduction band in the contact region gets closer to the Fermi level, which leads to an increase in the n- on-state current while the p- on-state current is reduced. However, the changes of the bands occur only in the contact area. The band positions relative to the Fermi level at the SWNT channel region remain unchanged. Therefore, changes in the contact metal work function have no influence on the off-state potential.

Influence of the SWNT band gap

The influence of the band gap on the CNFET performance has already been discussed in section 1.3.6. As shown in Figure 2.2, the band gap of a SWNT depends on its diameter. It has been shown that the diameter of the SWNT strongly influences the on-state current due to changes in the Schottky barrier height at the contact regions [49, 52] and the off-state current due to thermal activation of electrons (equation 1.1) as sketched in Figure 2.8. The influence of the size of the band gap on the threshold value and the sub-threshold slope has not been investigated yet.

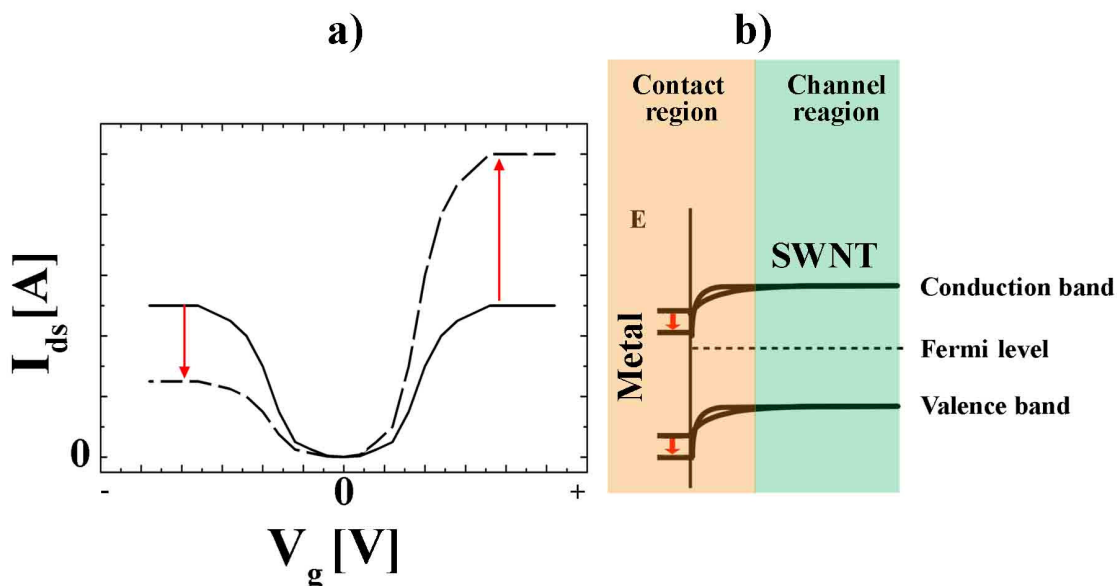


Figure 2.7: The change of the band depletion at the metal-SWNT contact results in the decrease of the p-on-state current and an increase for n-on-state current or vice versa. This modulation at the Schottky barrier of the CNFET is therefore responsible for asymmetric transistor characteristics. A change in the work function has no influence on the off-state potential.

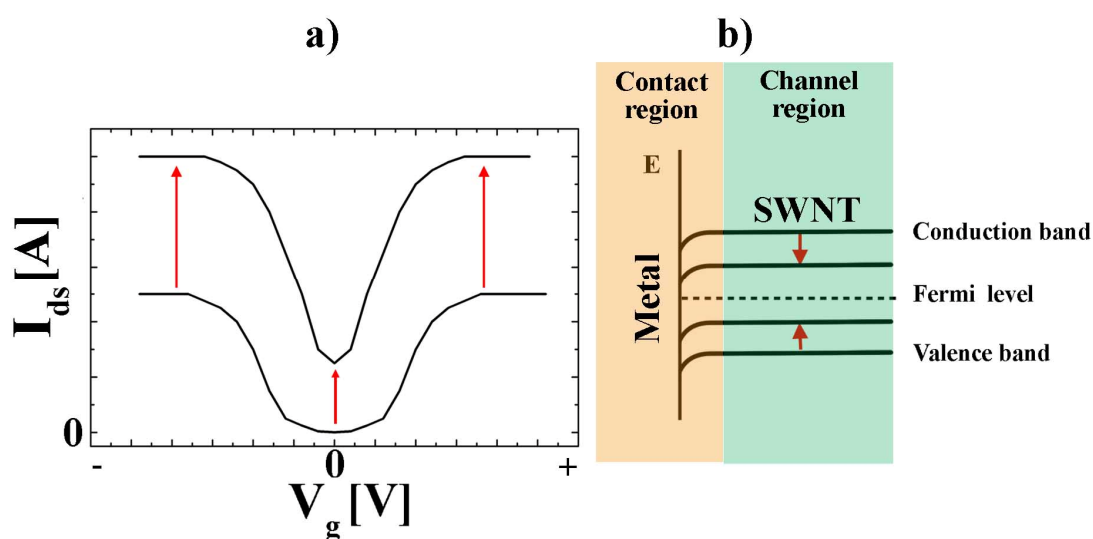


Figure 2.8: The influence of the band gap on the gate sweep characteristics. With decreasing band gap, the off-state current increases due to enhanced electron tunneling according to thermal activation and the on-state currents increase due the decrease of the Schottky barrier height in the contact region.

2.3 SWNT synthesis

SWNTs were first synthesized by thermal chemical vapour deposition (CVD) of benzene together with hydrogen using Fe catalysts in 1976 [134]. However, by that time they were identified as carbon fibers. Twenty years later, Iijima et al. [4] and Bethune et al. [5] were able to synthesize SWNTs by arc-discharge using Fe and Co catalysts, respectively. In 1996, SWNTs were synthesized for the first time by laser ablation [55]. Also in 1996, the same group was able to synthesize SWNTs by CVD of carbon monoxide on Mo catalysts [56]. Based on the CVD process, Nikolaev et al. [94] investigated a process where SWNTs were synthesized at high pressure and with floating catalysts (HiPCO process).

In this chapter, these techniques are described and their advantages and disadvantages are discussed. Further, the basics of SWNT formation are described and followed by a new model, which describes the impact of pressure, temperature, catalyst, gas composition, etc. on the nucleation and growth of SWNTs by CVD. Finally, the protein Ferritin and its iron uptake and release functions are introduced.

2.3.1 SWNT synthesis techniques

Arc discharge [15, 135]

The basic setup of an arc discharge growth apparatus is shown in Figure 2.9. In a chamber filled with He two graphite electrodes (anode and cathode) are located. For the synthesis of

SWNTs the anode is doped with catalyst material. By applying a voltage to the electrodes, they discharge in a light arc (plasma) with optimal SWNT formation currents of 40-100A. In this processes temperatures up to 3000°C are reached, which causes the evaporation of carbon inside the plasma. The carbon atoms condensate from the gas phase, form SWNTs and are collected at the cathode.

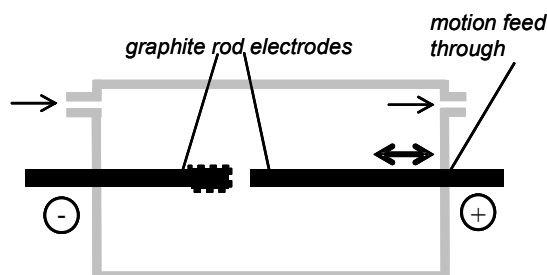


Figure 2.9: Schematic of the basic setup for SWNT growth by arc discharge.

The high temperature allows the formation of highly crystalline SWNTs in large scale (45g/h) with narrow diameter distributions. However, maintaining stable discharge conditions is challenging and therefore reproducibility in yield and length of the SWNTs has not been achieved yet. The major drawback of this method is that only SWNT bundles can be produced and that byproducts including fullerenes, amorphous carbon and graphitic polyhedrons with enclosed metal particles can not be avoided requiring purification and bundle splitting methods.

Laser ablation [15, 135]

In this method, carbon atoms are evaporated in an inert atmosphere from a graphitic substrate doped with small quantities of transition metals by the irradiation of a laser. High yield of SWNTs is achieved in a heated flow tube at operation temperature around 1200°C, as sketched in Figure 2.10.

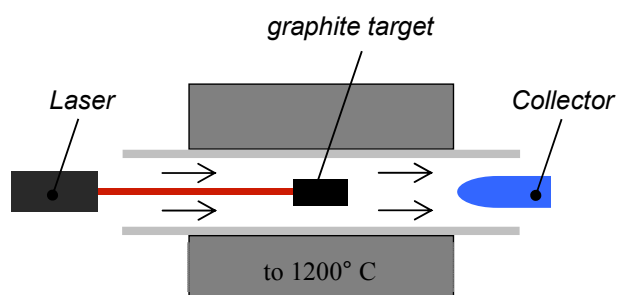


Figure 2.10: Schematic of a laser ablation setup consisting of a heated flow through tube.

This method yields SWNT bundles with low defect densities and narrow diameter distributions. However, the amount of SWNTs which can be produced in a day is lower than with the arc discharge method. Additional drawbacks are the necessity of post purification and bundle splitting steps.

Chemical vapour deposition (CVD) [15, 135]

Today's most common method for the synthesis of SWNT is the growth by CVD. Different to the previously described methods, SWNTs are grown at lower temperatures (400°C - 1000°C) and an organic gas is used as carbon source (CH₄, C₂H₄, C₂H₅OH, CO, etc). The carbon source gas is dissociated on a catalyst nanoparticle to yield pure carbon atoms as raw material for the synthesis of the SWNTs. A common SWNT growth setup is illustrated in Figure 2.11.

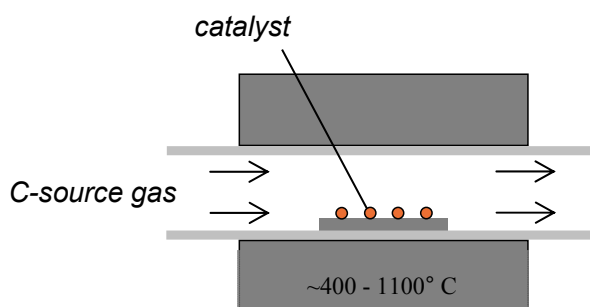


Figure 2.11: Conventional CVD setup based on a tube furnace.

In this particular case it consists of a heated flow tube where the substrate with the catalyst can be placed. During the growth process the carrier and reaction gases propagate through the tube and adsorb on the catalyst surfaces.

Mono-, bi- or multi-metal catalysts of transition metals (Fe, Ni, Co, Cu, Mo, Co-Mo, Co-V, Fe-Mo, Co-Ni, etc.) are mainly used for CVD growth of SWNTs. Beside the catalysis of the dissociation of the carbon source the catalyst has an important role as shaping and stabilizing structure in the SWNT formation process. Therefore, the SWNT diameter depends strongly on the size of the catalyst particle as sketched in Figure 2.12.

CVD synthesis is the most flexible SWNT growth method. Many parameters (e.g. temperature, partial pressure of the feed stock gas, partial pressure of additional gases, flow rate, catalyst type, size and amount and growth time) can be tuned to optimize yield, length, density, quality and diameter of the SWNTs. Therefore, several CVD methods for SWNT growth have been developed. Reduced pressure (LPCVD) and ethanol based CVD allow the growth of SWNTs with low defect densities and low amorphous carbon contaminations [61, 136], while the growth of high quality amorphous-free SWNT forests has been achieved by water assisted CVD [60]. Plasma enhanced CVD allows the growth of only semiconducting SWNTs at reduced temperatures [40, 137] (which might be the result of introduced defects by the plasma (see section 1.3.2).



Figure 2.12: The catalyst particle acts, in addition to catalyzing the dissociation of the carbon source gas, as shaping and stabilizing element. Therefore, the diameter of the growing SWNT depends on the size of the catalyst particle.

High-pressure CO conversion (HiPCO) [15, 135]

This special CVD-based production method involves the thermolysis of floating $\text{Fe}(\text{CO})_5$ in the presence of CO at elevated temperatures (1000-1100°C) and pressures (>10bar) as shown in Figure 2.13.

This method allows the SWNT production in bulk amounts with narrow diameter distributions and mean diameters around 0.7-1.2nm. However, similar to the arc discharge and laser ablation techniques, amorphous carbon formation and bundle formation can not be avoided, requiring mandatory purification and separation.

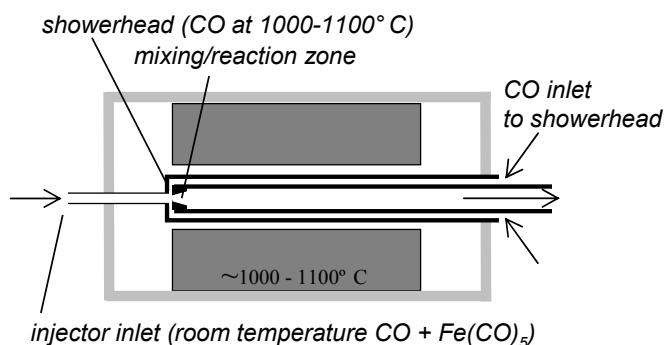


Figure 2.13: HiPCO SWNT synthesis furnace.

Purification and separation of SWNTs

The major drawback in bulk and large scale SWNT production methods is the requirement of purification processes to remove catalyst particles and amorphous carbon deposits and the subsequent splitting of the bundles in presence of surfactants.

Several purification processes have been investigated so far. Most of them include etching of the amorphous carbon (eg. by HNO_3) and catalyst particles (eg. by HCl) by acid in

combination with annealing steps [135]. However, the acid does not only react with the unwanted species around the SWNTs but also the SWNTs themselves causing undesired defects.

More serious problems causes the use of detergents in combination with ultrasonic treatment for the splitting of bundled SWNTs and for making them soluble [76]. This dissolution step is mandatory for controlled integration of SWNTs in devices. Most common surfactants are sodium dodecyl sulphate (SDS) and sodium dodecylbenzene sulphonate (SDBS). These detergents show strong adhesion to the SWNTs and can hardly be removed. Therefore, contact resistances of such treated SWNTs are 2 to 100 times higher than high quality SWNTs directly grown on the substrate. As an example, system resistances of $\sim 100\text{k}\Omega$ to several $\text{M}\Omega$ for SDS coated HiPco grown SWNTs were measured, while SWNTs directly grown on the substrate by CVD show system resistances from $\sim 30\text{k}\Omega$ to $\sim 300\text{k}\Omega$ (see state-of-the-art Table 1.4). Integration method and contact materials were equal for all measurements.

2.3.2 SWNT growth model

Already in the early stage of SWNT growth investigation, the vapour-liquid-solid model (VLS) was used to explain their formation process [139-140]. This model is well known from Si whisker formation [141] and has been adapted for the growth of SWNTs. According to this model, dehydrogenated carbon atoms are absorbed in a metal catalyst nanoparticle. When the temperature of the catalyst decreases, a super saturation occurs leading to the formation of a fullerene-like layer on the catalyst (a spherical carbon structure consisting of hexagons and pentagons). The formation of an initial graphene layer around the catalyst is confirmed by *in situ* TEM investigations in the carbon fiber nucleation process shown by Helveg et al. [142]. At elevated temperatures, this layer can be released from the catalyst. This process step is called cap formation or nucleation of the SWNT. Afterwards, the SWNT grow by incorporating freshly dissociated carbon atoms at the base of the SWNT. This model is widely accepted in the community today. However, it is known that the catalyst does not need to be liquid for the propagation of SWNT growth [143] and that a super-saturation stage can also be reached by steadily increasing the amount of carbon atoms at the catalyst particle [144].

The molecular dynamic simulation studies based on the VLS model made by Zhao et al. [144] explain the different steps of the SWNT formation by CVD of CH_4 nicely (Figure 2.14). High resolution TEM images of SWNT nucleation made by Zhu et al. [145] support and illustrate the different formation steps additionally.

1.

In a first step, the carbon feed stock gas is adsorbed on the catalyst surface, where it dissociates into carbon and hydrogen atoms.





In a side reaction, the hydrogen radicals form molecular hydrogen, which desorbs from the surface.

**2.**

The carbon atoms diffuse into the catalyst and on the catalyst surface. With increasing amount of the free carbon atoms in the catalyst, they start to form carbon chains on the surface of the catalyst particle.

**3.**

Carbon atoms are added to the chain, which leads to the formation of carbon sheets consisting of pentagons, hexagons and heptagons [146] until the particle surface is covered by a single layer of this fullerene-like carbon. At elevated temperatures, supported by the catalytic activity of the nanoparticle, bonds easily break and rebond. Consecutively carbon atoms can be incorporated in the carbon layer, resulting in a continuous reformation of its structure.

4.

Driven by the increasing amount of carbon atoms in the particle and by the elevated temperature, the fullerene-type of structure can lift off the catalyst particle, which results in the formation of a cap. This step is also called nucleation. So far, all the steps were reversible. Since the single carbon layer is no longer fully attached to the catalyst, the nucleation is an irreversible step. Nevertheless, at temperatures above 800°C, C-C bonds still break and rebond [144]. During this annealing step, the defects in the SWNT structure are reduced. The efficiency of the annealing increases with increasing temperature.

5.

After the cap formation, the SWNT grows by the incorporation of freshly catalyzed carbon atoms at the catalyst site.

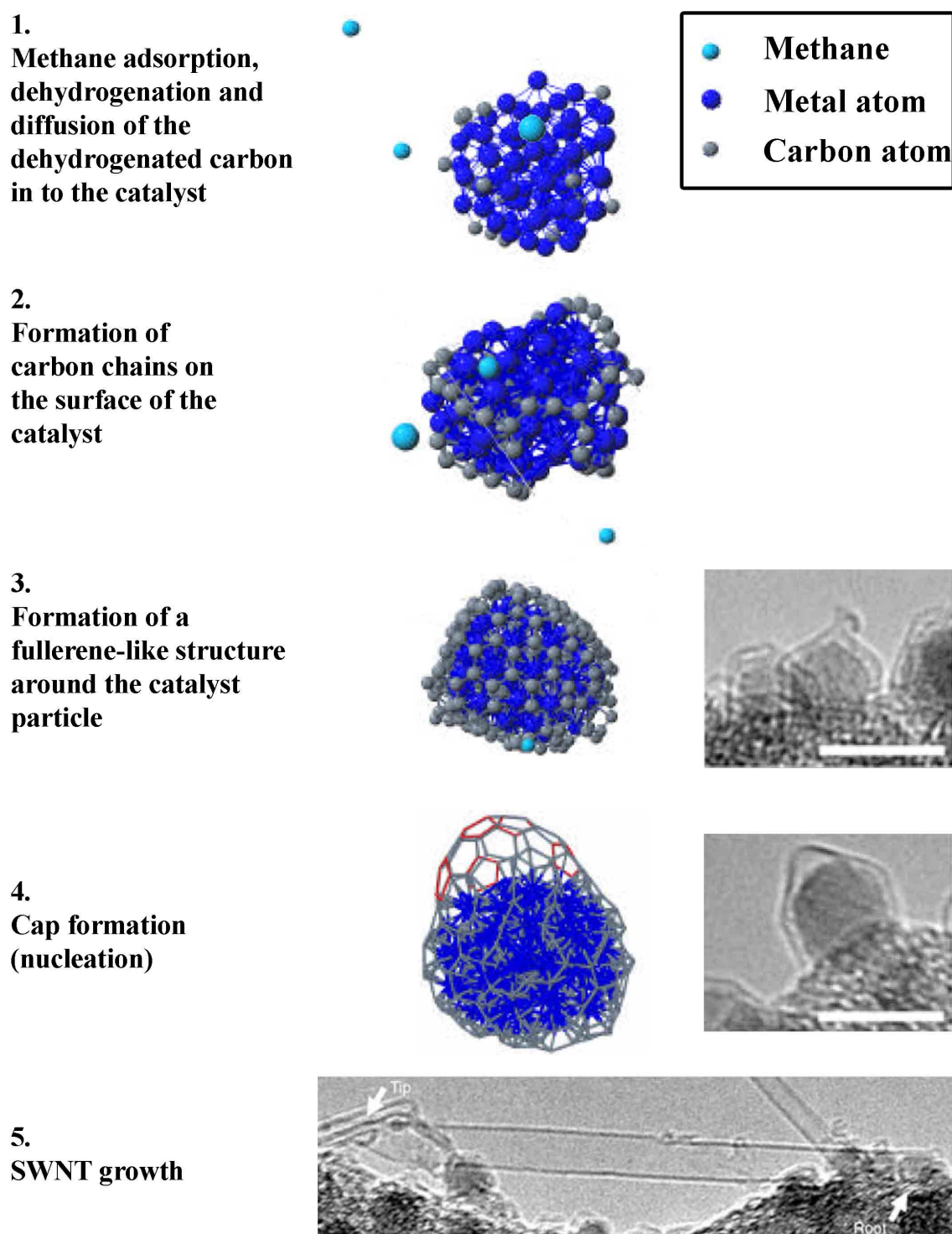


Figure 2.14: Enhanced VLS model describing the nucleation and the growth of SWNTs in five steps, adapted from [144-145] (scale bare dimensions were not mentioned in the corresponding publication but according to other TEM images in that publication it is assumed to be ~2nm).

2.3.3 Thermodynamic and kinetic considerations in SWNT growth

In the CVD growth of SWNTs, there are many parameters (e.g. carbon source type, catalyst type, H₂ pressure, carbon source pressure, gas flow rate, temperature, growth time, etc.), which influence the nucleation yield, density, diameter, quality and cleanliness of the SWNT. Some of these parameters and their influences on the SWNT growth are listed in Table 2.1. Some of the referred publications only show the amount of deposited carbon, which is the sum of amorphous carbon and SWNTs determined by weighing the products after growth.

Table 2.1: Influence of process parameters on the growth of SWNTs by CVD (↑ = increase)

Parameter		Influences on the..		Reference
CH ₄ /H ₂ ratio	↑	SWNT diameter	↑	Lu (2006) [98]
CH ₄ /H ₂ ratio	↑	Amorphous carbon formation	↑	Jungen (2007) [54]
CH ₄ /H ₂ ratio	↑	yield of carbon material	↑	Nagy (2004) [147]
Temperature	↑	SWNT diameter	↑	Cheung (2002) [86]
Temperature	↑	Amorphous carbon formation	↑	Javey (2002) [148]
Temperature	↑	yield of carbon material	↑	Jungen (2007) [54]
Temperature	↑	yield of carbon material	↑	Nagy (2004) [147]
Catalyst activity	↑	yield of carbon material	↑	Nagy (2004) [147]

Methods explaining the influences of the CVD parameters on the SWNT growth have been presented in both, thermodynamic [149] and kinetic approaches [150-152].

Wagg et al. [149] showed a thermodynamic model based on the Gibbs free energy (ΔG) for the determination of the SWNT formation threshold value. In this publication, pseudo equilibrium between the SWNT formation and the back reaction of the carbon source (CH₄) was assumed. Therefore, the standard Gibbs formation enthalpy ΔG^*_{SWNT} was determined over the relation:

$$\Delta G^*_{SWNT} = -RT \ln \frac{p_{H_2}^2}{p_{CH_4}} \quad (2.6)$$

where R is the gas constant, T is the temperature and p_{H_2} and p_{CH_4} are the partial pressures of hydrogen and methane, respectively. The SWNT nucleation takes place at higher energy than the formation of SWNTs after the nucleation occurred. Therefore, a driving force $\Delta G'$ was introduced, without further specification. If this driving force is high enough (for example at increased methane concentrations), the nucleation of SWNTs and graphitic carbon takes place. However, a correlation between the poisoning of a catalyst (amorphous carbon formation) and the nucleation of a SWNT was not distinguished by the authors.

The kinetic model of Perez-Cabero et al. [152] considers the influence of the CH_4 and H_2 partial pressures as well as the temperature on the reaction constants and therefore the growth velocity of SWNTs. A relation between the nucleation of SWNTs and the carbon formation velocity on the catalyst surface was assumed but not described in detail. All other kinetic models are mainly focusing on the SWNT growth velocity and SWNT termination, which is rather important for large-scale SWNT synthesis than for the understanding of the SWNT nucleation.

A model explaining the influence of all these parameters on the SWNT nucleation hence on the SWNT yield and diameter does not exist to my best knowledge.

A novel qualitative model was determined by combining thermodynamic and kinetic considerations. Since experimental data for the verification of this model are missing yet, this model is given in the appendix. Therefore be referred to the appendix.

2.3.4 Ferritin: A protein helps to form the catalyst nanoparticle

Ferritin is a Fe storage protein, which was first introduced for Fe catalyst particle formation by Li et al. [71]. In their process, apoferritin (the empty ferritin protein) was loaded with Fe and then adsorbed on a SiO_2 surface. Subsequently, the protein shells were oxidized and the remaining particles were calcined, which led to the formation of Fe_2O_3 (hematite) nanoparticles. From these nanoparticles, SWNTs were grown by CVD directly on the surfaces.

The use of Ferritin proteins for catalyst nanoparticle formation has several advantages:

- Easy handling
- Low cost wet chemistry process
- Overall protein charge prevents the protein from aggregation → formation of well separated catalyst particles on the surface
- Adjustment of catalyst size via the amount of loaded Fe in the ferritin cavity

Due to these advantages, ferritin was used for catalyst formation in this thesis. Therefore, a short introduction of this protein with main focus on the Fe uptake function is given in this section.

Ferritin, illustrated in Figure 2.15 a), is an iron storage protein, which uptakes ferrous ions (Fe^{2+}) and stores them as ferric ions (Fe^{3+}) in its core. In mammalian metabolism the most important is the oxygen binding and release in hemoglobin. Therefore, a mammalian body requires an appropriate amount of iron in its soluble Fe^{2+} -state. However, because of the toxicity of a too high iron concentration ferritin acts as regulator. It takes up and stores iron at high concentrations and releases it in case of low concentration [153-156].

Ferritin is a large protein consisting of 24 helical protein subunits (Figure 2.15 a). It has an outer diameter of 8-12nm and the core diameter is 6-8nm, depending on the type of ferritin. It can store up to 4500 Fe atoms in the form of mono crystalline ferrihydrite [155]. It is assumed that free Fe^{2+} is guided to the threefold channel entry by an electrostatic field. Figure 2.15 b) shows the charge distribution on the protein surface. The electrostatic field is additionally highlighted by the yellow field lines [157].

After the entering of two ferrous ions into the catalytic center shown in Figure 2.15 c), they are complexed by different amino acids (2.20) and oxidized to a peroxy intermediate (2.21) followed by a hydrolysis to a μ -oxobridged complex (2.22). With an additional water molecule the μ -oxobridged dimer is split into two stable monomeric $[\text{Fe}(\text{OH})_2]^+$ ions. Ferric ions leave the catalysis sites in an oxo/hydroxo bridge to the cavity [158].

Glutamates are assumed to be involved as ligands in the translocation of iron from the ferroxidase center to the cavity followed by incipient ferrihydrite nucleation [158].



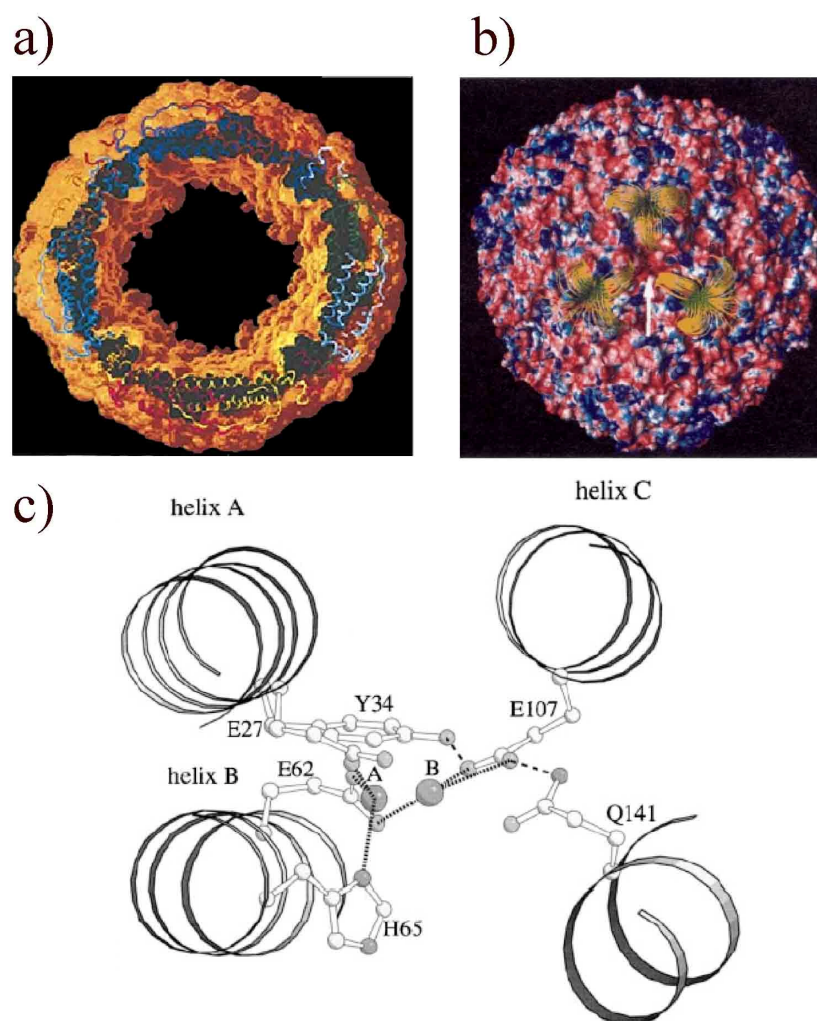


Figure 2.15: a) Profile of a ferritin protein with an inner core diameter of 8nm. b) The yellow lines show the electrostatic field lines guiding Fe^{2+} ions to the threefold iron entry (positively charged regions are colored blue and negatively charged region are colored red). c) Active site of the protein located in the human Hanukah factor (HuHF) unit. In the dinuclear ferroxidase center Fe^{2+} ions are complexed. Adapted from [154, 157-158].

3 Experimental

In this chapter, all experimental details for sample preparation, SWNT growth, catalyst islands and electrode structuring by UV lithography and the used analysis methods are given. The objective of this chapter is to provide documentation for the reproduction of the performed experiments.

The process flow for the ferritin catalyst preparation and adsorption on the SiO_2 surface and CVD growth of SWNTs are shown in Figure 3.1. This process was adapted from Li et al. [71] and was published in the journal sensors and actuators [96]. Apoferritins (empty ferritin proteins) were loaded with Fe^{3+} in a solution containing Fe^{2+} ions (a). After dialysis (b) the proteins were adsorbed on the sample surface (c). Then the protein shells were oxidized and the ferrihydrite particles were calcined (d). The remaining Fe_2O_3 nanoparticles were reduced to Fe in the CVD chamber by H_2 treatment at elevated temperature (e). Subsequently, SWNTs were grown from the catalyst particles by the use of CH_4 as feed stock (f). The development of the CVD growth process was published in [54]. This sample preparation process is discussed in sections 3.2 and 3.3 and SWNT growth is described in section 3.5.

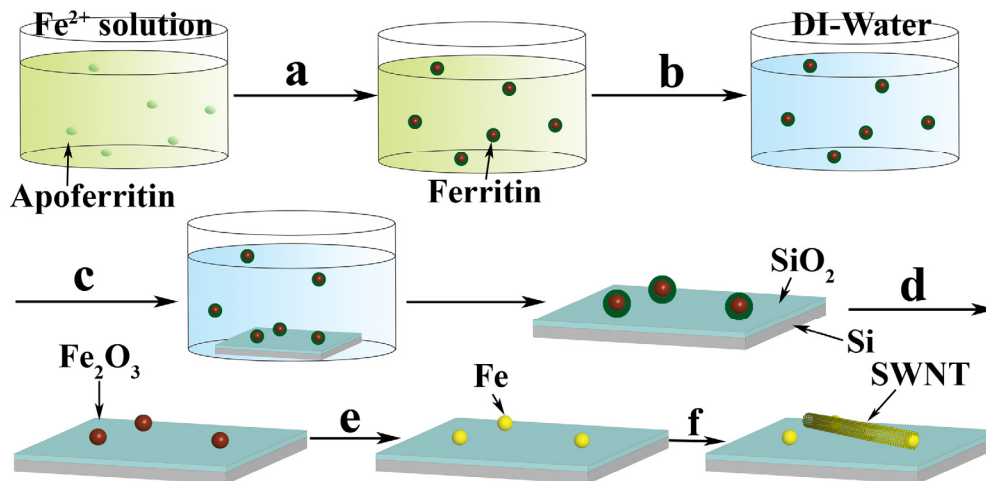


Figure 3.1: Process flow of SWNT growth by the use of ferritin-based Fe catalysts: a) apoferritin loading at 50°C , b) dialysis for 24h and centrifugation for 15min at 14,000g, c) ferritin adsorption on 200nm thick gate oxide, d) oxidation of the organic protein shell at $>800^\circ\text{C}$ for 1-5 min in air, e) reduction of the Fe_2O_3 particles under H_2 atmosphere at 850°C for 10min, f) SWNT growth at 850°C from CH_4 source gas [96].

In order to reduce the catalyst diameter distribution and to obtain better control over the mean catalyst diameter, a new method was developed for catalyst separation according to their size. Shortly, ferritin proteins were loaded on top of a viscous medium (glycerol) and then centrifuged in an ultra centrifuge at high centrifugation forces for ~17h. Thereby the protein sediments towards the bottom of the centrifugation tube with velocities which are dependent on the size of the encapsulated catalyst nanoparticles. Fractions were collected after centrifugation containing catalyst particles with reduced size distributions. This investigation was submitted to the journal nanotechnology [159] and is described in section 3.4.

The CNFET production process based on e-beam lithography and metal evaporation is shortly explained in section 3.5. For a detailed discussion of the process refer to [30].

In section 3.7, the process parameters which have been determined for the fabrication of CNFETs in large scale are given. The process is shown in Figure 3.2 and consists of the following main steps: 1. UV lithography and subsequent RIE etching of the markers into the SiO₂ layer or, as depicted in the Figure, by metal evaporation and lift-off. 2. UV lithographical structuring of patterned growth islands, ferritin adsorption, lift-off and catalyst calcination. 3. SWNT growth from the catalyst particles. 4. Electrode structuring by UV lithography, metal evaporation and lift-off. 5. Optional post fabrication processes like cleaning and annealing steps and device protection by atomic layer deposition (ALD) of Al₂O₃, or the fabrication of suspended SWNTs by a HF etching dip.

In the last section, the analysis methods are described in detail.

3.1 General considerations

- For all the vessel cleaning, sample cleaning and solution preparation distilled water (DI water) with a resistivity >18MΩcm have been used.
- Frequently used chemicals: 1-Methyl-2-pyrrolidone (NMP) (C₅H₉NO, 99.5%, Fluka), acetone (C₃H₆O, >99.5%, Fluka), isopropanol (C₃H₈O, >99.8%, Fluka), apoferritin (53 mg/ml, Sigma)⁴ and ferritin (50-150 mg/ml, Fluka).
- Glassware in the chemistry lab has to be cleaned prior to the experiments. Metal ions and organic compounds adsorbed on the side walls can affect the experimental results drastically. The glassware was cleaned in a Piranha solution. Therefore a large beaker was filled with concentrated H₂SO₄ (95-97%, Fluka) and then H₂O₂ (30%, Ridel-de

⁴ Only yellowish apoferritin was used. Green or black apoferritin solution consists of aggregated proteins and was sent back to Fluka

Haen) was slowly added until the beaker became hot (bubble and vapour formation). Then all the glassware was put into that solution for 10min. Subsequently the glassware was rinsed with DI water for 5min.

- All investigations were performed equal substrates (wafers from the same production run with the same doping level, which were oxidized in the same oxidation run and stored at the same place) because a change in the surface energy and morphology does not only change the protein adsorption behavior but also the growth of SWNTs and the structuring processes by UV lithography.

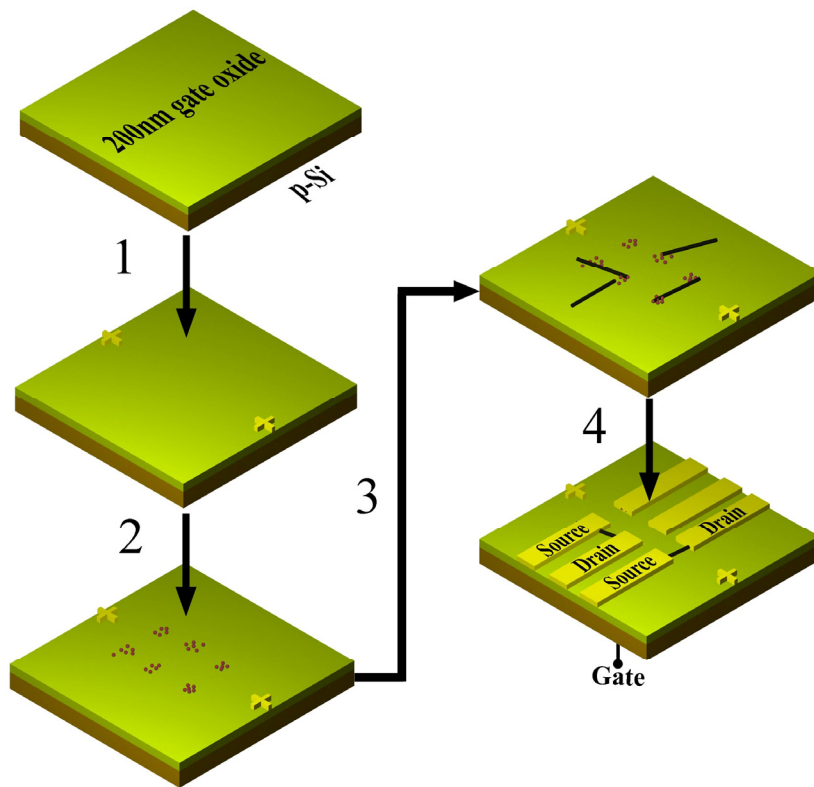


Figure 3.2: Sketch of the process flow for the SWNT integration by UV lithography. 1. Patterning of alignment markers by UV lithography, metal evaporation and lift-off or RIE etching into the SiO₂. 2. Patterning of Fe catalyst nanoparticle by ferritin adsorption into pre patterned photoresist moulds and lift-off. 3. Growth of SWNTs from the ferritin-based catalysts. 4. Electrode structuring on top of the SWNT growth pattern by UV lithography, metal evaporation and lift-off.

3.2 Substrate preparation

For all experiments, highly p-doped 500 μm thick Si with 200nm thermally grown SiO_2 (dry oxide) was used. The oxidized 6-inch Si wafers were obtained from the Institute for Microelectronics in Stuttgart. For protecting the surface during dicing, the wafers were covered by a photoresist (Microposit S1813, Shipley) and baked for 2min at 100°C. First, the wafer was mounted on blue tape and diced in 4 pieces (dicing saw 8003, European Semiconductor Equipment Center). One wafer piece was then mounted upside down on the blue tape again. The piece was only diced half through from the back side (blade to chuck distance 300 μm , which leads to ca 290 μm deep trenches in a 500 μm wafer) into 4x4mm² dies. This has the advantage of reduced surface contaminations during dicing and batch processing during subsequent sample cleaning. In a next step, the photoresist was stripped by first dipping the wafer piece in a beaker of cold acetone to remove most of the photoresist, followed by cleaning the wafer piece in fresh acetone at 50°C for 10min. Subsequently it was transferred into fresh isopropanol for 5min, followed by a 5min immersion into DI water. Then it was carefully blown dry with N_2 on a clean room towel. In this stage no more photoresist could be observed optically on the surface. However, AFM images showed that there were still residuals remaining on the surface. To remove these residuals, cleaning of the chip in NMP at 60°C for ~70h would be required. In order to reduce this time, the wafer piece was put on a glass ceramic plate which was heated by a Bunsen burner until the whole surface was glowing. This led to the immediate oxidation of all organic remainings on the surface. For further use, the wafer piece was broken in 4x4mm² chips and in case of further use for UV-lithography based integration processes into 16x16mm² chips, which could be broken in smaller chips if needed. A cleaned 4x4mm² chip is shown in Figure 3.3.

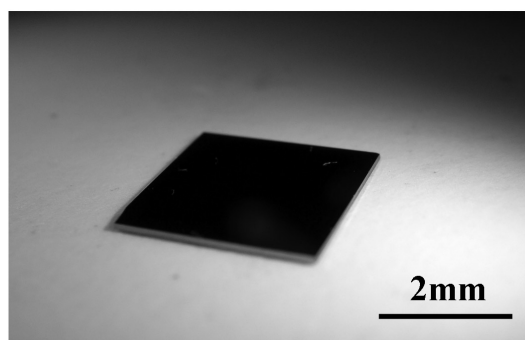


Figure 3.3: Highly p-doped Si chips with 200nm thermally grown SiO_2 on top were used for SWNT growth investigations.

Figure 3.4 shows a top view and a 3D view AFM image of a cleaned thermally grown SiO_2 surface. In all the investigations chips from the same wafer slot were used and therefore the surface of Figure 3.4 is representative for all surfaces which were used in the experiments.

The arithmetic average of all points on the surface (R_a) measured in an area of $10 \times 10 \mu\text{m}^2$ is 0.23nm (surface roughness).

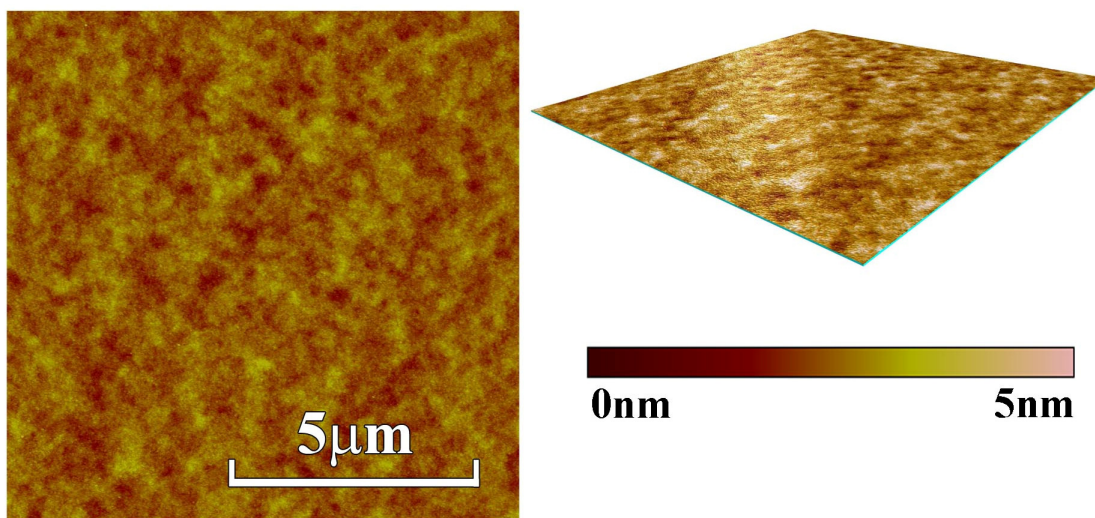


Figure 3.4: AFM image top view and 3D view of a clean substrate surface, $R_a = 0.23\text{nm}$.

3.3 Catalyst preparation

Table 3.1 shows three different apoferritin loading processes resulting in different catalyst particles sizes. In the following section, the preparation process for the catalyst nanoparticle formation on the SiO_2 is described. Equine spleen apoferritin (in order to avoid contamination of the solution, which can cause mildew, the protein was collected with a sterile needle) was added to a 25ml 50mM 2-(N-morpholino)ethanesulfonic acid (MES) (99.5%, Fluka) solution. The solution was previously adjusted to pH 7.1 by adding 1M NaOH solution (sodium hydroxide monohydrate, >99.99%, Fluka). The temperature during the loading of the apoferritin was kept constant at 50°C . After the loading temperature was reached, 25 mM freshly prepared ammonium ferrousulfate hexahydrate solution (Fluka, ultra) and 25mM trimethylamine N-oxide dihydrate (Fluka, purum) was added to the solution. For each addition a new pipette tip was used.

For the formation of particles with sizes from 1 to 3nm (process #1 and #2 of Table 3.1) iron and oxidation solutions were only added in the beginning, while for the formation of larger particles (#3 of Table 3.1) it is recommended to make several additions during the whole loading time.

In some experiments, commercially available saturated ferritin proteins were used. For the preparation of a stock solution of already loaded Ferritin, 0.25ml-1ml iron saturated horse spleen ferritin were added to 25ml DI water.

Table 3.1: Apoferritin loading parameters

Process ID #	Ferritin solution (ml)	Fe ²⁺ and oxidation solution (ml)	First addition (min)	Second addition (min)	Third addition (min)	Ferritin loading time (min)	Fe ₂ O ₃ particle size (~nm)
1	0.4	0.25	0	-	-	30	1-2.5
2	0.4	0.25	0	-	-	45	2-3
3	0.75	1	0	30	60	90	3-5

In order to avoid protein aggregations both, the home loaded and the commercial available ferritin solutions were dialyzed against DI water for at least 24h at 4°C in a 5l beaker⁵. The DI water was exchanged twice. After dialysis, the solution was centrifuged at 14,000 g for 15 min and the supernatant was stored at 4°C for further use. The centrifugation pellet contained undesired protein aggregations. Even better results were obtained by centrifuging the protein sample for 60min.

Prior to each use, the quality of the ferritin solution was checked by adsorbing the proteins on the surface and determining the resulting protein or particle surface density. If the density was drastically reduced in comparison to previous measurements, ferritins were aggregated and the solution could not be used any more (sometimes it helped to centrifuge the protein solutions again).

As recently recognized, for long term stability it is best to store the protein solution in the non centrifuged stage. Prior to use, a small amount of solution can be centrifuged. Therefore the solutions can be used for several months.

Remark: It might be interesting to find out whether there is a way to split apart aggregated proteins by moderate ultrasonic or other treatments!

For the Fe₂O₃ particle formation, Ferritin was adsorbed on highly doped Si chips covered with 200nm of thermally grown SiO₂. The chips were dipped into the prepared and further diluted (see results) ferritin solution for 1min, followed by a DI water dip for 1min. Subsequently, the chips were blown dry by N₂. The adsorption was carried out at room temperature.

The protein shells were oxidized and the remaining ferrihydrite particles were calcined at high temperature (T>800°C) on a glass ceramic plate heated by a Bunsen burner for approximately 1 min in ambient air.

⁵ Dialysis is important for reducing the ion content in the solution. Fewer ions in the solution increase the coulomb repulsion between the proteins and therefore the proteins have a lower chance to aggregate

3.4 Catalyst size separation

Both types of the described ferritin solutions were used for the following investigations. In order to remove large protein aggregates, the ferritin was centrifuged at 20°C for 15min at 25,000g. For sedimentation velocity separations, Beckman centrifuge tubes (part no. 331372) were prepared by layering 4ml 20% (v/v) glycerol on top of 7ml 60% (v/v) glycerol. To form a glycerol gradient, the tubes were sealed with parafilm and then tilted smoothly to a horizontal and back to a vertical orientation in approximately 5s. Next, approximately 1 ml of the pre-centrifuged protein was gently layered on top of the glycerol (see Figure 3.5).

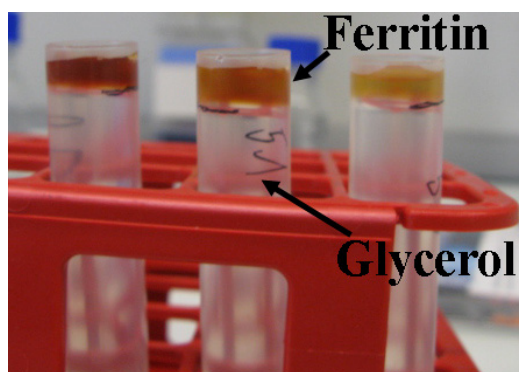


Figure 3.5: ~1ml of the ferritin solution was layered on top of the glycerol in the centrifugation tube.

The samples were centrifuged using a Beckman SW41 swinging bucket rotor (Figure 3.6) in a Beckman ultra centrifuge (Figure 3.6 c) at 30,000-40,000rpm for 2-17h at 20°C. After centrifugation, fractions of 250 μ l each were collected from the top using a Hamilton syringe with the needle tip placed at the desired particle travel distance. The fractions were dialyzed against water in order to stabilize the protein and prevent aggregation. For some experiments the fractions were applied to a second density gradient centrifugation to improve the resolution in size separation. Before loading the sample on the glycerol media, the fraction was concentrated to a volume of ~80 μ l. In case of a second centrifugation run, only the peak fraction was collected from the second run. The ferritin in the dialyzed samples was adsorbed by immersing a chip into the ferritin solution for 1min, followed by rinsing with DI water as described in the previous section. However, since the volume of the solution was only around 250 μ l, it was pipetted onto the chip which was placed in a lid of an Eppendorf tube.

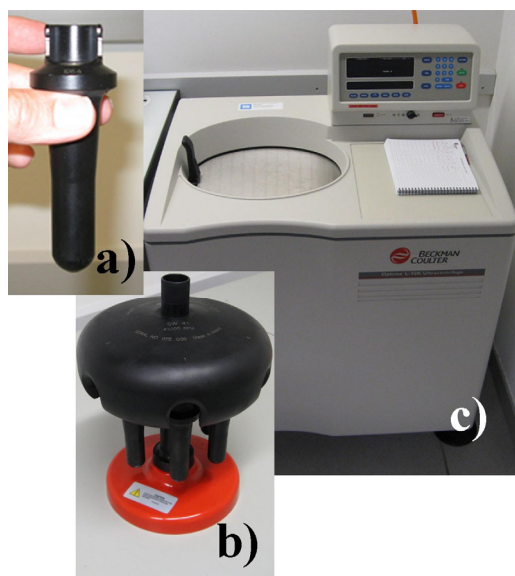


Figure 3.6: Ultra centrifuge equipment: a) centrifuge tube holder, b) centrifugation rotor SW41 and c) Beckman ultra centrifuge.

3.5 SWNT growth

SWNTs were grown in a PEO 603-PLC-300C LPCVD oven (ATV Technology). The CVD machine setup is shown in Figure 3.7. In this particular CVD apparatus, the reaction gas remains in the chamber during the whole reaction time after the injection. This differs from a gas flow chamber, where the gas is steadily flowing through a long quartz tube. Advantage of the stationary system compared to a gas flow system is the better controlled (diffusion controlled) and therefore more reproducible reaction conditions at the catalyst surface.

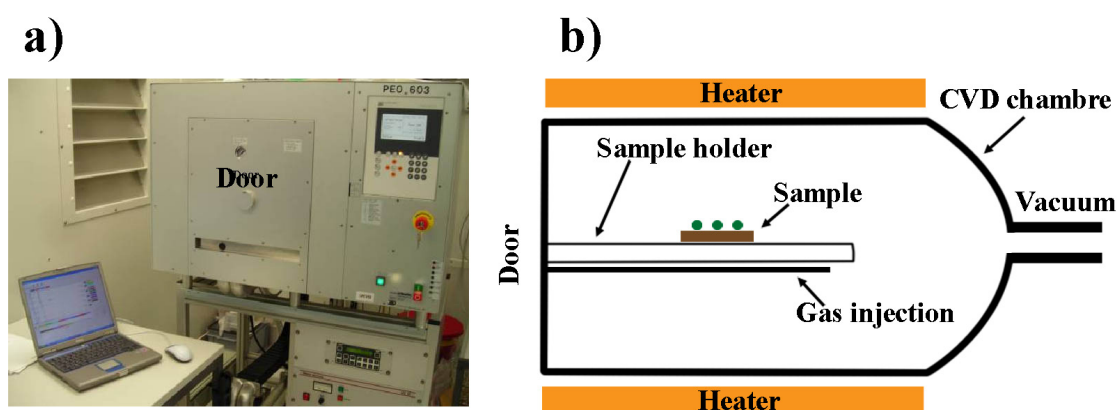


Figure 3.7: CVD apparatus used for the growth of SWNTs. a) Exterior view of the CVD machine. The growth process was controlled and recorded by the corresponding computer program provided for ATV. b) Schematic drawing of the CVD chamber. The sample is placed on a quartz support, while the gas injection takes place beneath the substrate holder. The chamber is heated by radiation heaters arranged around the quartz vacuum chamber.

Table 3.2 shows the steps and the different parameters used for SWNT growth. The row with the standard growth process resulting, in clean large diameter SWNTs, is highlighted in orange. All deviations in the other processes are written bold.

Following the standard procedure is described in detailed. First, the samples were mounted on the quartz holder. The temperature was raised to 850°C and the particles were calcined again for 5min in air to make sure that really all water molecules were removed from the catalysts. Then the chamber was pumped down to vacuum and H₂ was injected into the chamber to a pressure of 375mbar. Under these conditions, the hematite particles were reduced to iron particles⁶ according to:



Then the chamber was pumped to vacuum and 0.2slm H₂ was injected for 45s to achieve a pressure of approximately 55mbar followed by CH₄ injection for 42s with an injection flow of 1slm resulting in an overall pressure of 211mbar. SWNTs were then grown under these

⁶ Only in the ground state iron is catalytically active.

conditions for 15min. Subsequently, the chamber was pumped to vacuum and then cooled to the unloading temperature of approximately 200°C. During the cooling a constant N₂ flow at atmospheric pressure was employed.

Table 3.2: SWNT growth processes. The standard process is highlighted. All variations in the other processes from this process #3 are written in bold.

	Process #1	Process #2	Process #3	Process #4
Step 1	Heating up to 850°C in vacuum and an Ar flow of 0.2slm	Heating up to 850°C in air	Heating up to 850°C in air	Heating up to 850°C in air
Step 2	-	Calcination for 5min	Calcination for 5min	Calcination for 5min
Step 3	Vacuum for 1min to reach a pressure of <10 ⁻⁵ bar	Vacuum for 1min to reach a pressure of <10 ⁻⁵ bar	Vacuum for 1min to reach a pressure of <10 ⁻⁵ bar	Vacuum for 1min to reach a pressure of <10 ⁻⁵ bar
Step 4	Injection of H ₂ to a pressure of 370mbar	Injection of H ₂ to a pressure of 370mbar	Injection of H ₂ to a pressure of 370mbar	Injection of H ₂ to a pressure of 370mbar
Step 5	Particle reduction for 10min	Particle reduction for 10min	Particle reduction for 10min	Particle reduction for 10min
Step 6	Vacuum for 1min to reach a pressure of <10 ⁻⁵ bar	Vacuum for 1min to reach a pressure of <10 ⁻⁵ bar	Vacuum for 1min to reach a pressure of <10 ⁻⁵ bar	Vacuum for 1min to reach a pressure of <10 ⁻⁵ bar
Step 7	Injection of 0.2slm H ₂ for 45s to a pressure of 55mbar	Injection of 0.2slm H ₂ for 43s to a pressure of 48mbar	Injection of 0.2slm H ₂ for 45s to a pressure of 55mbar	Injection of 0.2slm H ₂ for 48s to a pressure of 62mbar
Step 8	Waiting for 1min	Waiting for 1min	Waiting for 1min	Waiting for 1min
Step 9	Injection of 1slm CH ₄ for 42s to an overall pressure of 211 mbar	Injection of 1slm CH ₄ for 42s to an overall pressure of 204 mbar	Injection of 1slm CH ₄ for 42s to an overall pressure of 211 mbar	Injection of 1slm CH ₄ for 42s to an overall pressure of 218 mbar
Step 10	SWNT growth for 15min	SWNT growth for 15min	SWNT growth for 15min	SWNT growth for 15min
Step 11	Vacuum to reach a pressure of <10 ⁻⁵ bar	Vacuum to reach a pressure of <10 ⁻⁵ bar	Vacuum to reach a pressure of <10 ⁻⁵ bar	Vacuum to reach a pressure of <10 ⁻⁵ bar
Step 12	Cooling under N ₂ flow	Cooling under N ₂ flow	Cooling under N ₂ flow	Cooling under N ₂ flow

3.6 SWNT integration by e-beam lithography, metal evaporation and lift-off

SWNTs were grown on the Si/SiO₂ substrate followed by the structuring of Cr/Au metal markers by e-beam lithography, metal evaporation and lift-off. The SWNTs were then mapped by AFM scanning and masks for the contact electrodes were drawn according to the AFM images. After structuring the electrodes into PMMA by e-beam lithography, 2nm Cr and 50nm Au were evaporated followed by lift-off. For a more detailed discussion of this prototype process refer to [6, 29-31].

3.7 Catalyst islands and electrode pad structuring by UV lithography and lift-off

Table 3.3 shows the different UV lithography recipes used for the structuring of markers, catalyst islands and electrodes in the batch CNFET production process. All the used AZ photoresists were delivered by Micro Chemicals GmbH and the ma-N resist was provided by micro resist technology GmbH.

Table 3.3: UV lithography recipes for different resists

Process step	AZ nLOF 2070 2:1 diluted with EBR	AZ 5314E image reversal (as negative resist)	AZ 5314E image reversal (as positive resist)	ma-N 405
Surface pretreatment	Resting of the sample for at least one day in ambient air (45±5% RH, 21 ±1°C) (hydrogenation of Si surface)	Resting of the sample for at least one day in ambient air (45±5% RH, 21 ±1°C) (hydrogenation of Si surface)	Resting of the sample for at least one day in ambient air (45±5% RH, 21 ±1°C) (hydrogenation of Si surface)	Resting of the sample for at least one day in ambient air (45±5% RH, 21 ±1°C) (hydrogenation of Si surface)
Spin coating	@ 5000rpm for 45s	@ 5000rpm for 45s	@ 4000rpm for 45s	@ 5000rpm for 45s
Hardbake	@ 110°C for 1min	@ 105°C for 1min	@ 105°C for 1min	@ 95°C for 1min
UV exposure	Intensity: 11mW/cm ² Time: 2.7s Dose: 29.7mJ/cm ²	Intensity: 7mW/cm ² Time: 1s Dose: 7mJ/cm ²	Intensity: 3mW/cm ² Time: 14s Dose: 42mJ/cm ²	Intensity: 11mW/cm ² Time: 14s Dose: 154mJ/cm ²
Postbake	@ 110°C for 1min	@ 110°C for 2min	-	-
Flood exposure	-	Intensity: 7mW/cm ² Time: 20s Dose: 140mJ/cm ²	-	-
Development	~2min 30s in AZ 826 MIF (convection by pipetting fresh developer onto the substrate by a pipette)	~1min 30s in AZ 826 MIF (convection by pipetting fresh developer onto the substrate by a pipette)	~1min 30s in AZ 826 MIF (convection by pipetting fresh developer onto the substrate by a pipette)	50s in MaD 332 (convection by pipetting fresh developer onto the substrate by a pipette)
DI water rinsing	for >5min	for >5min	for >5min	for >5min
Surface residual removal	in 1% NaOH for 30s (optional)	in 1% NaOH for 15s (optional)	-	in 1% NaOH for 15s (optional)
DI water rinsing	for >5min	for >5min	-	for >5min

3.7.1 Alignment markers

Since this large scale integration process is based on several UV lithography steps, markers are required for the alignment of the mask in the second and third lithography step. Best alignments were achieved with the marker structure shown in Figure 3.8 using a Karl Süss MA6 mask aligner. This Alignment marker structure was not developed in the frame of my theses but is shown here to explain how to achieve best alignments. A coarse alignment was performed with the large structures in the middle, assigned with “1. alignment level”. The fine alignment was then done using the structures assigned with “2. alignment level”. The marker structures were also used for process optimization. The optimal structures for this purpose are assigned in the figure as well.

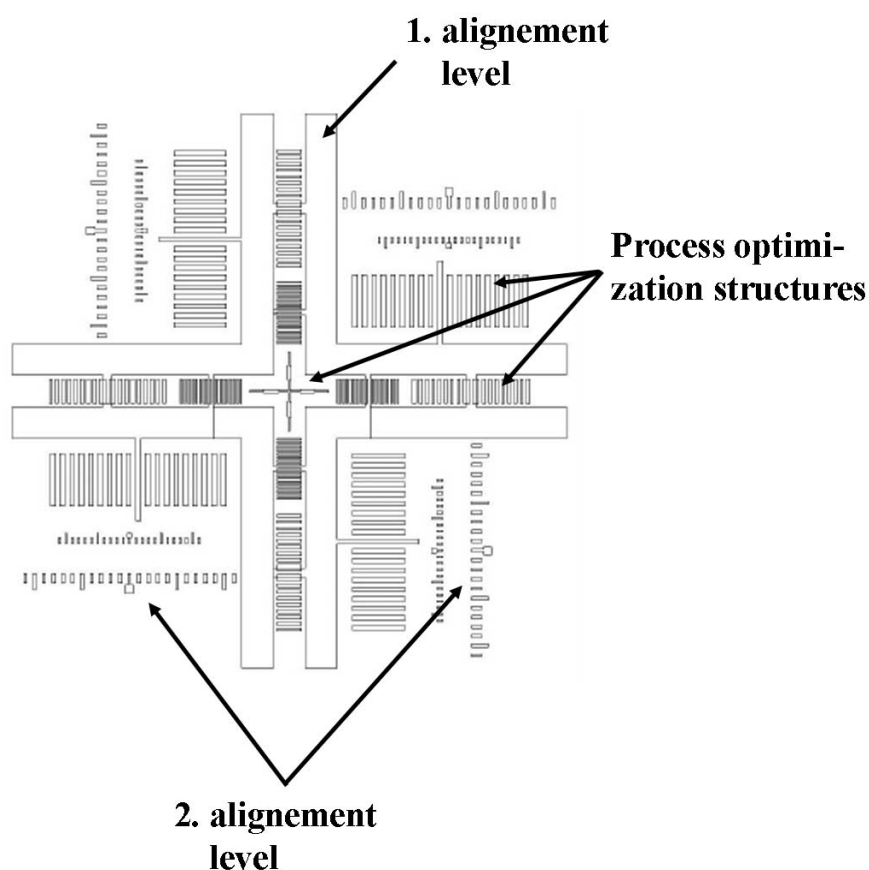


Figure 3.8: Marker for the mask alignment and UV-lithography process development, adapted from [160].

For marker structuring, AZ5314E image reversal resist was used as positive resist. Advantage of this resist compared to other positive resists is that strongly surface binding HMDS (a chemical which is mandatory for the use of most positive resists) can be omitted. HMDS is hard to remove and could influence the SWNT growth. After development, the markers were etched by RIE (Oxford instruments RIE +80) into the 200nm thick SiO₂

layer. In early experiments, the markers were produced using the negative resist AZ nLOF 2070, evaporation of 2nm Cr and 50nm Au and lift-off. However, the use of these metals inhibits SWNT growth drastically. Alternatively, Ti markers were used; however they disappeared during the CVD process due to the etching behavior of H₂. Therefore, the marker structuring process based on etching by RIE was introduced. Since particles on the mask and resist surface cause undesired holes in the resist during the negative UV lithography process, which then results in holes in the gate oxide layer during the RIE etch process, often gate leakage was measured in the final CNFETs. With a positive UV lithography process this problem could be avoided.

3.7.2 Patterning of catalyst islands and growth of SWNTs from these islands

In this process step $2 \times 3 \mu\text{m}^2$ hexagonal holes as shown in Figure 3.9 were structured in the AZ nLOF 2070 negative resist. For a homogenous protein distribution on the SiO₂ surface, all photoresist residuals at the bottom of the structures needed to be removed. This was achieved by dipping the chip into a 1% NaOH solution for 20s after the development of the holes. Alternatively, O₂ plasma ashing was used for residual removal (100W for 30s). However, it could be possible, that O₂ plasma lowers the yield of SWNT growth.

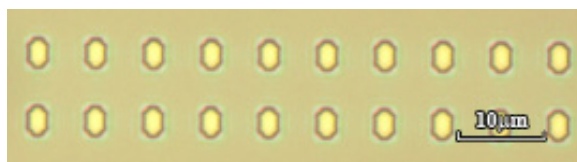


Figure 3.9: Optical microscope image of patterned holes in the photoresist used for ferritin lift-off, resulting in the formation of patterned catalyst islands.

Approximately 80 μl of protein solution was pipetted onto the chip leading to coverage of the whole chip surface. After an adsorption time of 3min, the chip was washed with DI water. Subsequently, the photoresist was stripped by dipping the chip in fresh acetone for approximately 20 seconds. The chip was then transferred to a beaker containing acetone heated to 50°C. After 10min, the chip was put into IPA for 5min. Then it was washed in DI water for 5min. Subsequently, the surface was blown dry by N₂ and the remaining photoresist residuals and the protein shells were removed by heating the chip for 1min on a glass ceramic plate to temperatures >800°C.

SWNTs were grown from the patterned catalyst particles employing the CVD processes described in section 1.5.

3.7.3 Structuring of the electrodes

UV lithography

The structuring of the electrodes is the most critical UV lithography step in this integration process. Remaining photoresist residuals on the SWNTs after development reduces the contact quality and influences therefore the gate sweep characteristics as already discussed in section 1.2.3 . However, O₂ plasma ashing to remove these residuals would damage the SWNTs. On the other hand, applying a NaOH dip to remove the residuals (as it was described in the catalyst patterning process) deteriorates the lift-off profile and therefore the lift-off quality. To overcome this problem the following measures were taken:

1. A photoresist was used which has only weak adhesion to the SiO₂ surface.
2. The negative resist was underexposed.
3. The development time was increased.

Both resists, the AZ5314E used as image reversal resist and the ma-N, resulted in low ohmic contact resistances. However, a better metal lift-off resulted from the AZ5314E resist.

Here the electrode structuring process using this AZ5314E resist is described. It is important to expose the chip to ambient atmosphere for at least one day after CVD growth of SWNTs. Therefore the surface becomes hydrogenated, which causes a weaker adhesion of the resist to the surface. Instead of exposing the structure to UV light at an intensity of 7mW/cm² for 1s, the intensity was reduced to 6mW/cm² while the exposure time was kept unchanged. The reversal bake was then conducted at 110°C, which is the lowest possible reversal bake temperature (the lower the temperature, the weaker is the binding to the SiO₂ surface, the less residuals remain on the surface after development). Prior to the development, the critical development time was adjusted using dummy samples.

A development time of 45s to 60s resulted in the complete removal of the photoresist residuals on the surface, while the structures still remained on the surface. A slightly higher development time resulted in loss of the structures, while with shorter development times residuals were still observed on the surface. In order to verify that all the residuals were removed, the contact area was checked by AFM prior to metallization. The variation of the photolithography process broadened the thickness of the electrodes from originally 4μm to approximately 4.8μm and designed electrode gaps of 2μm were reduced to approximately 0.7μm.

Metallization

50nm Pd or in case of HF post-treatments 2nm Cr + 50nm Pd was evaporated by physical vapor deposition at the “ETH Berufsbildungszentrum für Physiklaboranten”. After evaporation, the chip was put into a home built annealing oven consisting of a gas flow tube with a resistive heater. After the chip was placed on the heater, which was then inserted into the flow tube, the tube was pumped to low pressure (approximately 4mbar). In a next step, the sample was heated to 100°C within 1min and immediately after the

temperature was reached the sample was cooled down to 60°C. This temperature was then kept constant for at least 3h (even better overnight). Omitting the annealing step resulted in the peeling-off of the electrode structures during the lift-off procedure.

Lift-off and cleaning

For lift-off, the chip was placed in heated NMP at a temperature of 60°C for approximately 30min. Subsequently the remaining metal layers were rinsed off the chip in acetone by pipetting acetone onto the chip in the bath. The chip was then put back into the heated NMP.

Since CNFETs are very sensitive to adsorbed molecules on the SWNT surface, it is crucial that no resist remains on it. Therefore, the stripped chip with the contacted SWNTs was kept inside the NMP for 3 days. The temperature was maintained at 60°C. Only this long cleaning time guaranteed the removal of all photoresist residuals from the SWNT. Since the oxygen solubility in NMP is low, the SWNT-metal contacts are protected from oxidation during that time. Then the chip was put into acetone for 5min followed by an isopropanol dip for another 5min. Subsequently the chip was blow-dried with N₂ on a clean room towel. It is important not to put the chip into DI water, because this causes the release of the Pd from the surface and therefore the loss of the electrode structures.

3.7.4 Post-treatments

Annealing

An annealing step improves the contact resistances and it desorbs molecules from the SWNT surfaces. The chip was therefore put into the CVD chamber. The chamber was pumped down to vacuum ($\sim 10^{-5}$ mbar) and subsequently heated to 400°C. This temperature was kept constant for at least 2h. Afterwards the temperature was lowered to 200°C and the sample was removed. (Remark: The unloading of the sample at 200°C might have caused oxidation of the SWNT-Pd interface. Therefore I would cool the oven down to room temperature before unloading or even better anneal the samples directly in the ALD machine.)

In some cases, measurements of unpassivated CNFETs were performed. Those samples were annealed in the home built annealing oven (see above) under vacuum (~ 4 mbar) at an annealing temperature of 400°C for more than 2h.

Al₂O₃ passivation by atomic layer deposition (ALD)

Directly after the annealing, the devices were transferred to the ALD oven (Picosun Sunale R-150B). The transfer time was approximately 5min. The samples were covered with 50nm Al₂O₃ according to reference [29]. With this layer, the devices were protected from molecule adsorption and therefore became long term stable.

Production of suspended SWNTs

The process for producing suspended SWNTs was adapted from reference [85]. For better adhesion of the Pd electrodes to the wafer, 2nm Cr was evaporated prior to Pd evaporation.

After the annealing step, the samples were dipped for 3min in ~0.5% HF solution followed by transferring the chips to a beaker with DI water. After cleaning the chips in a second DI water beaker, they were put into a beaker with isopropanol and finally dried in a critical point dryer (Automegasamdri®-915B, Tousimis Research Corporation).

3.8 Analysis

3.8.1 AFM

The nanoparticle size and SWNT diameter determination was performed by AFM height measurements (Digital Instruments-Veeco Metrology Group, Dimension 3100), assuming a spherical shape in the case of the nanoparticle size determination and assuming cylindrical shape of the SWNT (i.e. neglecting deformations from SWNT-surface interactions and assuming low deformation induced by tip-SWNT forces). All images were recorded in the repulsive AFM tapping mode. For measurements on the SiO₂ surfaces, an error in the height of 0.15nm was determined based on multiple measurements and on system specifications. The particle analysis was performed with the grain analysis tool (SPIP, Image Metrology) using the measured heights of 250-1000 particles per sample. To determine the diameter of a SWNT, the height of the tube was measured at 4 different positions along the SWNT. To obtain reliable height values, the heights were measured only from individual tubes at positions where the SWNT was lying flat on the substrates, far from crossing points with other tubes.

3.8.2 SEM and TEM

A field emission scanning electron microscope (Zeiss, ULTRA 55) with inlens-detector was used for capturing of SEM images. Commonly the working distance was around 3mm and the acceleration voltage was set to 3kV.

Transmission electron microscopy (TEM) images were recorded by a FEI CM12 TEM at acceleration voltages of 80kV to 100kV [161].

Some of the SEM and all TEM analysis were performed on suspended SWNTs which were grown on micro machined samples. An SEM image of a micro machined polysilicon hole with a bridging SWNT is shown in Figure 3.10. The micro machined chips were produced in a polysilicon-based foundry process described elsewhere [115-116, 162]. These polysilicon chips were first oxidized in an oxidation oven (ATV) at 1000°C for 5h constant oxygen flow or on a hot plate (T >800°C) for approximately 10min in air under and then

dipped for 1min into a prepared ferritin solution. SWNTs were grown with process #4 of Table 3.2.

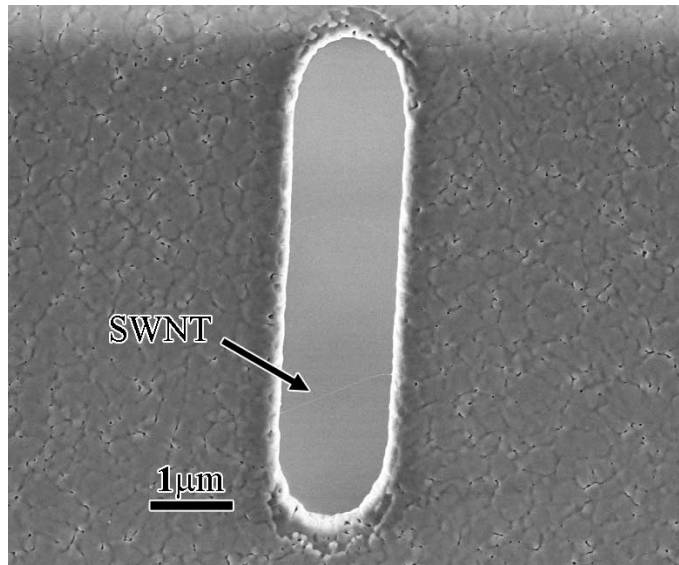


Figure 3.10: SEM image of a micro machined poly-MEMs structure. SWNTs were grown from Ferritin particles on the oxidized surface. For TEM analysis SWNTs were grown from tip structures (see therefore [161]).

3.8.3 Raman spectroscopy

Raman spectra of suspended SWNTs were recorded at room temperature by a scanning confocal Raman microscope (WITec CRM 200) with a 532nm laser (2.33eV) [163]. The analysis was performed either on a sample with a high SWNT density or on suspended SWNTs.

3.8.4 Transistor measurements

The CNFET measurement setup is shown in Figure 3.11. The Pd contacts were used as source and drain electrodes and the thermally grown 200nm thick silicon oxide layer acts as gate oxide. The highly p-doped Si substrate was used as gate electrode a). The electrodes on the devices were contacted via probe needles on a probe station and the gate electrode was contacted via the chuck b).

The source-drain voltage was kept constant at 20mV or 30mV by a Keithly 2400 SourceMeter (Keithly Instruments). The drain current was amplified by a FEMTO DLPCA-200 variable gain low-noise current amplifier. After I-V conversion, the voltage was measured by a Keithly 2000 digital multimeter (Keithly Instruments). The whole measurements were controlled by a LabVIEW program.

The gate voltage was varied from 0V to 10V, to -10V and back to 0V. In more sophisticated measurements, potential pulses were applied as shown in Figure 3.12. The use of pulsed gate sweep measurements was introduced elsewhere [28-29, 164] and has the effect of reducing the hysteresis. Large hysteresis in the gate sweep is explained by charge trapping due to polar molecules around the SWNT or by charge injection from the SWNT into the substrate [165]. Here, immediately after a positive potential pulse, a negative potential pulse with the same amplitude was applied. Therefore, these charging effects can be balanced [166] and hence hysteresis effects are suppressed. Figure 3.12 a) shows the overall pulse characteristics. The gate potential pulses were increased to $\pm 10\text{V}$ and then decreased again to 0V. This pulse characteristic was applied twice. As shown in Figure 3.12 b), pulses of 1ms were applied with increasing gate voltage steps of $\pm 0.4\text{V}$, where first the positive voltage pulse was applied followed by the negative voltage pulse with the same absolute value.

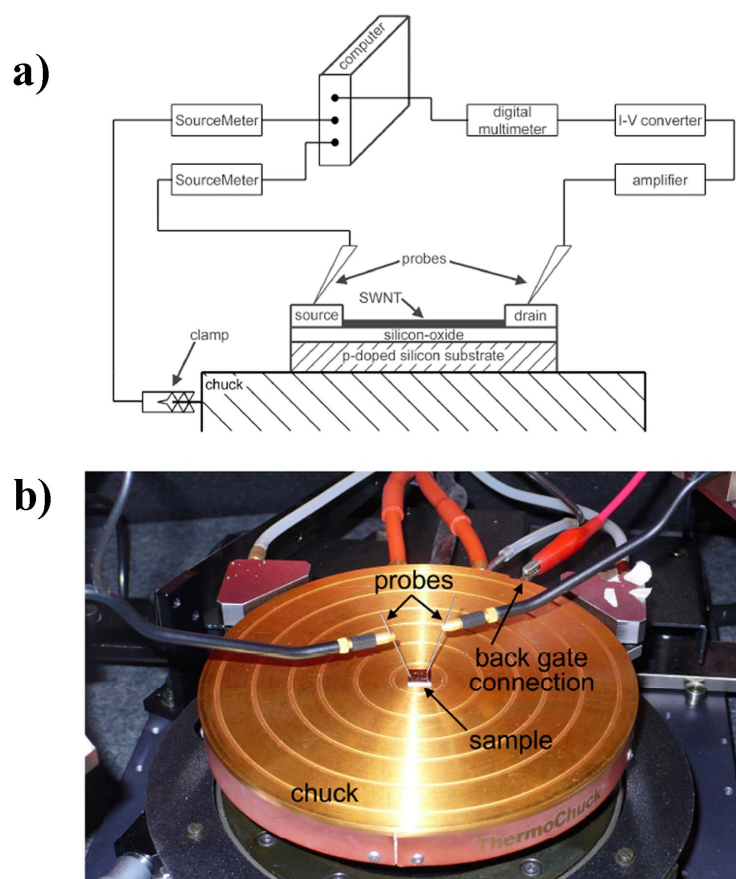


Figure 3.11: CNFET measurement setup, source and drain electrodes were contacted by probe needles on a probe station, while the back gate was contacted over the chuck. Adapted from [160]

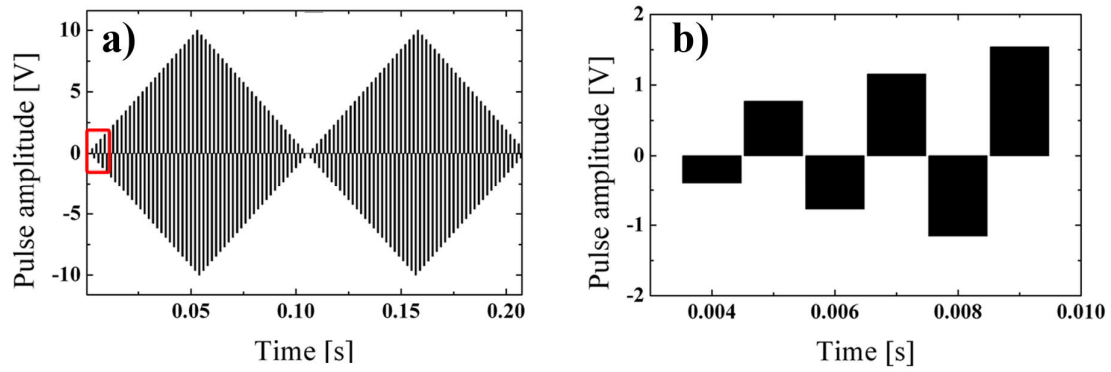


Figure 3.12: Applied pulse sequence for pulsed gate sweep measurements resulting in current responses with reduced hysteresis effects. a) The overall view shows that the potential is shifted from 0V to ± 10 V and back to 0V. b) Shows a detailed view of the sector indicated by the rectangle in a).

4 Results and discussions

This Chapter is divided in three main sections. First the investigations on SWNT growth from ferritin based catalysts are reported. In the second section, it is shown how the SWNT diameter can be controlled and the diameter distribution narrowed. In the last section, the development of a batch compatible large scale integration process is shown. Investigations of CNFETs from this process show interesting results towards device reproducibility.

4.1 Growth of straight, clean and individual SWNTs

In this section, investigations on the SWNT synthesis process on SiO₂ surfaces (from ferritin proteins to SWNTs) are shown. The SWNTs were characterized by AFM, TEM and Raman. Special features which might give some indications on the growth and bundle formation process are discussed. In the second part, the investigations resulting in the SWNT surface density control and in the growth of only individual SWNTs are shown. The data of this chapter were published in the journal “Sensors and Actuators” [96].

4.1.1 SWNTs grown from ferritin based catalyst nanoparticles

Figure 4.1 a) shows an AFM image of a SiO₂ surface with commercially available saturated ferritin (Fluka) adsorbed from a 50 times diluted ferritin solution. The stock solution contained 50-150mg/ml ferritin. The mean height of the iron loaded proteins is 3.5 ± 1.4 nm and the surface coverage is $70 \text{ proteins}/\mu\text{m}^2$. Figure 4.1 b) and c) show AFM images of the resulting Fe₂O₃ nanoparticles and of SWNTs grown from the ferritin-based Fe catalysts. In Figure 4.1 d) and e), diameter distribution histograms of the formed particles and grown SWNTs are shown. The CVD process yielded SWNTs with lengths between 100nm and 40 μ m. The mean length was 2 μ m. The mean value and standard deviation of the SWNT yield was obtained considering 7 AFM images and are 0.24 ± 0.21 SWNT/particle. For this result, the particles and SWNTs grown on particles in the images were counted. In the image of In Figure 4.1 c), both thick straight SWNTs and small curved SWNTs can be identified. The straight SWNTs have mainly diameters >0.9 nm while for curvy SWNTs diameters <0.9 nm were measured. Depending on the sample received from Fluka, up to 30% of the grown SWNTs had these undesired small diameters.

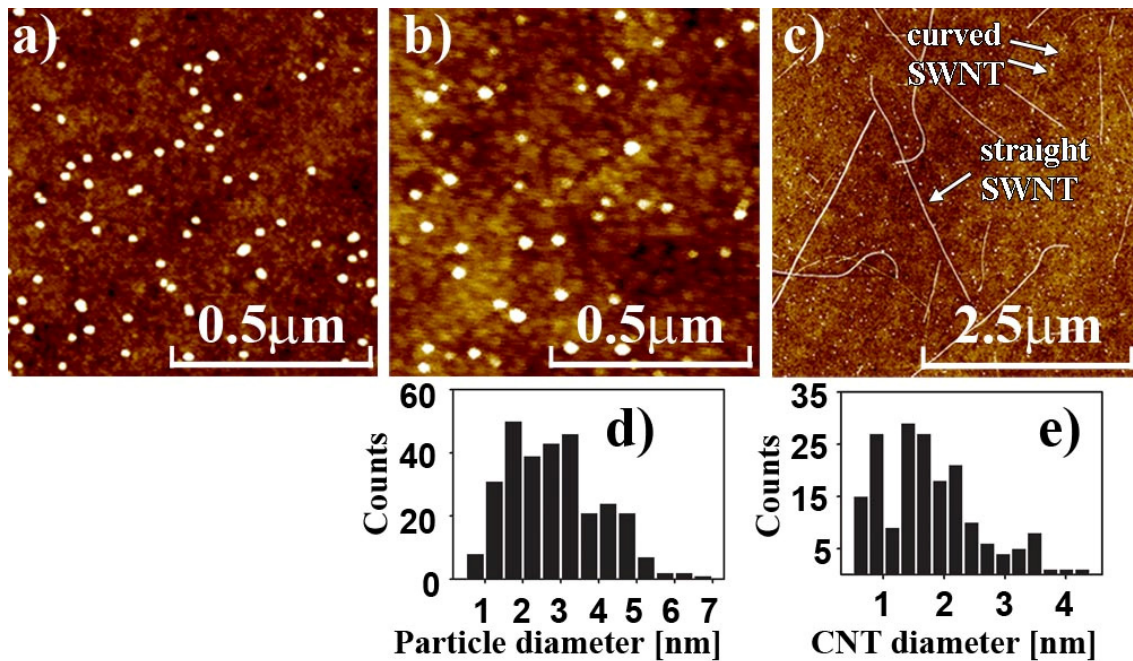


Figure 4.1: AFM image of a) ferritin proteins (Fluka) adsorbed on a SiO_2 surface, color range: 10nm b) Fe_2O_3 nanoparticles formed by oxidation of the adsorbed ferritin shells and subsequent calcination of the ferrihydrite nanoparticles, color range: 5nm, c) SWNTs grown from the reduced Fe_2O_3 particles by the standard CVD process, color range: 5nm d) diameter distribution of the Fe_2O_3 particles, e) diameter distribution histogram of the grown SWNTs, adapted from [96].

TEM and Raman spectroscopy are powerful analysis tools to determine whether SWNTs, MWNTs were grown and to obtain information about amorphous carbon formation or other contaminations. The size of the D band peak in relation to the G band peak in a Raman spectrum indicates additionally if the tube has defects in its structure. A large D peak refers to increased defect density in the structure [167].

The TEM image of Figure 4.2 a) shows a straight SWNT grown from a ferritin-based catalyst particle (Fluka) by the CVD process #4 on an micro machined and oxidized poly silicon surface (see chapter 3.8.2.). The SWNT is mainly clean. So far more than 50 SWNTs were analyzed by TEM on the $\text{SiO}_2/\text{polySi}$ substrates and exclusively tubes consisting of one wall were obtained (see also an individual and a bundle consisting of 6 SWNTs shown in Figure 1.7. which were grown on the same substrate with the same process).

A typical Raman spectrum for SWNTs is shown in Figure 4.2 b). The spectrum was recorded on a sample with SWNTs grown on Fe particles by process #1, yielded from ferritin proteins delivered by Fluka. The radial breathing mode (RBM) has a shift of 161cm^{-1} , from which a SWNT diameter of 1.5nm can be determined [163]. No D band peak at approximately $\sim 1350\text{cm}^{-1}$ was detected, which is an indication, that the SWNT has a very low defect density. [24]. Overall, more than 50 SWNTs produced by processes #1, #3 and #4 were analyzed by Raman spectroscopy, all showing only small or even no D band peaks.

For example all SWNTs mapped by the scanning Raman (G-band filter) shown in Figure 4.3 have all very high G/D peak ratios or the D band peak is fully missing as the one shown in Figure 4.2 b). The reason for this low amount of SWNT detection on a surface with a high SWNT density is that the Raman signal of CVD grown SWNTs in contact with the SiO₂ substrate is suppressed. Therefore, only free standing (when one SWNT lies on other SWNTs) can be detected.

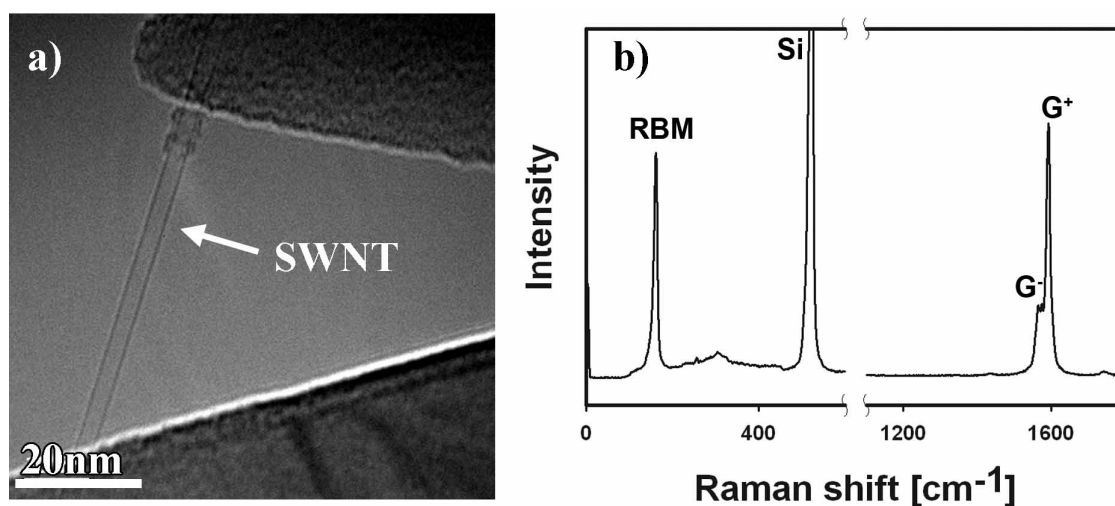


Figure 4.2: a) TEM image and b) Raman spectrum of amorphous carbon-free SWNTs grown by the CVD process #4 and #1, respectively from ferritin-based Fe catalyst nanoparticles (from Fluka).

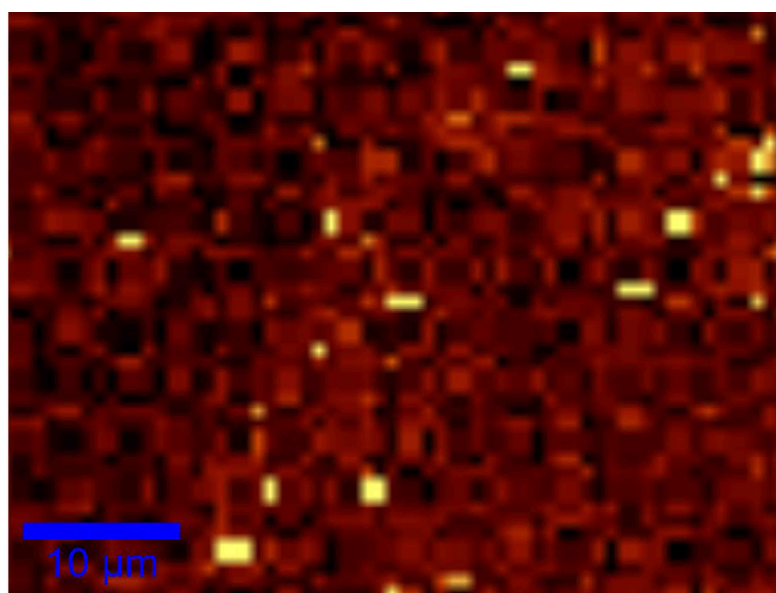


Figure 4.3: Scanning Raman image of a SiO₂ surface with a high density of SWNTs grown by process #1 from ferritin-based catalysts (Fluka). The bright spot are showing the G-band of SWNTs on the surface. The G/D ratios of all these 21 SWNTs are in the same range as the one in the example spectra from Figure 4.2 b).

Independent on the CVD process (#1-#4) some features were constantly observed. These features give indications on the growth process of SWNTs. The most common features are assigned in the AFM image shown in Figure 4.4. For better visualization, the same surface area is shown in top (left side) and 3D (right side) view. Positions 1 and 5 indicate the catalyst particle, which had catalyzed the growth of the attached SWNTs. Interestingly, the particle is larger than the SWNT diameter. This effect has often been observed using the growth of SWNTs from ferritin-based catalysts on SiO₂ surfaces. Grown SWNTs with diameters >0.9nm often show a bend or a kink near the particle side, assigned with 2 and 3, respectively. At position 4, a small diameter SWNT joins a SWNT with a larger diameter. Therefore, this position shows the formation of a SWNT bundle. It can be assumed that from position 1 (SWNT end with the catalyst particle at the lower part of the image) to position 4 the thicker SWNT is individual, while henceforward a bundle consisting of the two SWNTs occurs.

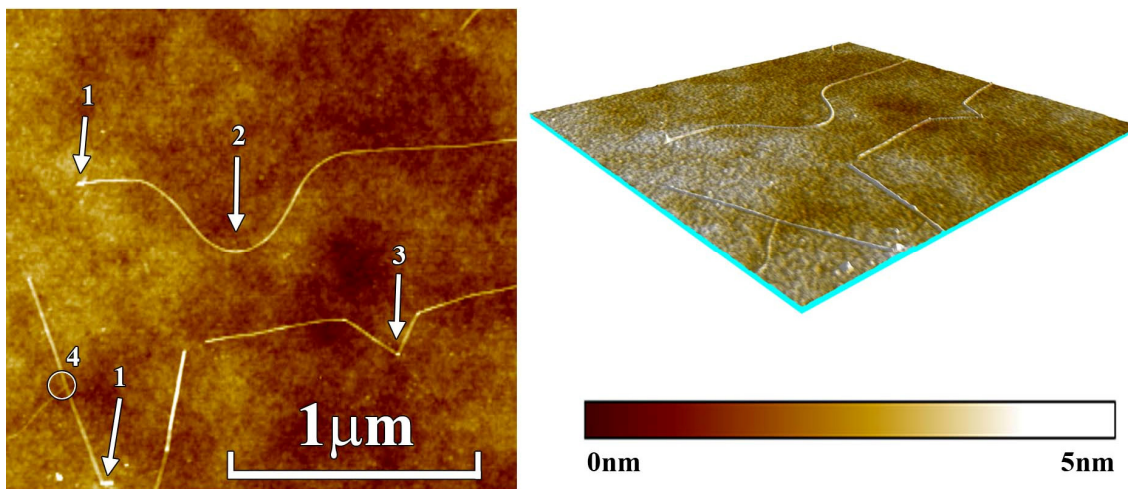


Figure 4.4: AFM image top and 3D view of SWNTs grown from ferritin-based catalyst nanoparticles (Fluka) by the CVD process #3. In the top view, special features which were often observed from SWNTs grown by this process are assigned. **1:** Large particle at the catalyst end of the SWNT, **2:** Bend near the catalyst end, **3:** Kink near the catalyst end **4:** Bundle formation event.

To determine whether the main growth mechanism is tip- or base- growth, SWNTs were grown from patterned growth islands shown in Figure 4.5 (see process preparation in chapter 3.7.2). To visualize the patterns on the SiO₂ surface the developed photoresist covered chip was dipped for 3s into a 0.05% HF solution resulting in approximately 0.7nm deep etch holes. After ferritin adsorption into these holes, lift-off and CVD growth by process #3, the SWNTs were analyzed by AFM. The catalyst end of the SWNTs can be determined by the particle at one SWNT end as discussed above. An SWNT which has its catalyst end inside the etched region and the other end in a surface region which was covered with photoresist during ferritin adsorption (not etched region) was grown by the

base growth mechanism. 7 SWNTs in Figure 4.5 (assigned by a cycle around the starting point) can therefore be assigned as base grown tubes, while the growth process of the other 11 SWNTs cannot be assigned because they have both ends in the HF etched part.

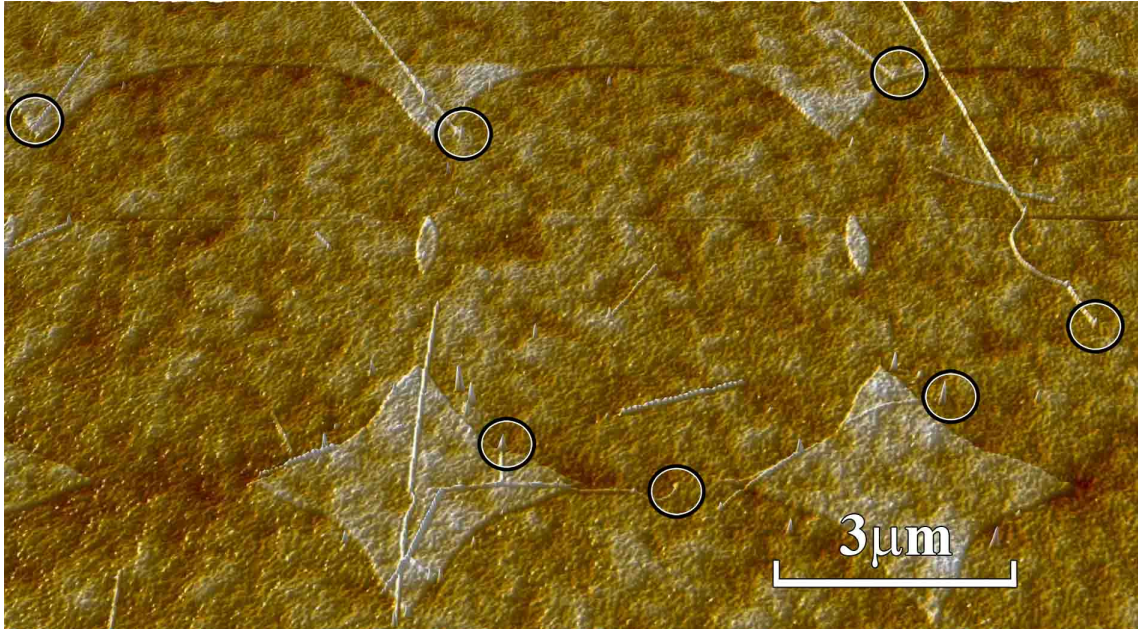


Figure 4.5: 3D AFM image of SWNTs grown from ferritin-based catalyst nanoparticles at UV lithographically structured growth islands. For visualizing the growth islands, the SiO₂ surface in the patterned structures was slightly etched by a 0.05% HF solutions for 3s prior to catalyst adsorption (Since the UV exposing was not optimal in this particular process run, the growth islands are connected). The circles highlight SWNT growth starting points with one end on the surface areas which had been covered by photoresist during ferritin adsorption.

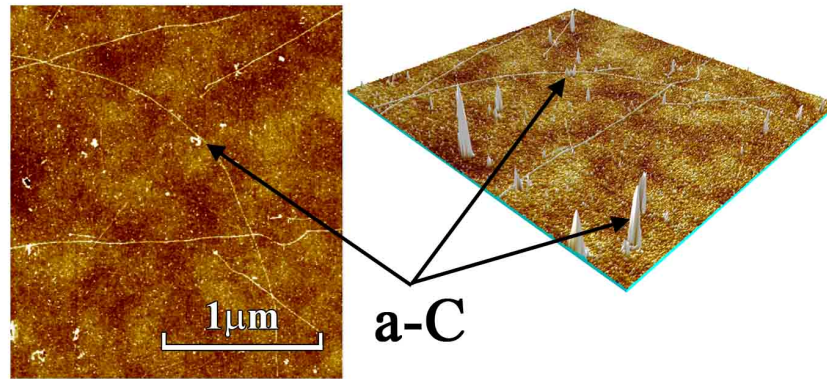
As mentioned in the new qualitative growth model described in the appendix and also shown by Lu et al. [98], the nucleation of SWNTs with larger diameters, which are required for low resistance contacts, might increase with increasing velocity of the formation of free carbon on the catalyst. This can for example be achieved by a reduction of the H₂ partial pressure or an increase in the CH₄ partial pressure as described in Equation (6.10). However, unwanted amorphous carbon formation does increase too (Equation 6.13). Therefore the growth of SWNTs with optimal parameters (highest possible formation of free carbon on the catalyst with lowest possible amorphous carbon formation in the CVD chamber) is crucial.

Figure 4.6 shows two AFM images in top and 3D view of SWNTs grown by two different growth processes. The SWNTs shown in a) are grown with processes #2 using a lower hydrogen content (48mbar) than used for the growth of the SWNTs shown in b), which were grown by process #4 (64mbar). Beside the SWNTs image a) shows a lot of particles which have heights up to 40nm. Since the catalyst nanoparticle density prior to SWNT growth was much smaller ($\sim 1\text{particle}/\mu\text{m}^2$), these new particles can be related to amorphous

carbon deposited by pyrolysis of methane in the gas phase. On the other hand, the surface treated by the CVD growth process #4 shown in Figure 4.6 b) is free of amorphous carbon. The catalyst density was ~ 0.5 particles/ μm^2 . However, already at an H_2 partial pressure of 55mbar (process #3) no amorphous carbon was obtained on the surface (cf. Figure 4.4).

a)

CVD pressures
 $\text{H}_2/\text{CH}_4 =$
 48mbar/156mbar



b)

CVD pressures
 $\text{H}_2/\text{CH}_4 =$
 62mbar/156mbar

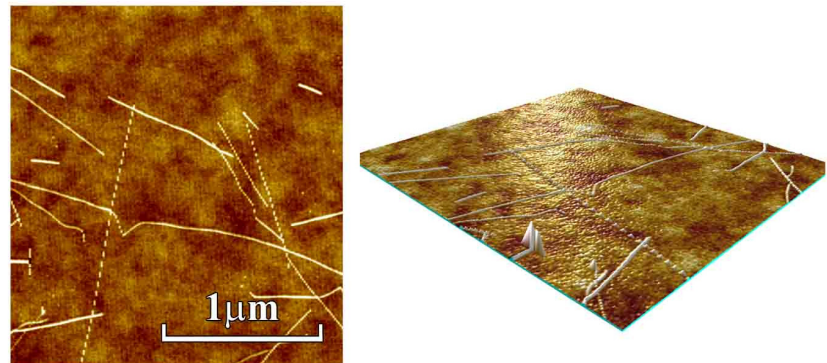


Figure 4.6: SWNTs grown from ferritin-based catalyst nanoparticles (Fluka) by two different CVD processes. In process #4 (b) a higher partial pressure of H_2 than in process #2 (a) was applied, which enabled avoiding amorphous carbon formation. (The dotted recorded lines in the image originates from reduced recording resolution in one scan direction)

The contact quality of CNFETs produced with the SWNTs grown by process #2 degraded over time, even when they were passivated by ALD Al_2O_3 . Figure 4.7 shows a CNFET gate sweep measurement of a s-SWNT which had been grown by process #2. The on-state current decreases over time while the noise level increases drastically.

SWNTs produced by process #1, #3 and #4 show long term stability upon Al_2O_3 passivation as described in reference [29].

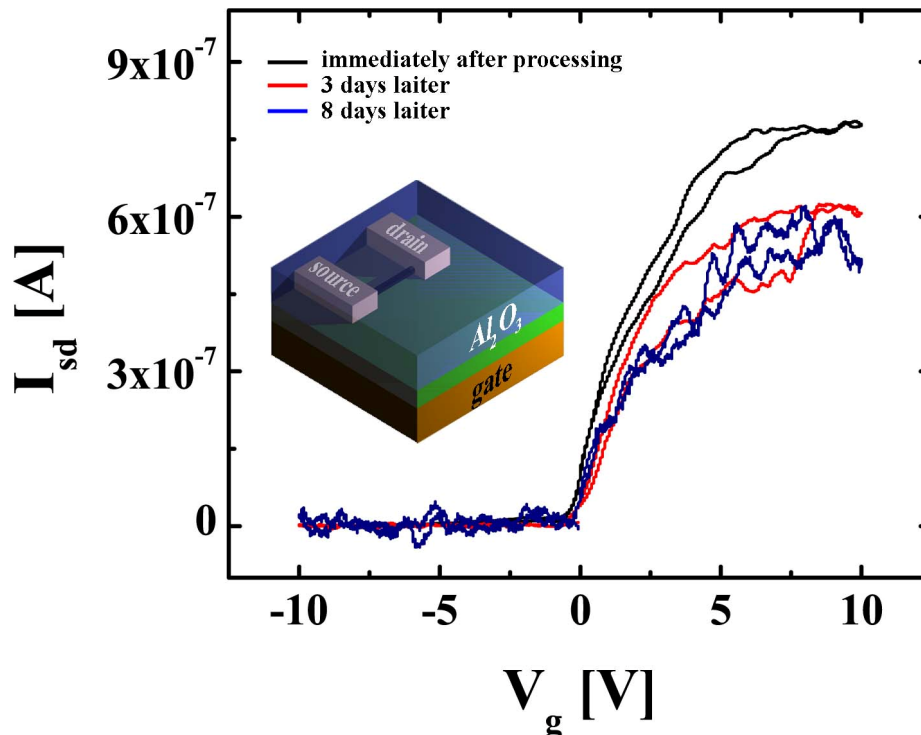


Figure 4.7: Gate sweep measurements of a CNFET consisting of an SWNT which was grown by process #2 recorded immediately, three days and eight days after passivation with ALD Al_2O_3 . V_{sd} was set to 60mV.

4.1.2 Control of the SWNT density

As already mentioned in the introduction (chapter 1.3.5), for SWNT integration it is important to have control over the SWNT density on the surface. In the case of ferritin-based catalysts, the SWNT density is proportionally dependent on the ferritin density on the surface. Li et al. [71] used for their adsorption process an adsorption time of 24h, which suggests, that with this long adsorption time a higher SWNT density can be obtained.

Figure 4.8 a) shows the ferritin density of adsorbed ferritin on SiO_2 in dependence of the adsorption time. In this experiment four chips were simultaneously put in the 89-times diluted ferritin solution (Fluka). After 1, 20, 60 and 180min, respectively, a chip was taken out of the solution and into DI-water for 1min. The density was then obtained by AFM tapping mode imaging of a randomly chosen $5 \times 5 \mu\text{m}^2$ spot. No significant changes in the ferritin density due to an increased adsorption time were observed. Figure 4.8 b) shows the density of adsorbed ferritin on a SiO_2 surface in dependence of the dilution of the ferritin stock solution. Because the ferritin concentration in the stock solution (50-150 mg/ml) is only approximately known, it is not possible to assign the ferritin concentration quantitatively. This means that for a freshly prepared ferritin solution the initial ferritin density has to be verified. However, the diagram shows that the ferritin density on the surface decreases with increasing dilution.

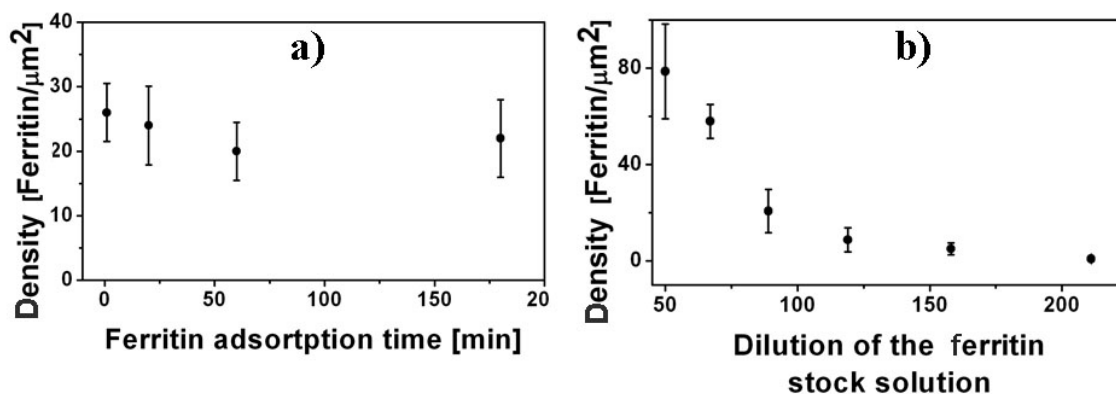


Figure 4.8: Ferritin density on the SiO₂ surfaces measured by AFM imaging in dependence of a) the ferritin adsorption time and b) the dilution of the ferritin stock solution. The stock solution consists of commercially available saturated ferritin, adapted from [96]

That the SWNT surface density indeed can be controlled by the dilution of the ferritin solution is shown in the diagram in Figure 4.9, where the SWNT surface density is plotted vs. the dilution of the ferritin stock solution. The analyzed SWNTs were grown from ferritin-based Fe catalyst nanoparticles gained from 45min loaded ferritin (loading process #2). For each data point, tubes from at least three $15 \times 15 \mu\text{m}^2$ AFM images recorded at three different spots on the same sample were counted. Similar to the decrease of the ferritin surface density by increasing the dilution of the ferritin solution, the SWNT surface density decreases with increasing dilution of the ferritin solution. AFM images show the corresponding SWNT density for dilutions of 300 (b) and 1000 (c) times. The enlarged detail in b) at the upper image shows that at this high density the SWNTs often appear in bundles, indicated by the encircled branches. For very low SWNT site densities as shown in c), no such junctions were observed.

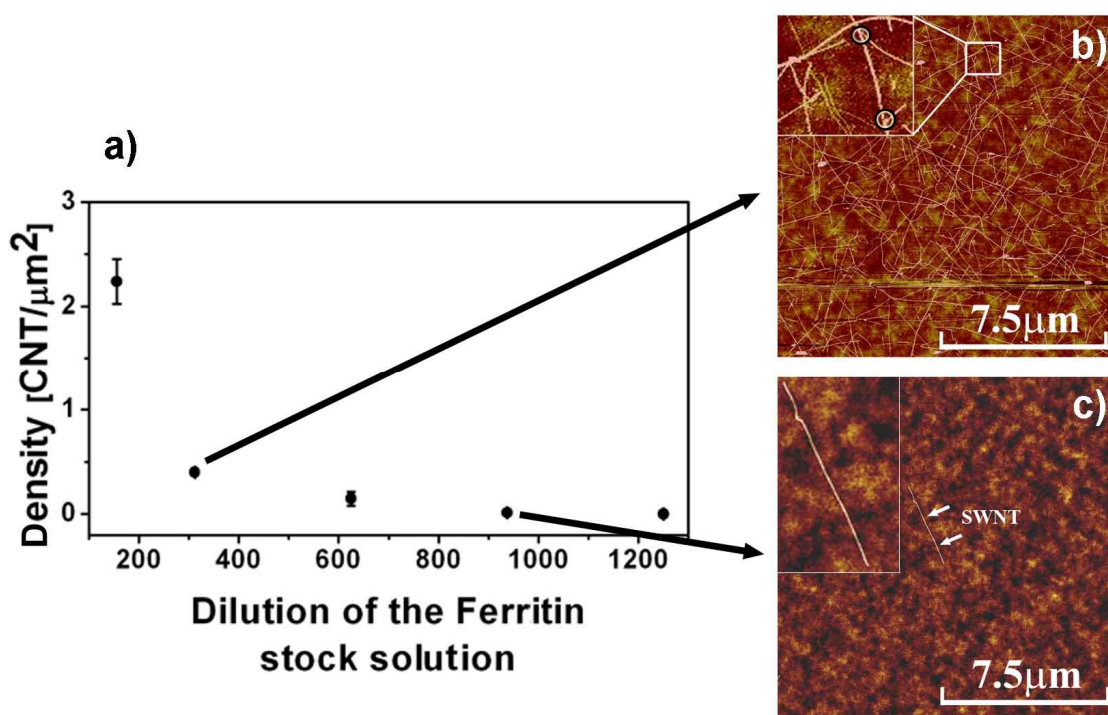


Figure 4.9: a) SWNT density on SiO_2 measured by AFM in dependence of the dilution of the ferritin stock solution. The stock solution contained ferritin prepared by process #2. b) AFM image for a stock solution diluted 300 times. The inset indicates the formation of bundles at higher SWNT densities. c) AFM image for a stock solution diluted 1000 times. A detailed view shows that the formation of bundles can be avoided by reducing the SWNT density, color range: 5nm, adapted from [96].

4.1.3 CNFETs-based on SWNTs grown from ferritin-based catalyst nanoparticles

Figure 4.10 shows an AFM map of SWNTs recorded in an area containing e-beam marker for SWNT localization and electrode mask design. The SWNTs were grown previous marker structuring by CVD process #3 from ferritin-based catalysts (Fluka). This low SWNT density of approximately 8-14 SWNTs/ $100\mu\text{m}^2$ is important for SWNT integration by e-beam lithography to avoid device shorting by other SWNTs. These densities were achieved by making a dilution row from a ferritin stock solution and subsequent determination of the particle density on the surface. Using the solution for sample preparation which shows a particle density of ~ 0.01 - 0.05 particles/ μm^2 resulted in the desired SWNT density.

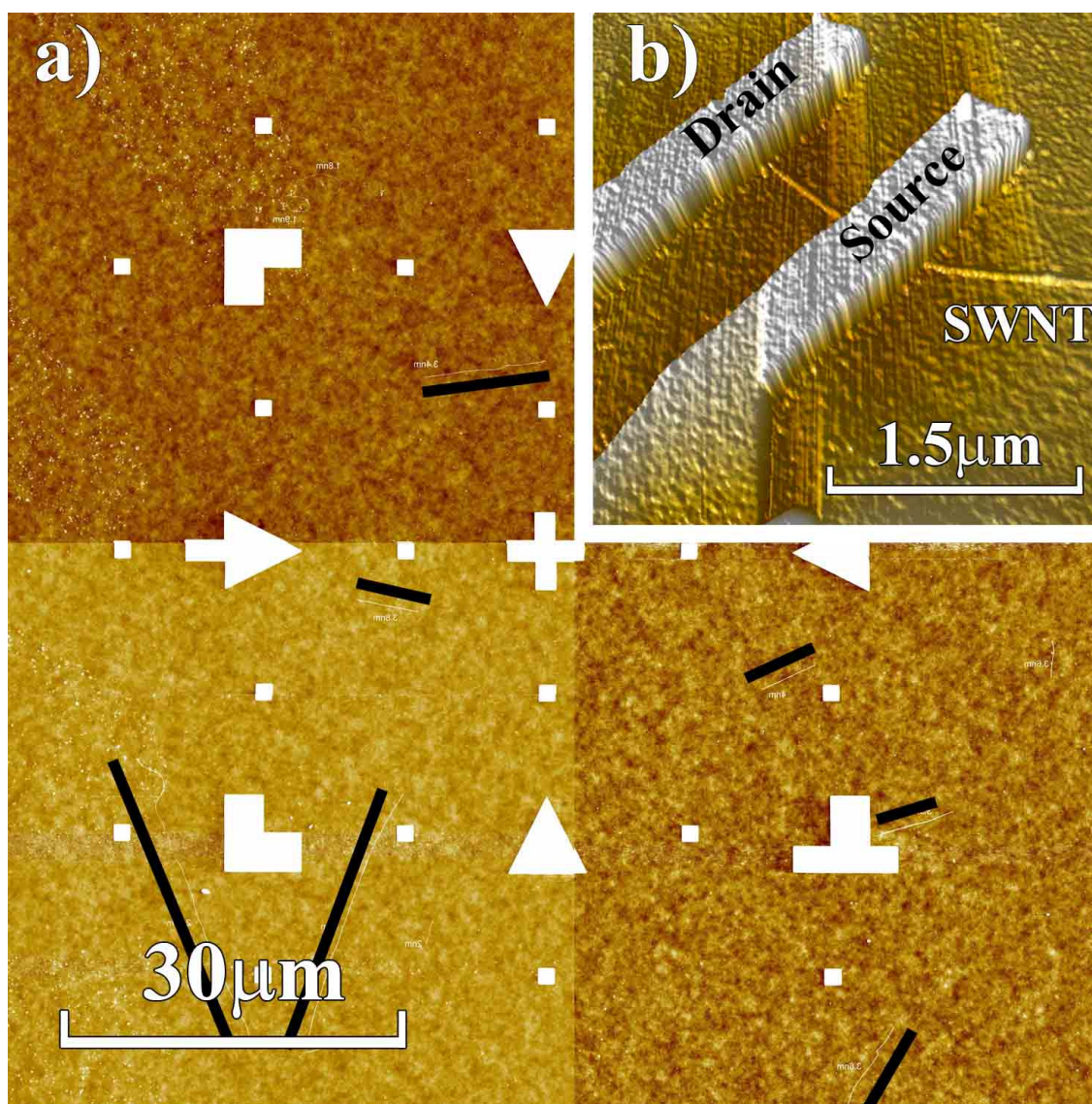


Figure 4.10: a) Large area AFM map for localizing the SWNTs grown from ferritin-based catalysts (#3) in the e-beam marker area for SWNT integration by e-beam lithography metal evaporation and lift-off. The SWNTs are marked by black lines. Such a low SWNT density is required to avoid device shorting by other SWNTs and was achieved by diluting the ferritin stock solution prior to adsorption, color range: 5nm. b) 3D-AFM image of a SWNT contacted by Cr/Au electrodes structured by e-beam lithography and lift-off, color range: 30 nm.

Figure 4.11 shows typical gate sweep measurements (back gate) of a non-passivated semiconducting SWNT and small band gap semiconducting SWNT, respectively. The hysteresis in both curves are related to gating effects, induced by polar molecules adsorbed on the SWNT or nearby the SiO₂ surface [165].

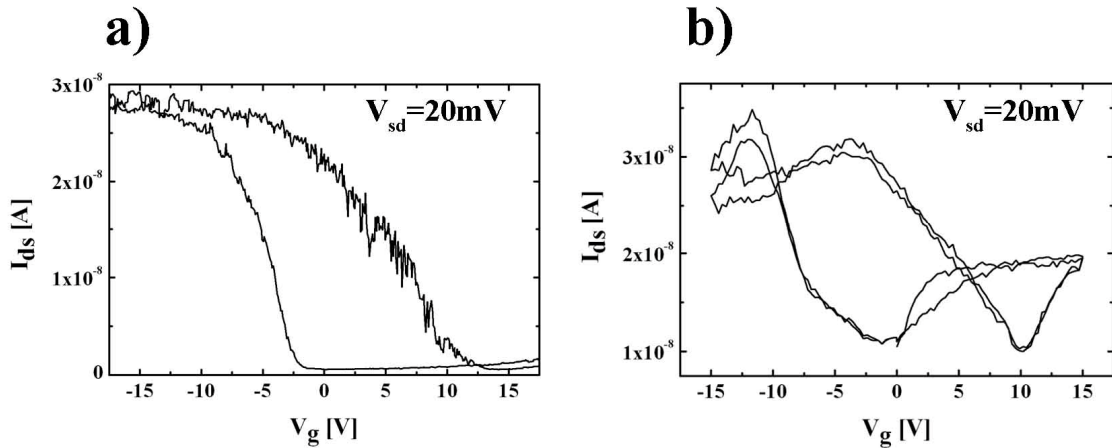


Figure 4.11: Gate sweep measurements of a non-passivated individual a) s-SWNTs and b) SGS-SWNT in CNFET architecture. The large hysteresis effects are due to water and other molecular adsorption on the CNFET surface.

4.1.4 Discussion

Understanding the growth of SWNTs on SiO₂ surfaces from ferritin-based catalysts

As shown in Figure 4.1 SWNTs with larger diameters are straight, while SWNTs with diameter below $\sim 0.9\text{nm}$ often have a curvy shape. To understand why this is the case, the underlying growth process needs to be understood. The features observed in Figure 4.4 and Figure 4.5 give some hints on that process.

Tip or base growth

From the experiment shown in Figure 4.5 and from the TEM images of SWNTs grown from ferritin-based catalyst nanoparticles on polycrystalline SiO₂ substrates by Li et al. [71] shown in the introduction part (Figure 1.6) it can be concluded that the SWNT growth process is mainly a “base growth process”. This means that the catalyst particle remains attached on the SiO₂ surface.

Determination of the growth process for straight SWNTs

SWNTs with diameters $> 0.9\text{nm}$ show often a kink or bend at the catalyst particle side of the SWNT. These features can only be caused by a compressive stress. In two growth scenarios the occurrence of such compressive forces can be imagined:

- The SWNT grows straight upwards. After reaching a certain length the base of the SWNT becomes unstable due to the weight of the SWNT. A bend or kink occurs which causes the SWNT to stick to the surface.
- The SWNT fall first to the ground where it sticks due to Van-der-Waals interactions between the SWNT and the surface. However, the SWNT growth continues resulting in a lateral force. While the SWNT remain attached due to Van-der-Waals interactions this growth force causes the characteristic bend or kink.

In situ growth investigations have shown that SWNTs move a lot during growth and stick then to the surface [168]. During these movements the catalyst particle are like a ball and socket joint, while the SWNT remains stiff. Therefore, the second scenario is more presumable.

Subsequently after this kink or bend is formed the growth might terminate. But the catalysis of carbon atoms at the nanoparticle surface is still ongoing, leading to an increase of ΔG for the formation of carbon on the catalyst surface. Hence the nucleation of amorphous carbon is enabled (see appendix). This would explain the observation that particles attached to the SWNTs base are often larger in size than the tubes are in diameter (cf. points 1 in Figure 4.6). The additional material originates from amorphous carbon formed on the catalyst after the termination of the SWNT growth.

From these considerations the growth process shown in Figure 4.12 can be concluded:

1. After nucleation the SWNT grows straight upwards.
2. At a certain stage, the SWNT fall to the SiO_2 surface.
3. Van-der-Waals forces between the SWNT and the SiO_2 surface fix the SWNT to the surface, while the growth is still going on. The growth force on one side and the Van der Waals forces between the SWNT and the surface on the other side, results in a compressive strain causing a bend or a kink at the catalyst side of the tube.
4. Subsequently, the SWNT growth terminates, which results in a steadily increasing carbon concentration on the catalyst surface causing the nucleation of amorphous carbon on the catalyst particle.

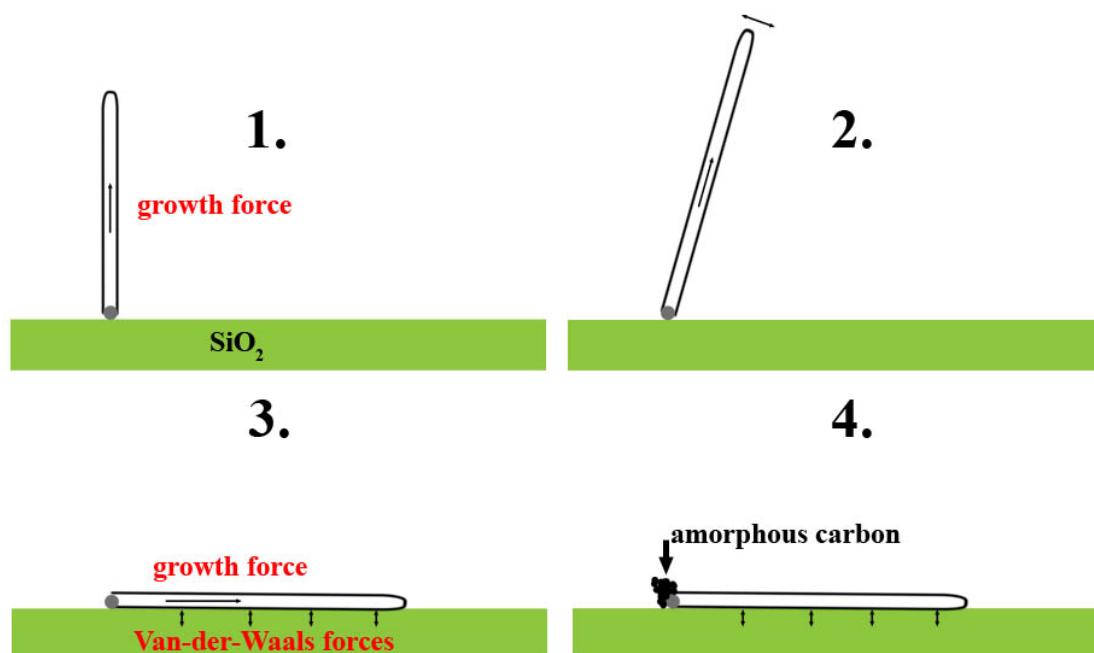


Figure 4.12: Determined growth process for SWNTs with diameters larger than $\sim 0.9\text{nm}$. 1. The SWNT grows straight perpendicular to the surface (base growth model) 2. After reaching a certain height the SWNT falls to the ground. 3. Van-der-Waals interactions bind the SWNT to the surface, while the growth force causes a kink or a bend near the catalyst side. 4. After the SWNT growth is terminated amorphous carbon is formed on the catalyst surface.

Determination of the growth process for non-straight SWNTs

SWNTs with diameters below 0.9nm never show such a characteristic bend or kink near the particle. They are often longer than the SWNTs with diameters $>0.9\text{nm}$ and have mostly a curvy appearance. Similar to the SWNTs with the kink or bend is the catalyst coverage with amorphous carbon at the base of the SWNT.

SWNTs with small diameters are less stiff, have a lower mass and have weaker Van-der-Waals interactions due to the smaller surface area than SWNTs with larger diameters. Therefore, the following growth process shown in Figure 4.13 can be assumed:

1. Due to the smaller diameter of these SWNTs they are most probably much less stiff than SWNTs with larger diameter. Therefore they might already grow in a bended manner.
2. After a certain length they might fall to the substrate surface.
3. Because the Van-der-Waals interactions are weak, it might be possible that they attach and detach from the surface easily. Therefore, they are able to grow longer than SWNTs with larger diameters.
4. The growth termination is either similar to the described above for tubes with diameters $>0.9\text{nm}$, caused by the sticking of the SWNT to the surface or it is similar to the process proposed by Gavillet et al. [139] where it is caused by the poisoning of the catalyst.

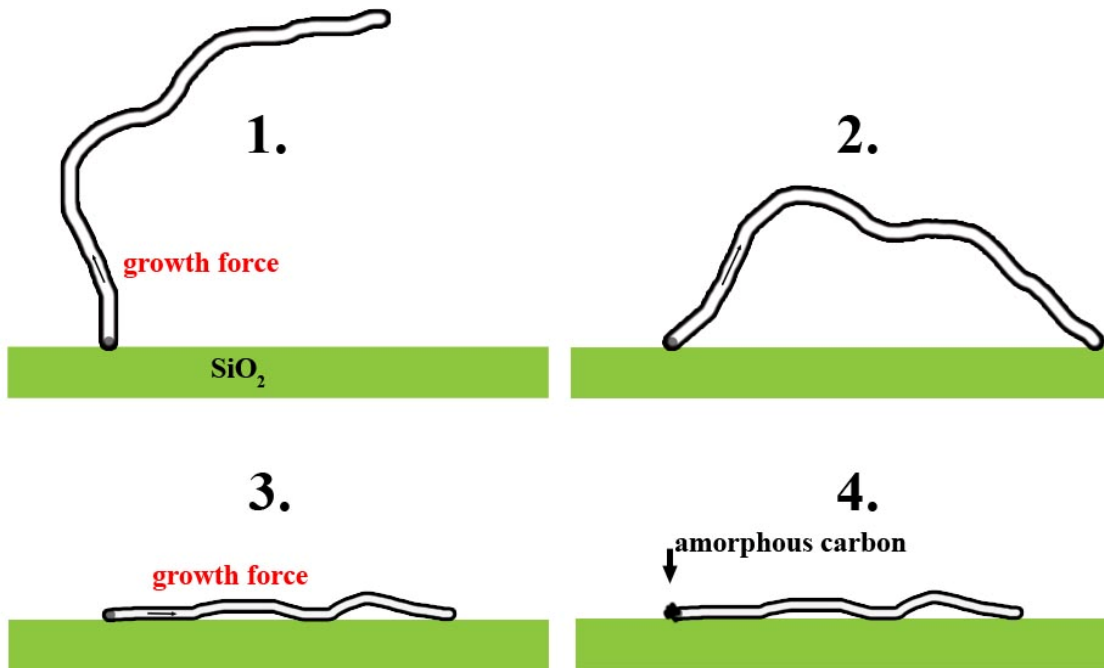


Figure 4.13: Proposed growth process for SWNTs with diameters $<0.9\text{nm}$. 1. The SWNT is not stiff enough for straight growth and it therefore grows more wobbly. 2. The SWNT falls to the surface but due to the weak van-der-Waals interaction it does not stick to the surface. 3. Therefore, the growth may continue. 4. The SWNT stops growing because either poisoning of the catalyst occurs due to amorphous carbon formation or the van der Waals interactions become dominant with a certain length and the SWNT sticks to the surface.

Synthesis of clean SWNTs

As shown in Figure 4.1, Figure 4.4 Figure 4.6, using ferritin for catalyst preparation results in low particle coverage on the surface (with $100\text{particles}/\mu\text{m}^2$ the surface coverage is less than 0.0001%). Unlike processes with other catalyst preparation methods (e.g. sputtering [169] and liquid phase deposition by evaporation of the solvent [74]), ferritin-based particles do therefore not contaminate the SWNTs or influence their growth.

As proposed by the new model described in the appendix and as already shown in earlier investigations [54], the pyrolysis of amorphous carbon can be reduced by increasing the H_2 content. However, for the nucleation of SWNTs with large diameters the Gibbs free formation energy of the carbon formations on the catalyst surface needs to be as high as possible, hence the H_2 content as low as possible. For a growth temperature of 850°C and a CH_4 partial pressure of 156mbar the optimal H_2 partial pressure for the growth of amorphous free SWNTs is 55mbar (growth process #3) as shown in Figure 4.4. At a slightly lower H_2 partial pressure, amorphous carbon deposition occurs (Figure 4.6 a), causing the contamination of the SWNTs and therefore degradation of the contact quality of CNFETs as shown in Figure 4.7. To be on the safe side growth process #4 is actually used

for CNFET production. This process yielded still SWNTs with mean diameters around 2nm.

SWNT density control

Today's most common ferritin immobilization process for catalyst particle formation is to spin coat the ferritin solution on the chip [87, 170-171]. However, with this technique unwanted protein aggregations (5nm-100nm particle size) stick to the surface as well. Applying the ferritin adsorption technique, this effect can be suppressed as shown in Figure 4.1 a). Main reason for using the spin coating technique might be to avoid the long adsorption time of 24h as published by Li et al. [71]. In Figure 4.8 a) it is shown that the ferritin adsorption time has no influence on the protein and hence on the SWNT density on the surface. Therefore, the ferritin adsorption time can be set to 1min, which reduces the processing time drastically. The SWNT density can be controlled by the ferritin concentration in the adsorption solutions as shown in Figure 4.8 b) and Figure 4.9. This allows control of the SWNT density on the surface. It is possible to grow a few SWNT within $100 \times 100 \mu\text{m}^2$ for CNFET device production by e-beam lithography techniques (Figure 4.10) or more than 2 SWNTs on an area of $1 \mu\text{m}^2$ (Figure 4.9). To my best knowledge, there is no other method showing a SWNT density control of the same quality (see state-of-the-art Table 1.3).

Synthesis of individual SWNTs

Figure 4.4 and Figure 4.9 show bundling events of SWNTs. From these image it can be extracted that bundles are formed when two SWNTs meet during growth. They stick together by Wan-der-Waals forces. The growth of several SWNTs out of one single catalyst, as often observed in arc discharge growth [139], can be excluded because the ferritin-based catalysts have diameters in the range of the diameters of single SWNTs (see therefore TEM images of Figure 1.6 b and Figure 2.14). Therefore the proposed assumption for SWNT bundle formation by the sticking of SWNTs due to Van-der-Waals forces [74-75] is the reason for bundle formation in this growth system.

In Figure 4.9 is show that bundle formation is avoided by reducing the SWNT density to $0.02 \text{ SWNT}/\mu\text{m}^2$.

CNFETs

All the above mentioned points (growth of straight clean individual SWNTs with controlled site density low defect densities and diameters around 2nm) results in CNFETs of high qualities. Low device resistances in the range between 30k Ω and 200k Ω were observed.

Based on the high SWNT quality a number of interesting investigations were enabled.

Gas sensors

The effect of NO₂ on the CNFET gate sweep characteristics was investigated (see Figure 1.2) and published in several journals and conference proceedings [28, 30-31, 164]. Mattmann et. al. [28] were able to detect NO₂ down to the ppb regime.

Pressure sensors

Substituting HiPCO SWNTs [35] with straight SWNTs grown directly on the surface from ferritin-based iron catalysts with controlled site densities increased the device yield of high quality and stable SWNT-based pressure sensors [6, 29]. Amongst others, we assume that these results were achieved by the optimal clamping and contact conditions due to the use of clean SWNTs with diameters around 2nm. The straightness of the SWNTs resulted in devices which show responses already at small pressure differences and sensitivities down to 50pA/mbar.

Quantum dots

The SWNT were also used for the production of suspended quantum dot devices published in the journal "Nature Physics" [172]. The high quality of the used SWNTs is reflected in the measured fourfold periodicity of the so called Coulomb diamonds, which can only be observed in devices of high quality and cleanness.

Batch CNFET production by dielectrophoresis

Dissolving SWNTs grown from ferritin-based catalysts by a short ultrasonic pulse into SDBS solution and using this solution to integrate SWNTs by dielectrophoresis techniques results in devices with system resistances which are in the range of 300-1000k Ω . These values are about one order of magnitude lower than resistances reported by other groups using dielectrophoresis for SWNT integration [100]. This confirms once again the high quality of the SWNTs resulting from the investigated process.

4.2 SWNT diameter control and narrowing SWNT diameter distribution

In the previous section, it has been shown that with clean SWNTs from ferritin-based catalyst nanoparticles, with controlled site densities SWNT-based devices of high quality and low system resistances can be produced. These devices were fabricated by localizing the SWNTs by means of atomic force microscopy (AFM). Straight SWNTs with diameters around 2nm were selected for contacting. Contacts were formed by e-beam lithography, metal evaporation and lift-off [30]. This serial process is well suited for prototyping purposes. In order to maintain this quality in parallel batch processing of SWNT-based devices for future commercial applications where individual SWNT selection is not feasible, SWNT material with a distinct mean diameter (~2nm) and narrow diameter distribution is required. Therefore, SWNT diameter control and the growth of SWNTs with narrow diameter distribution are discussed in this section.

This section is divided in two subsections. First, the SWNT diameter dependency on the loading time of the ferritin proteins is shown. The longer an apoferritin (empty ferritin) remain in the solution containing Fe^{2+} ions the more iron can be loaded and the larger the catalyst nanoparticle gets, which in turn results in the growth of SWNTs with larger diameters. These data were published in the journal “Sensors and Actuators” [96].

In the second part, a new method is shown allowing the separation of the ferritin proteins in dependence of the size of the ferrihydrite particle in the protein core by using velocity sedimentation centrifugation. Using size-separated catalyst particles allows the growth of SWNTs with narrow diameter distribution. These results were published in the journal of “Nanotechnology” [159].

4.2.1 Controlling the mean SWNT diameter by the loading time of the ferritin proteins

One advantage of the use of ferritin-based iron catalysts for SWNT growth is that the mean catalyst nanoparticle diameters can be increased by increasing the ferritin loading time which results in an increase of the mean SWNT diameter [71]. Figure 4.14 a) shows box plot diagrams of the particle size distribution for different ferritin loading times and in Figure 4.14 b) box plot diagrams of the diameter distribution of SWNTs grown on these particles are shown. It can be seen that the median (center line) and the mean (black square) of the particle diameter increases by increasing the ferritin loading time. The particle diameter distribution of the commercially available saturated ferritin (also shown in Figure 4.1 d) is match larger, than the distributions of the particles from the self loaded proteins. Figure 4.14 b) shows that the median and the mean SWNT diameter increase by increasing ferritin loading time as a result of the increase of the particle diameter. Additionally, it is shown that the SWNT diameter distribution increases as well by increasing ferritin loading time. The diameter distribution of SWNTs grown from particles produced by loading the

ferritin for 30min (particle formation process #1) and 45min (particle formation process #2) is much narrower than the distribution of SWNTs grown on the saturated ferritin-based particles (Fluka).

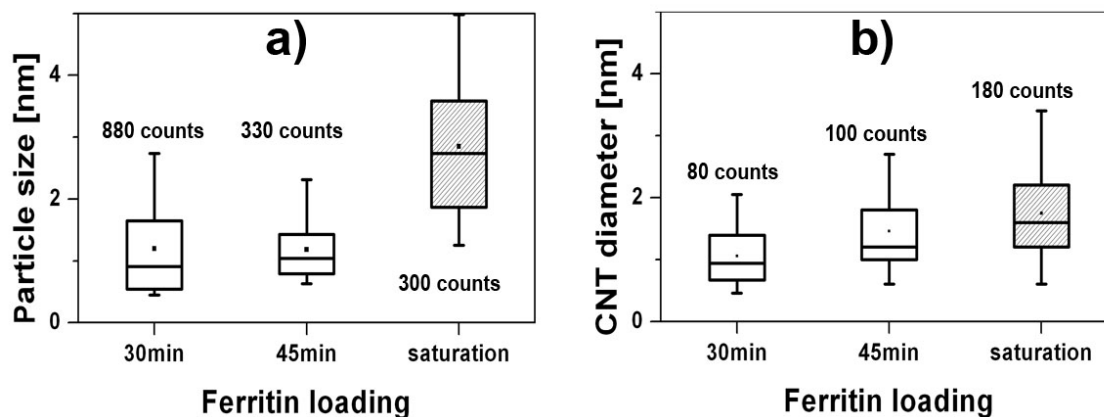


Figure 4.14: Box plots showing a) the particle size distribution for different ferritin loading times and b) the diameter distribution of SWNTs grown on particles formed by different ferritin loading times. The white box plots represent self loaded ferritin and the shaded on commercially available saturated ferritin (Fluka), adapted from [96].

4.2.2 Narrowing SWNT diameter distribution using size-separated ferritin-based Fe catalysts

In the previous subsection, it was shown that the mean particle size and hence the mean SWNT diameter can be controlled by the ferritin loading time. Unfortunately, particle and SWNT diameter distribution are increasing with increasing mean diameter of the catalyst particle and SWNT respectively. This problem is not only known for ferritin-based catalysts, but for any catalyst nanoparticles used for SWNT growth as discussed in section (1.3.6). In this section, a solution to overcome this problem is presented. Using velocity sedimentation centrifugation of ferritin allows separating them by the size of the loaded ferrihydrite particle in loaded the ferritin core. SWNTs grown from size separated catalysts show narrow diameter distributions even for mean diameters around 2nm.

Separation based on a molecule's sedimentation coefficient can be performed by ultracentrifugation and is well known in biochemistry for protein purification [173]. As illustrated in Figure 4.15, sedimentation velocity centrifugation to separate ferritin proteins according to the amount of loaded ferrihydrite in their core was used. A particle's sedimentation velocity is equal to its sedimentation coefficient multiplied by the centrifugal acceleration. The particle's sedimentation coefficient is in turn proportional to its mass and its diffusion coefficient. Since the radius of ferritin does not change upon iron loading, there is a fairly linear relationship between the iron content and the velocity that a ferritin

particle moves in a specific centrifugal field. In order to achieve a more constant particle sedimentation velocity, a glycerol gradient was used whose increasing density and viscosity counteract the increasing centrifugal acceleration experienced by particles as they move away from the center of the rotor. Thus, the distance a ferritin particle moves is a function of the rotor speed and geometry, run time, the composition of the glycerol gradient, temperature, and most importantly the iron content of the ferritin. Although it is clear that larger ferritin encapsulated particles sediment faster, while ferritins with smaller internal particles sediment more slowly, it is not obvious that the technique will have sufficient resolving power.

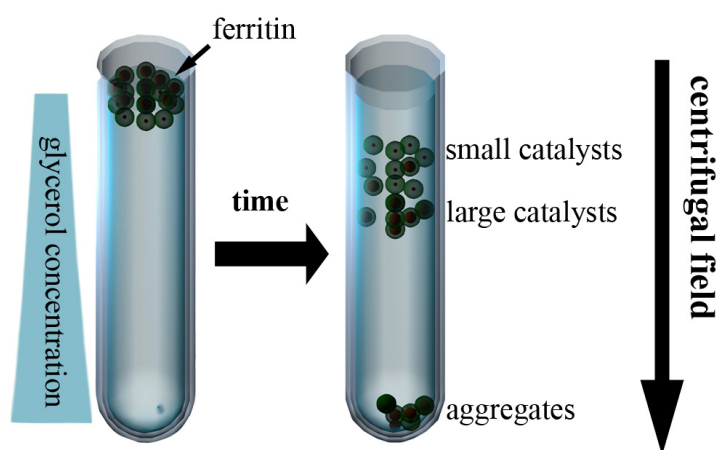


Figure 4.15: Sketch showing the principle of ferritin separation according to the size of their ferrihydrite nanoparticles by means of sedimentation velocity centrifugation, from [159]

Figure 4.16 a) shows a photograph of a centrifugation tube with ferritin in glycerol media after centrifugation for 17h at 30'000rpm. The yellowish and reddish color in the different segments depend on the ferritin concentration and the amount of loaded iron. Initially, the protein was loaded on top and it sediments during the centrifugation towards the bottom of the tube. According to the color, the highest protein concentration is located between 2cm and 3.5cm from the top. Fractions of 250 μ l were taken at 1cm intervals. Figure 4.16 b) shows an AFM height image of Fe₂O₃ nanoparticles on SiO₂ resulting from ferritin proteins collected at the sedimentation distance of 3cm from the centrifugation tube shown in Figure 4.16 a). The diameter distribution of these particles is shown in the histogram at the upper tight part of the Picture. The average particle diameter is 3.7nm and the standard deviation is 1nm. The graph in Figure 4.16 c) shows the mean diameter and the standard deviation of Fe₂O₃ particles resulting from ferritin of different sedimentation distances collected from the centrifugation tube shown in Figure 4.16 a). For comparison, the mean diameter (4nm) and diameter distribution (\pm 1.5nm) obtained from a non-size-separated ferritin (Fluka) is included in the graph. The graph clearly shows that the particle diameter increases with increasing sedimentation distance of the ferritin protein during centrifugation. The standard deviation in the particle diameter distribution increases only from \pm 0.8nm to \pm 1.15nm as

the mean diameter increases from 2nm to 5nm. The fractions collected at 5cm and 6cm were aggregated during the dialysis and could therefore not be used.

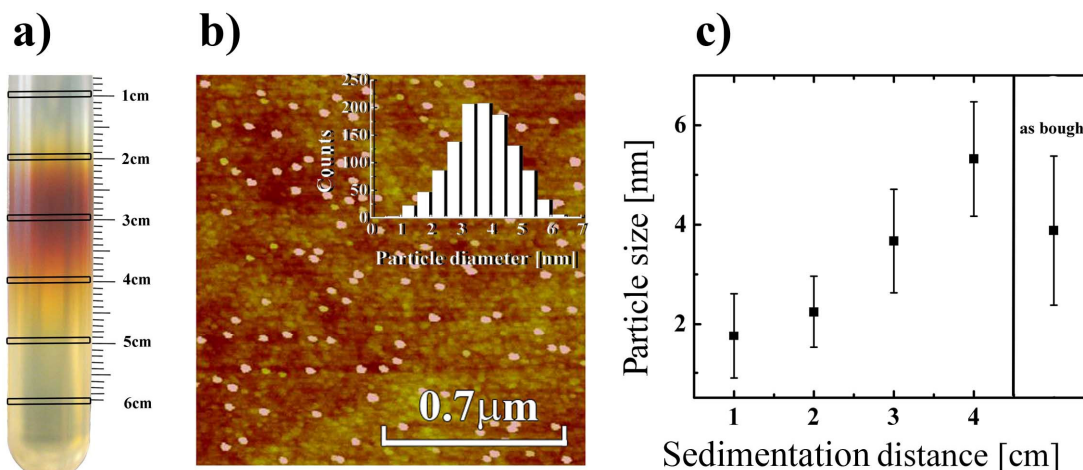


Figure 4.16 a) Picture of the centrifuge tube with iron-loaded ferritin after centrifugation at 30'000rpm for 17h. The sedimentation distances are shown at the right side of the centrifugation tube and the collected fractions are marked by rectangles. Depending on the protein concentration the solution at the respective fraction is yellowish to reddish. b) AFM image of size-separated Fe₂O₃ nanoparticles on the SiO₂ surface prepared with the solution from the fraction at a sedimentation distance of 3cm; color range: 5nm. At the upper right part of the image the particle size distribution is shown. c) Graph showing the mean particle sizes and size deviations resulting from ferritin fractions collected at the sedimentation distances depicted in a). For comparison, mean particle size and size deviation resulting from a non-size-separated ferritin (Fluka) sample is shown at the right part of the graph, from [159]

The growth of SWNTs from a growth island is the first step in the large scale integration process described (see section 1.3.7 and Figure 3.2). In this process, the ferritin-based catalysts are adsorbed onto photolithographically structured surfaces. Figure 4.17 a) shows an AFM image of SWNTs grown on such patterned surfaces from non-size-separated ferritin-based catalysts (Fluka). In this Figure a SWNT with a diameter of 0.7nm which grows from one of the patterned islands is highlighted by arrows. The tube is curved and extremely long. Figure 4.17 b) shows that these aberrant tubes can be eliminated by utilizing size-separated ferritin-based catalysts. After size-separation, only 0.5% of the observed SWNTs show this type of aberrant growth. The diameter distribution of the SWNTs in Figure 4.17 b) and the size distribution of the size-separated catalyst particles that were used to grow them are shown in Figure 4.18 b). Figure 4.17 c) shows SWNTs grown from patterned islands from ferritin-based Fe particles which were size-separated by two centrifugation runs (17 h at 30000rpm). The proteins used for this sample were self-loaded by the loading process #3. The nanotubes are straight (except for a bend or kink near the particle side [96]) and have diameters of 2.1 ± 0.32 nm.

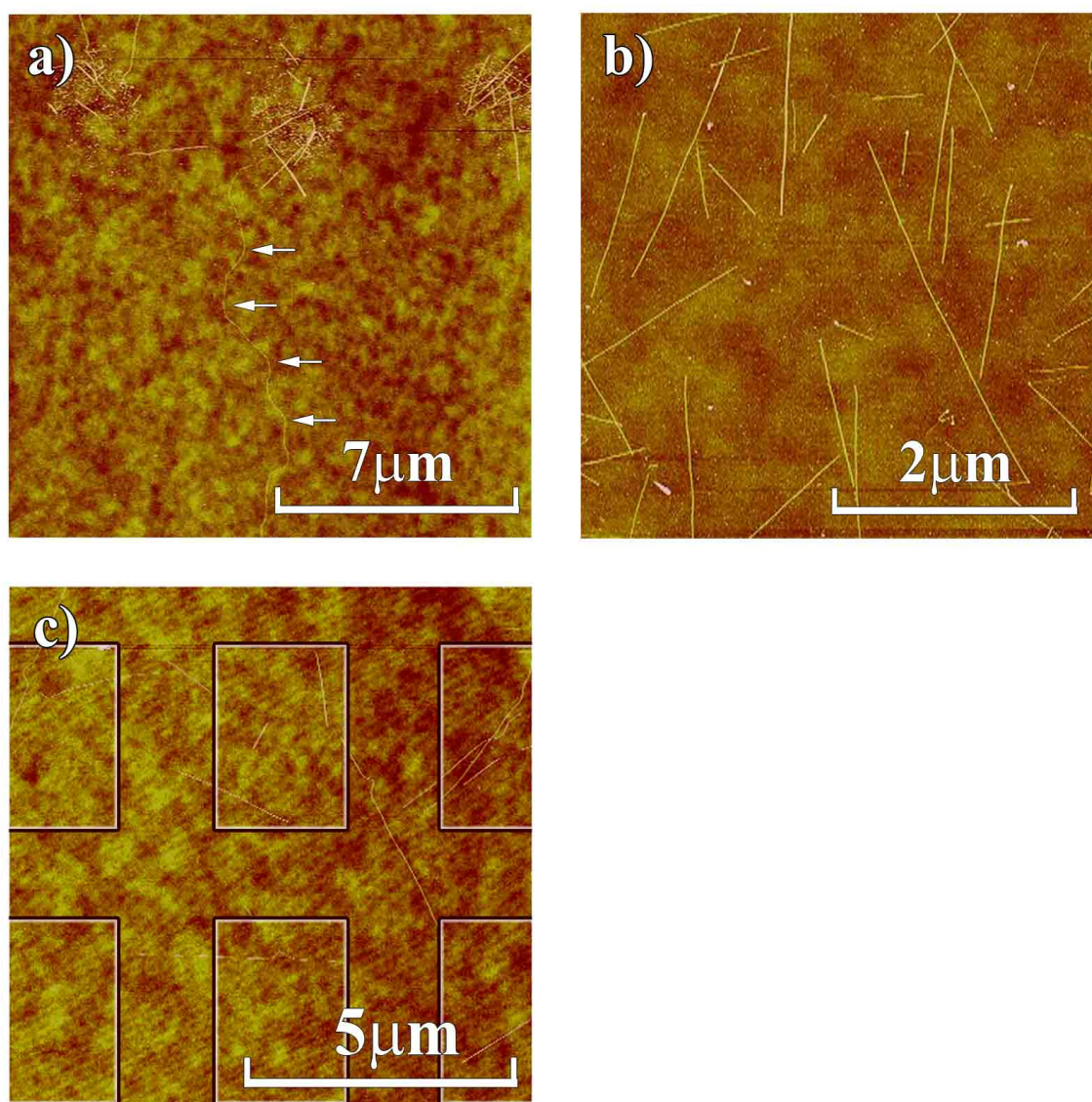


Figure 4.17: AFM images of SWNTs grown from a) patterned catalyst islands obtained from non-size-separated ferritin proteins (the arrows mark a 0.7nm thick non-straight SWNT) b) size-separated ferritin-based Fe catalyst nanoparticles equivalent to those in Figure 4.18 b) and c) patterned catalyst islands obtained from size-separated ferritin-based Fe catalyst nanoparticles (because of the low catalyst density, the approximate position and size of the patterns are indicated by the squares); color range in all AFM images: 5nm, adapted from [159].

The Fe_2O_3 size distributions and the corresponding SWNT diameter distributions that resulted from different centrifugation conditions are depicted in Figure 4.18. So far, the narrowest SWNT diameter distribution ($\pm 0.27\text{nm}$) with a mean diameter of 1.9 nm was achieved by two sequential size separations at 30'000rpm for 17h (Figure 4.18 a), for which

the sample was prepared by collecting the fraction at a 2.5cm sedimentation distance in the first run and the peak fraction from the second run.

Increasing the centrifugation speed has the advantage of reducing the centrifugation time, which might be important for batch production of size-separated ferritin-encapsulated nanoparticles. The centrifugation time was reduced to 2h with the speed at the maximum of 40'000rpm in order to test if the time can be significantly reduced (Figure 4.18 b and Figure 4.18 c). However, in that short time, the loaded proteins did not move as far as the protein centrifuged at 30'000rpm and for 17h. Fractions collected at 1.5cm contained particles with mean diameters of 4.5-5nm. The centrifugation conditions for the particles in Figure 4.18 b) and c) were the same and in both cases the samples were collected at 1.5cm, resulting in a small variation in the mean particle diameter and diameter distributions of the catalysts and the SWNTs. The particle size distribution is larger for these short sedimentation distances than for longer sedimentation distances. Nevertheless, at this short sedimentation time it is possible to separate smaller particles from larger particles and protein aggregates, resulting in diameter controlled SWNT synthesis in terms of avoiding the growth of very long SWNTs with small diameters (<0.9nm) discussed above.

In Figure 4.18 d), the size distribution of Fe₂O₃ particles derived from the non-size-separated commercial ferritin (Fluka) and the diameter distribution of the SWNTs grown from these particles is shown.

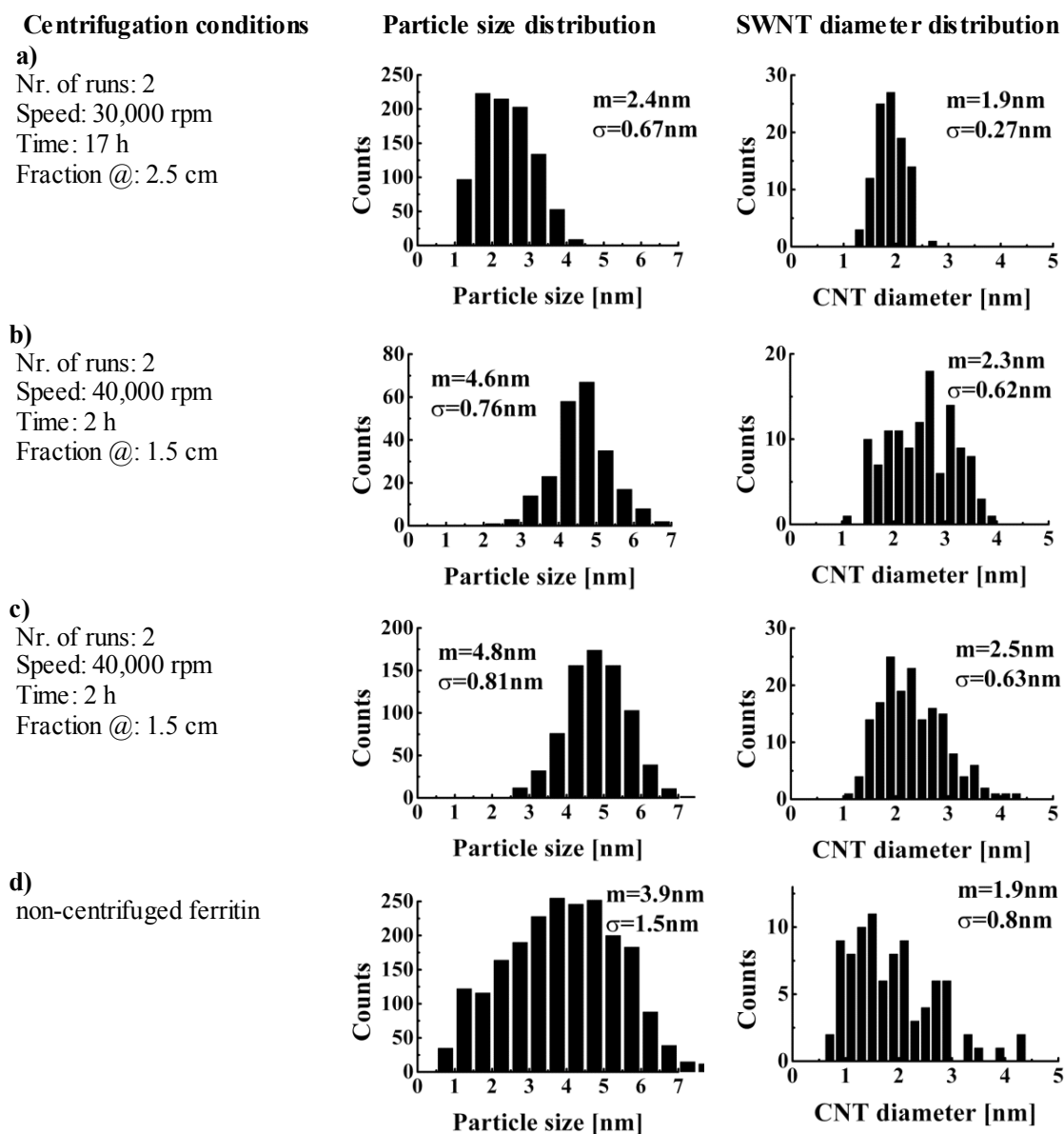


Figure 4.18: Fe_2O_3 nanoparticle size distributions and corresponding SWNT diameter distributions resulting from ferritin protein fractions size-separated under different centrifugation conditions, from [159].

4.2.3 Discussion

Control of the mean SWNT diameter

The investigations shown in Figure 4.14 confirm the result of Li et al. [71] that the mean SWNT diameter is dependent on the size of the catalyst nanoparticle and that it can therefore be controlled by the loading time of the ferritin protein. Consequently, it makes sense to use home loaded proteins containing particles with the desired mean diameter for velocity centrifugation. In order to improve even more SWNT diameter control one can collect fractions at several sedimentation distances, determine the mean diameter of the particles, and then re-centrifuge the fraction containing the ferritins with the desired nanoparticle diameter.

Growth of large diameter SWNTs with narrow diameter distributions

Figure 4.16 shows a much smaller diameter distribution increase with increasing particle size compared to those previously reported [71, 96]. The diameter distribution is also small compared to the commercially available iron-loaded ferritin (Fluka). Figure 4.18 demonstrates that not only the particle size standard deviation but also the SWNT diameter standard deviation is decreased by using ferritin that had been size-separated by sedimentation velocity centrifugation. This enables for the first time the growth of SWNTs of large diameters (around 2nm) with narrow diameter distributions, which according to Chen et al. [49] (see also section 1.3.6) all would result in ohmic contact resistance by contacting them with Pd electrodes, as shown in Figure 4.19 (the achieved results are shown by the red circles).

It could be assumed, that use of home loaded ferritin would result in even narrower diameter distributions. This assumption could not be verified experimentally ($2\text{nm}\pm 0.32\text{nm}$). Anyway, according to the investigations of Jeong et al. [171], who showed that the particles partially diffuse into the amorphous SiO_2 leading to uncontrollable smaller catalyst nanoparticles, it might be difficult to improve the SWNT diameter distribution any further on SiO_2 substrates. One possibility to reduce this effect could be the growth of SWNTs on monocrystalline quartz substrates.

The adaptability of using size-separated catalyst nanoparticle in combination with structuring techniques is demonstrated and shown in Figure 4.17. This is an important result considering the batch integration process described in the following section.

Furthermore, using size-separated catalyst nanoparticles for SWNT growth helps to avoid long curvy tubes whose growth was discussed in section 4.1.4.

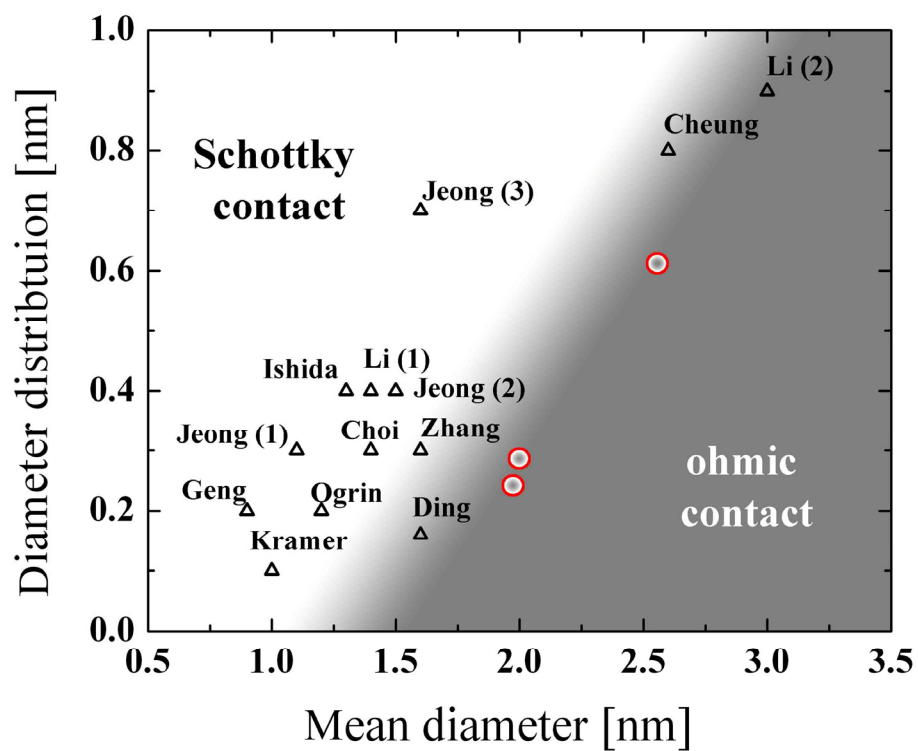


Figure 4.19: State-of-the-art diameter distribution as already shown and discussed in section 1.3.6 including the results achieved by using size separated catalyst nanoparticles for SWNT growth (red circles).

4.3 Batch integration of individual SWNTs by UV lithography

As mentioned in the state-of-the-art in section 1.3.7 batch integration of SWNTs is fundamental for future industrial production of SWNT-based devices and for the production of statistically relevant research data. Here the focus, was put on developing a process, which would allow producing many CNFETs consisting of mainly single-bridging individual SWNTs for statistical investigations of device characteristics in dependence of device parameters, e.g. device resistances, SWNT diameter, length and cleanliness.

For the elaboration of these individual parameters, the devices need to be of high quality and statistical relevance which includes the following points:

- Many integration events on one chip
- SWNT-metal contacts of high quality and long term stability
- Growth of long, straight and amorphous carbon free SWNTs with mean diameters around 2nm and narrow diameter distributions
- Reproducible nanotube-environment interfaces (which mainly means that no electrical charges from dirt particles or adsorbed molecules causes uncontrolled Fermi level shifts)

Even though several methods for batch integration have been proposed, there are no publications showing the integration of mainly single-bridging individual SWNTs. Here, an integration process based on UV lithography was investigated which allows the production of high quality CNFETs consisting of mainly single-bridging individual SWNTs. Table 4.1 shows the individual steps of this process. In the third column the objective of optimization is shown. The expected effects resulting from optimizing the particular process step according to the objective are given in the forth column.

In this thesis, data from four samples are presented. The last four columns of this table show which steps have been applied to each sample, while the color of each column denotes a different process run.

4.3.1 Design

The device design is one major aspect for high SWNT integration yield. Since SWNT growth direction control has not been investigated so far by our group, a design similar to the one shown by Soh et al. [107] was chosen. Regardless of the direction of growth of a SWNT it will be contacted by a second electrode if it reaches a certain length while the first electrode being placed on top of the growth spot. However, the electrode design has not been optimized towards high integration yield yet.

Table 4.1: Individual process steps of the UV-lithography based batch integration process for different samples

#	Process step	Objective	Influence on	Section	S0	S1	S2	S3
0	Design	Electrode arrangement resulting in high integration yield	- Integration yield	4.3.1 4.3.3				
1	Structuring of markers	Producing markers, which do not affect SWNT growth	- Integration yield	4.3.2 4.3.3				
	Non optimized metal markers (Cr/Au)					x	x	x
	Optimized RIE etched markers				x			
2	Patterning of holes for Ferritin adsorption	Having a residual free hole surface for homogenous ferritin adsorption,	- SWNT diameter control - SWNT density control	4.3.2				
	Surface clean by plasma ashing				x			
	Surface clean by NaOH dip					x	x	x
3	SWNT growth	Growth of defect free, clean, straight SWNTs with diameter around 2nm, low diameter distributions and controlled site densities	- Contacts of high quality - Off-state potential - Integration yield	4.3.2 4.3.3				
	Catalysts form non size separated Ferritin; growth process #3				x			
	Catalysts form size separated Ferritin; growth process #4					x	x	x
4	Structuring of electrodes	Residual free electrode patterns	- Contacts of high quality	4.3.4				
	Standard UV lithography (AZ nLOF)				x			
	Optimized UV lithography (reversal bake process with underexposing and low temp. bake)					x	x	x
5	Annealing before lift-off at 60°	Strong adhesion without Cr adhesion layer	- Device yield - Contacts of high quality	4.3.4				
6	Cleaning in NMP at 60° for 72h	Residual free SWNTs and SiO ₂ surfaces	- Off state potential	4.1.3				
8	AFM imaging	As fast as possible	- Integration control - Avoiding contact degradation	4.3.3				
7	Annealing 400°	Better adhesion (wetting) of the contact metal to the SWNT	- Contacts of high quality - Off state potential	4.3.4 4.1.3				
9	Measuring	Pulsed measurements	- Device characterization - Avoiding hysteresis	4.3.4 4.1.3				
10a	Annealing 400°	Removing of gas and vapour adsorbents from the SWNT and/or the surrounding surface	- Off state potential	4.1.3				
11a	Immediate ALD coating	Protection of the SWNT, the surrounding surface and the contacts	- Stable Fermi level - Stable Contacts → long term stable device	4.1.3				
12a	Measuring	Pulsed measurements	- Device characterization - Avoiding hysteresis	4.1.3				
10b	HF dip	Production of suspended SWNTs	MEMS	4.3.1				
11b	SEM		-Device characterization	4.3.1				

The design of the electrodes and growth pad arrangement is shown in Figure 4.20 a). An electrode is placed on top of each growth island, which can also act as contact electrode for a SWNT grown from one of the surrounding growth islands. There are 3 times 10 electrode pairs in a row on a $4 \times 4 \text{ mm}^2$ chip. The gap between two electrodes depends on the quality of the UV lithography process and is between $0.7 \mu\text{m}$ and $1.5 \mu\text{m}$. AFM markers allow one to locate the catalyst particles and the grown SWNTs by AFM after the second UV lithography step⁷. The 3D AFM image of Figure 4.20 b) shows a position where 4 individual SWNTs were contacted resulting in 4 CNFETs. After the integration of the SWNTs, the devices can be protected by Al_2O_3 deposited by ALD which provides long term CNFET stability [29], or the SWNTs can be suspended for the use as special NEMS [7] or quantum dot [172] devices. A suspended SWNT is highlighted in the SEM image of Figure 4.20 c)⁸.

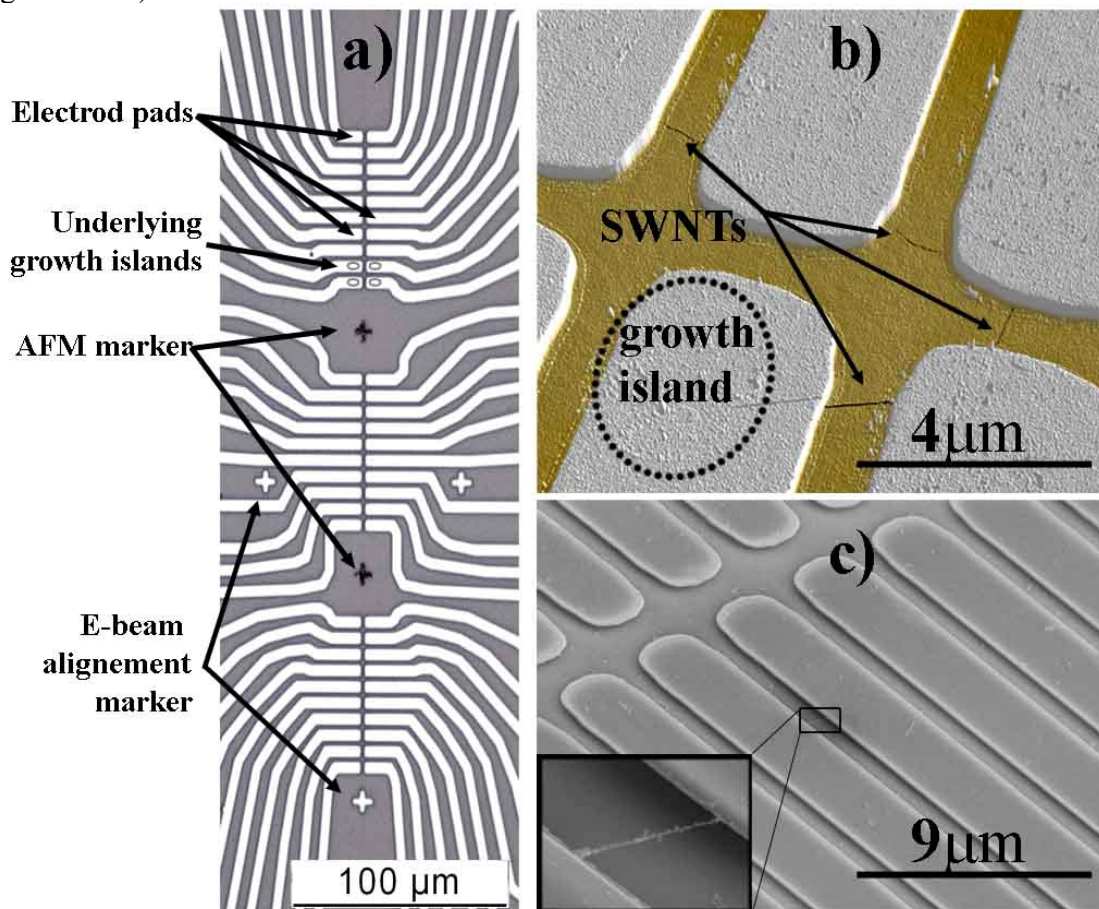


Figure 4.20: Batch SWNT integration by UV lithography (sample S0). a) Optical microscope image of the electrode structure design. b) 3D AFM image of SWNTs grown from patterned growth islands in random directions which were contacted by Pd electrodes; electrode layer thickness is 50 nm . c) It is possible to suspend the SWNTs by etching away the under laying SiO_2 with HF as shown in this SEM image.

⁷ E-beam markers allow post processing which includes etching holes in the post-deposited ALD Al_2O_3 at specific locations or the addition of side gate electrodes.

⁸ The dirt on the SWNTs results from contaminations in the critical point drier.

Figure 4.21 shows the mask design for the electrode patterns. On an $8 \times 8\text{mm}^2$ area (which represents a sample) there are four $4 \times 4\text{mm}^2$ chips containing electrode regions. Each electrode region consists of three rows of 10 electrode pairs.

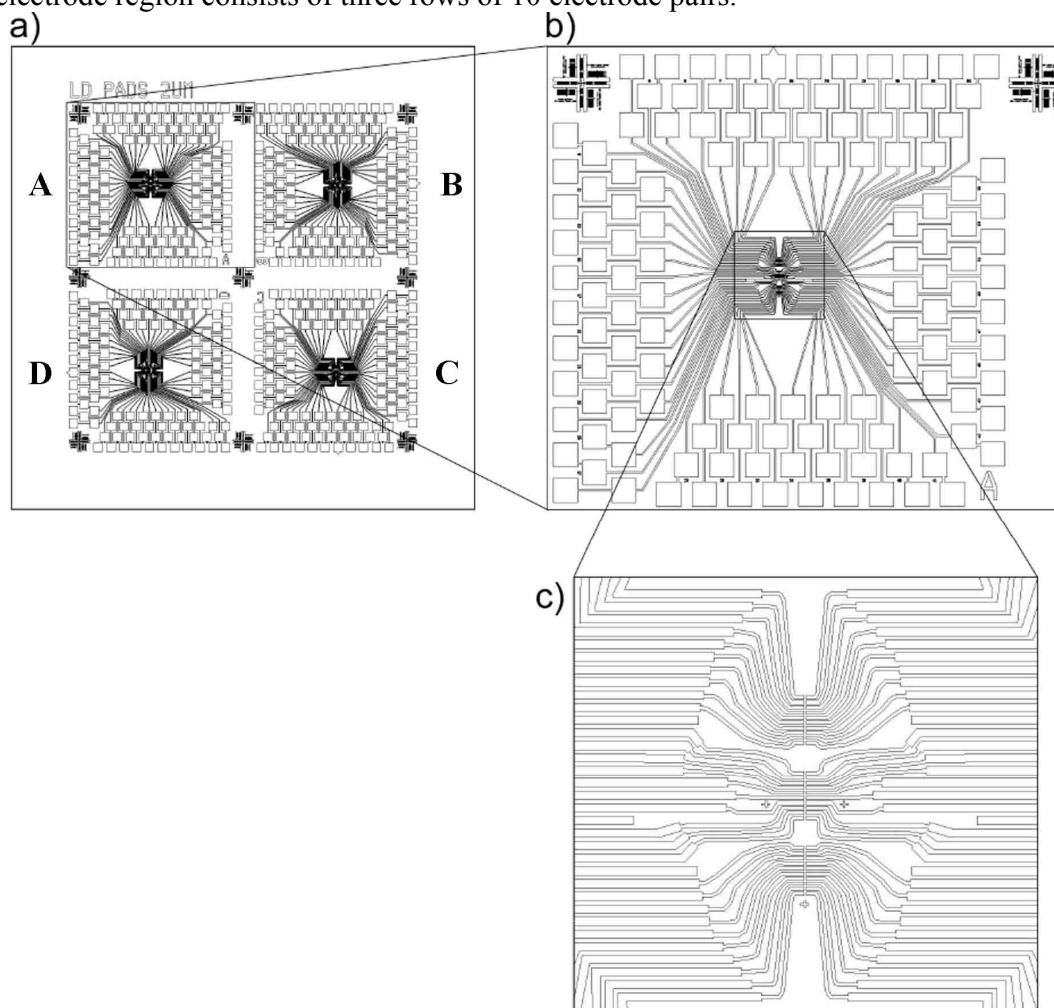


Figure 4.21: Chip design a) a $8 \times 8\text{mm}^2$ sample is divided in four chips labeled A, B, C and D. b) and c) each region consist of 3 electrode rows with 10 electrode pairs each. The electrodes are numbered from 1 to 60, from [160].

4.3.2 Growth of SWNTs from structured catalyst islands

As shown in the process flow of Figure 3.2 in the experimental part, the first step in the UV lithography integration process was applied to structure the alignment and AFM markers. In the second step, holes are structured in the photoresist into which ferritin proteins were adsorbed. The resist was then striped and the remaining proteins on the surface were oxidized and calcined, which results in patterned catalyst islands on the SiO_2 surface at controlled locations. To maintain the high quality in density and diameter control, ferritin adsorption needs to occur on a clean SiO_2 surface.

In Figure 4.22 each of the three AFM images shows 4 structured catalyst islands. The holes, into which the proteins were adsorbed for the formation of the catalyst islands shown in Figure 4.22 a), were produced using the AZ nLOF photoresist process without NaOH treatment (see chapter 3.7). Catalysts areas resulting from ferritin adsorption in these holes often show borders consisting of many catalyst agglomerations as shown in this figure. Inside the growth islands, some large particles occur, which result from catalysts agglomerations, too. As shown Figure 4.22 b), such aggregations were avoided by immersion of the chip for 20s in a 1% NaOH solution, after development of the holes in the photoresist. The catalyst density can be controlled by the ferritin concentration in the adsorption solution. Therefore, it is also possible to increase the catalyst density up to 600particles/ μm^2 as shown in Figure 4.22 c). Particle agglomerations on that sample are due to the high surface density.

The growth of SWNTs from such growth islands was already shown in Figure 4.17 (sample S3). However, there are some factors which can inhibit SWNT growth from the catalyst nanoparticles. Using Cr/Au for the alignment markers resulted in the growth of only very few and short SWNTs. Since other metals such as Ti or Pd were not suitable either, the markers were etched into the SiO₂ layer by RIE.

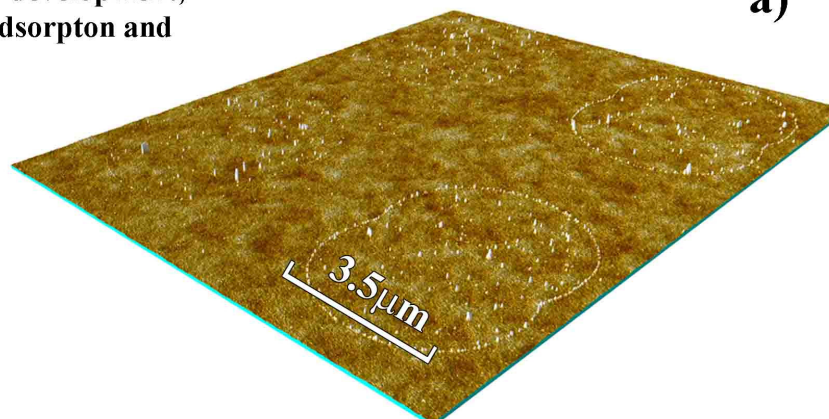
Another treatment which was found to reduce the nucleation yield is the use of oxygen plasma for surface cleaning prior to ferritin adsorption, which was therefore avoided in this process.

4.3.3 Integration yield

After the growth of SWNTs from the structured catalyst islands, the electrode pads were deposited on top of them. The bridging of a contact pair by SWNTs is a stochastic process, and therefore 0, 1, 2, 3, or multiple SWNT were contacted by two electrodes. In this thesis these events were named “single-, double-, triple- and multiple bridging”. Figure 4.23 shows one row of 10 electrode pairs with integrated SWNTs. The SWNTs were grown from size separated catalyst nanoparticles (sample S3) by growth process #4 (see SWNTs in Figure 4.17 c). They have diameters of $2.1\pm 0.32\text{nm}$ and were contacted by Pd electrodes. Four bridging events are enlarged on the right side. From the AFM images, it is often not easy to distinguish whether SWNT bundles or individual SWNTs are present. However, if no other SWNT runs into the SWNT of interest, the latter was regarded as individual SWNT. Therefore, the zoom-in #1 most probably shows a bridging event of an individual SWNT, at #2, two SWNTs were contacted (double bridging event), the zoom in #3 shows the integration of an individual SWNT which is crossed by a second SWNT, and the last zoom in shows a SWNT bundle. At the lower part of the image, pulsed gate sweep measurements show the corresponding device characteristics. The hysteresis effects were completely suppressed by using this technique. All shown SWNTs are semiconducting. From the double bridging event at position #2, no signal was detected. This was the case in approximately 10% of the contacting events recorded by AFM on this sample.

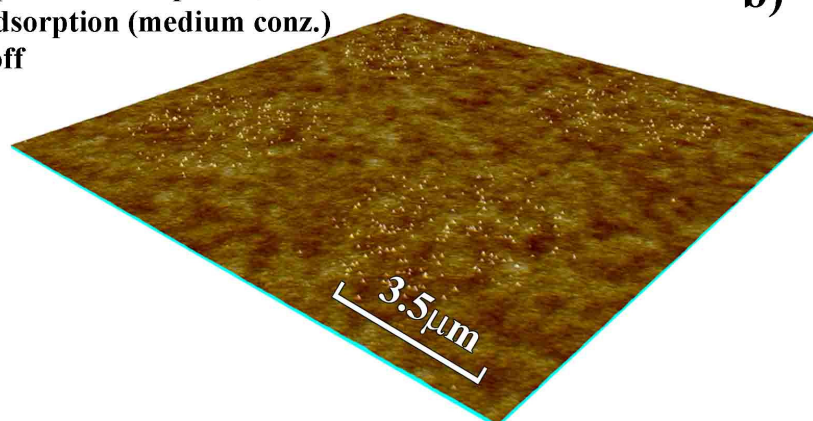
Standard development,
ferritin adsorption and
lift-off

a)



NaOH dip after development,
ferritin adsorption (medium konz.)
and lift-off

b)



NaOH dip after development,
ferritin adsorption (high konz.)
and lift-off

c)

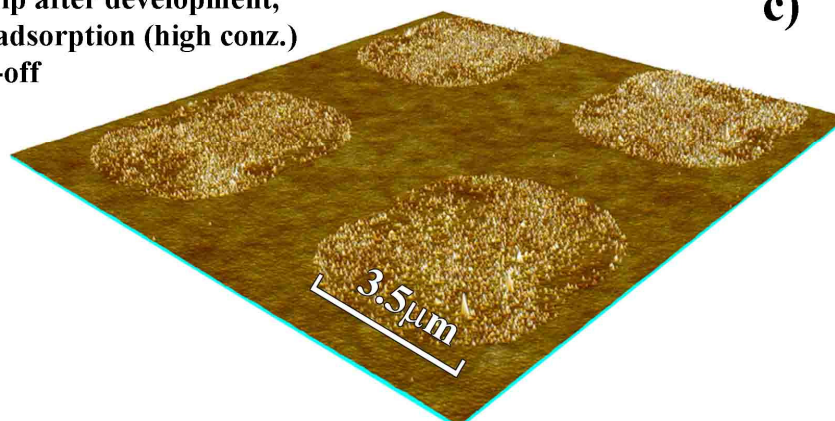


Figure 4.22: 3D AFM images of particle islands structured by UV lithography. a) After development, ferritin (from Fluka) was adsorbed into $2 \times 3 \mu\text{m}^2$ holes in photoresist, the resist was stripped, the protein shells were oxidized and the remaining nanoparticles were calcined. b) After development, the chip was put into 1M NaOH for 20s. c) Same procedure as in b), but the adsorption was performed with a higher concentrated ferritin solution. Color range: 5nm.

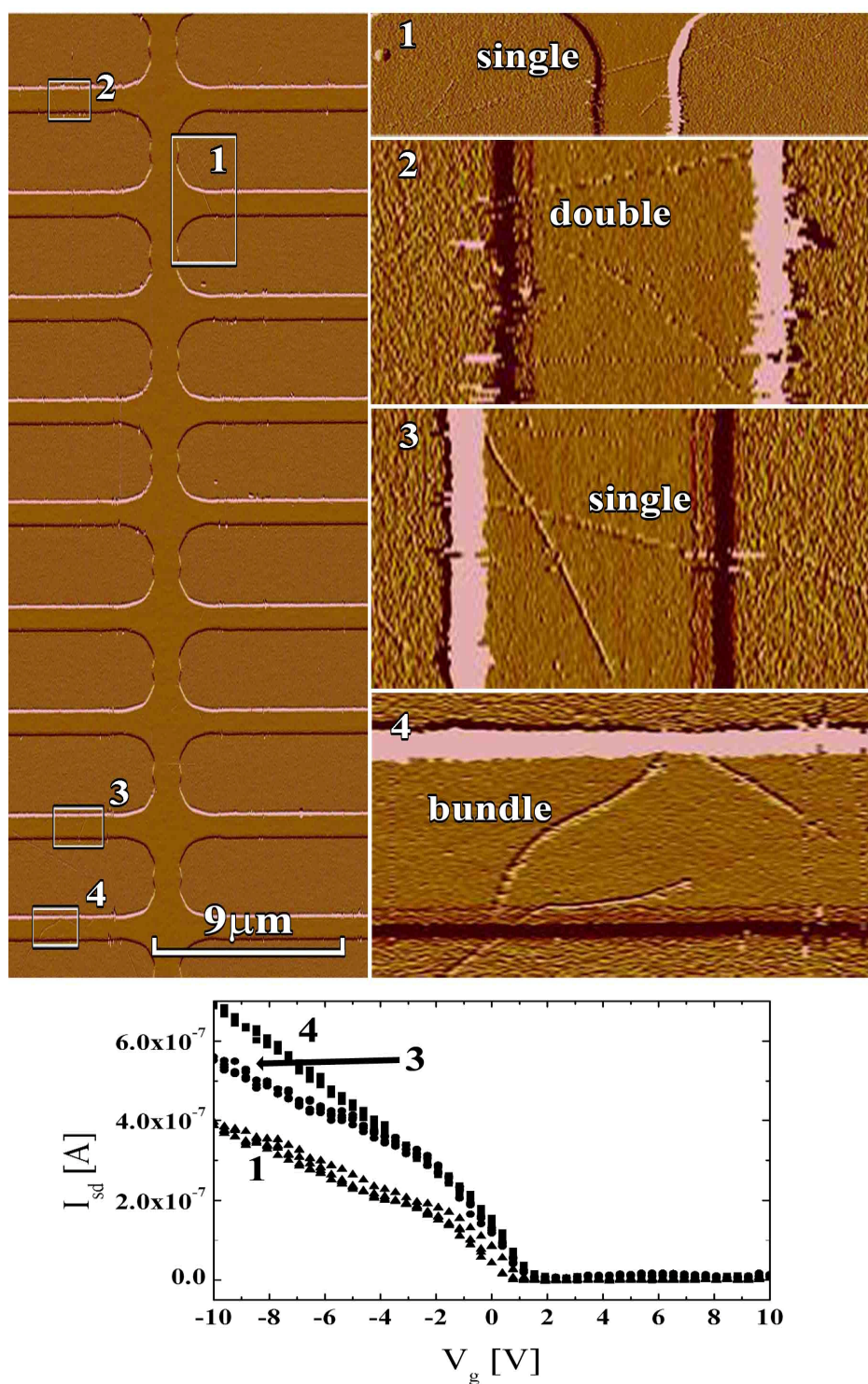


Figure 4.23: AFM amplitude image of a row of electrode pairs contacting randomly grown SWNTs (sample S3 chip A2). The zoom-ins on the right hand side show some of the bridging events assigned by the numbers. The corresponding gate-sweep measurements (pulsed measurements) are shown below the AFM images. No signal was detected from the double bridging event #2.

Also the opposite case has been observed, namely that even no SWNT was detected by AFM an electrical signal was detected. The reason for that might either be, that SWNTs were grown at an unwanted position or, that the resolution of the fast AFM scanning with a scan size of 30 μm was too low to detect perfectly horizontally aligned SWNTs.

In total, 39 CNFETs were electrically measured on sample S3 (all 4 chips A-D). AFM images were only taken of four electrode rows from already contacted SWNTs (chip A1-A3 and B1). Therefore, the correlation between AFM images and electrical measurements can only be made for a few measurements, which means, that in most of the electrical measurements the type of the SWNT bridging event is unknown.

To determine statistics of the integration yield, electrode rows from sample 1 to 3 were scanned by AFM before measuring the devices electrically. The integration yield is defined by the amount of single individual bridging SWNTs within 10 electrode pairs without device shorting over a third electrode. Therefore, the maximum number of devices one can obtain from 10 electrode pair is 19 (see footnote⁹), which was set to 100%. From sample 1 only one electrode row was scanned, while from sample 2 three and from sample 3 four electrode rows were imaged. The results are shown in Table 4.2 and are plotted in Figure 4.24. The chart of this figure shows the integration yield for each bridging type (single-, double-, etc.) in dependence of the average number of SWNTs grown from one growth island as imaged by AFM. The standard deviations are shown in Table 4.2. With decreasing amount of SWNTs per growth island, the integration yield of single-bridging events is increasing, while double, triple, and bundle bridging events are reduced. In average 3.3 SWNTs per growth island (sample 2) were reached by using a ferritin solution corresponding to a particle density of 16particle/ μm^2 . For the other two samples, the particle density was not measured. The electrical measurements shown in the remainder of this chapter originate from the sample with 2.3 SWNTs per growth island (sample S3), which shows the most bridging events of single individual SWNTs.

⁹ With the given electrode arrangement the maximum number of devices without having a device shorting over another electrode pathway is 19. This is for example the case by connecting all the electrodes from one side and all the electrodes from the other side with SWNTs, which results in 18 devices. Additionally the both sides can be connected by only one additional connection, which then would be the 19th device. Any additional connection would then result in a shorting of other devices.

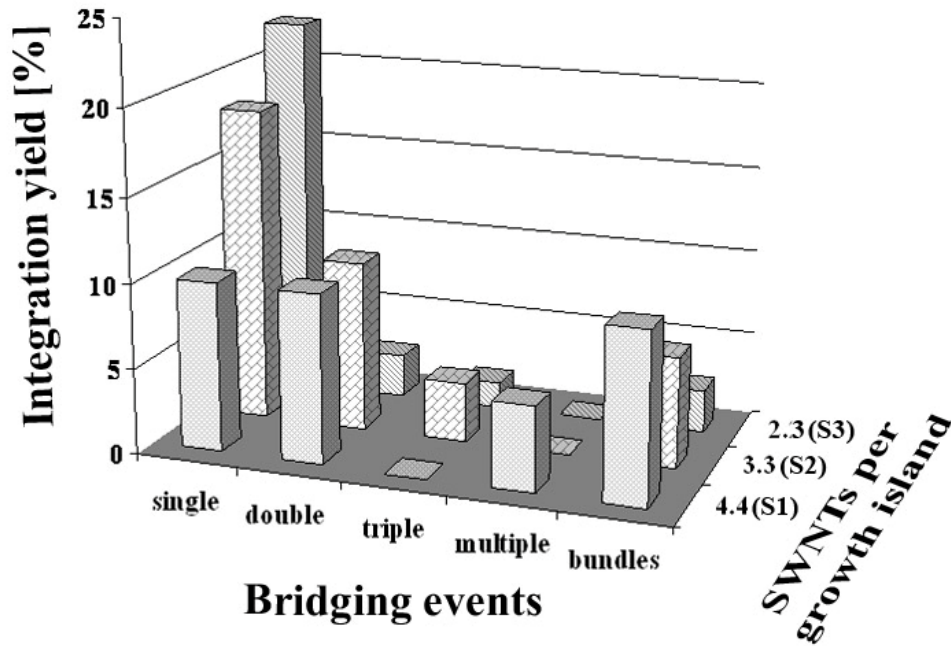


Figure 4.24: Diagram showing the integration yield as a function of the SWNT bridging events and SWNT density as determined by AFM imaging.

Table 4.2: Data with standard deviation of the integration yield shown in Figure 4.24. The data were obtained from 3 times 10 (S2) and 4 times 10 (S3) electrode pairs each except for the first sample, where only 10 electrode pairs were recorded. Therefore, standard deviations for this particular sample cannot be shown.

	Sample S2		Sample S3			
	Average	Deviation	Average	Deviation		
SWNTs per growth island	4.4	3.8	3.3	1.4	2.3	0.9
Single-bridging events per 10 electrode pairs	2	-	3.7	0.6	23	9
Double bridging events per 10 electrode pairs	2	-	2	1	0.25	0.25
Triple bridging events per 10 electrode pairs	0	-	0.7	1.2	0.15	0.25
Multiple bridging events per 10 electrode pairs	1	-	0	0	0	0
Bundle bridging events per 10 electrode pairs	2	-	1.3	1.2	0.25	0.25

4.3.4 Production of CNFETs with low contact resistance

As mentioned in the introduction (1.3.6) low contact resistance is required for high quality CNFETs. Therefore, the growth of SWNTs with diameters around 2nm is crucial. However, as important as the SWNT diameter, is the cleanliness of the SWNTs in the contact region. Any contamination might result in an increase of the contact resistance, which results in a higher device resistance.

Figure 4.25 a) shows an AFM image of a SWNT recorded inside a structured electrode pad after development of the photoresist. For this process the AZ nLOF UV lithography process (see chapter 3.7) had been used. The entire SiO₂ surface and the SWNT are covered by particles. Standard UV lithography processing requires oxygen plasma ashing after development to remove all residuals from the surface. However, using oxygen plasma after development of the contact pads would destroy the SWNTs. Applying a NaOH dip, as proposed for cleaning the surface in the ferritin adsorption holes (section 4.3.2), results in the loss of the resist lift-off profile. Therefore, another solution needs to be found. Figure 4.25 b) shows the surface recorded in a structured electrode pad after development, and it is almost free of residuals. This clean surface results from a special UV lithography process based on overexposing the AZ 5314E image reversal photoresist, in combination with a low reversal bake temperature (chapter 3.7). This process results in the widening of the electrode structures so that the gap between two electrodes decreases from ~1.5μm to ~0.7μm (process control).

A typical gate sweep characteristic of a non-passivated s-CNFET is shown in Figure 4.26 a) recorded on sample S3 chip D (similar curves with AFM image correlation recorded on Sample S3 Chip A are shown in Figure 4.23). The electrode gap was 1μm, the gate oxide thickness was 200nm and V_{sd} was set to 30mV and the curve was measured by the pulsed method. The current is still increasing at the minimum gate potential of -10V. The gate coupling is insufficient to reach the saturation plateau. Therefore, it was not possible to determine the on-state current. For the determination of the on-state current distribution shown in Figure 4.26 b), the highest measured current value was chosen instead. Therefore, the device on-resistances shown on the top axes are only approximate. The distribution shows the maximal measured current values of 23 s-SWNTs and 16 SGS-SWNTs on sample S3 (all 4 chips). All measured events (eg. single-bridging, double bridging, triple bridging, multiple bridging and CNFET devices consisting of bundles) were taken into account. However, as shown in Figure 4.24, most of the devices consist of only one individual bridging SWNT.

Most of the SWNTs have highest current values between 0.3μA and 0.6μA, which corresponds to device resistances between 100kΩ and 40kΩ. Only 13% of the devices show highest current value below 0.1μA. The highest obtained current value was 1.5μA, which would correspond to a device resistances of only 20kΩ.

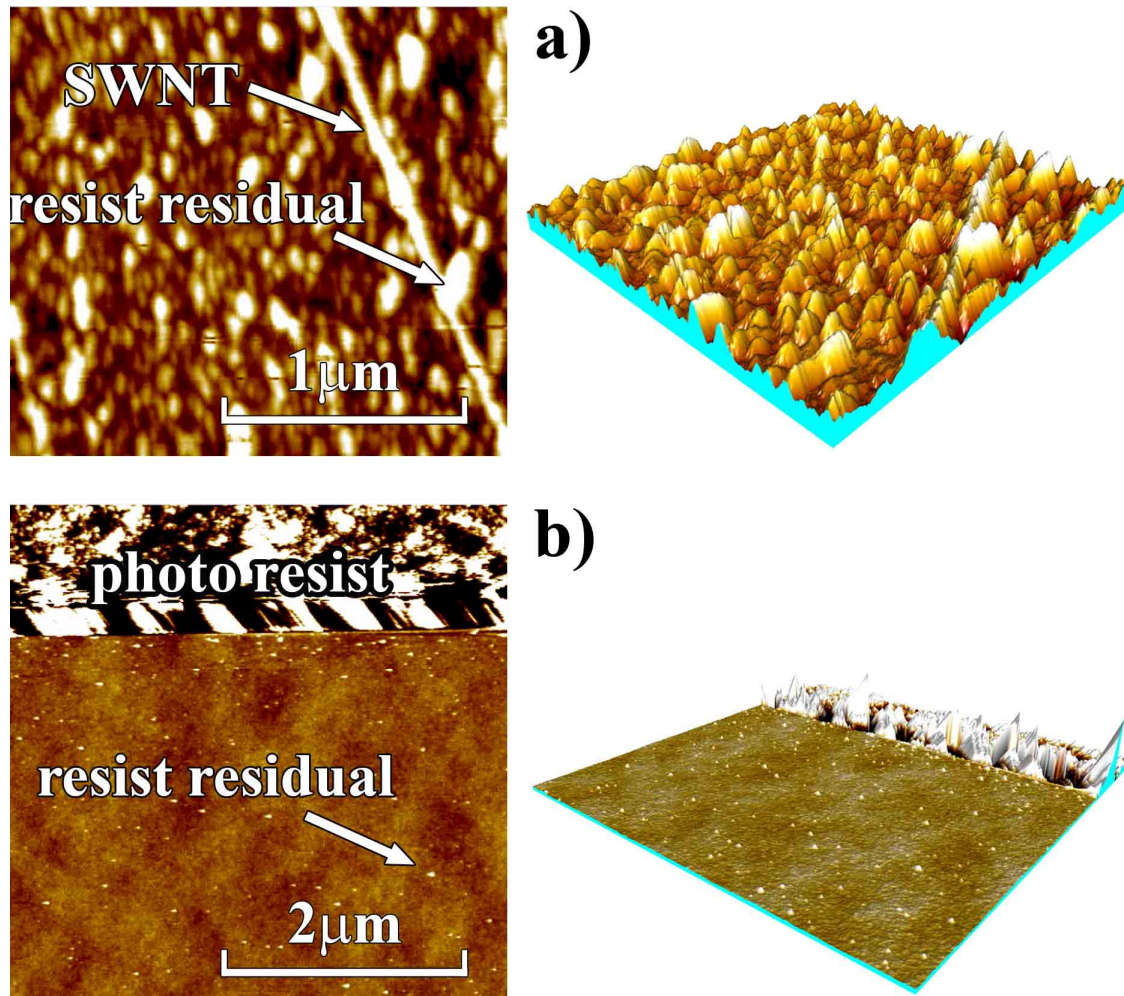


Figure 4.25: Top view and 3D view AFM images of the SiO₂ surfaces in developed electrode pad structures resulting from the a) standard UV lithography procedure with AZ nLOF resist b) process where the AZ 5314E image reversal bake photoresist that was underexposed and the reversal bake temperature was set to the specified minimum of 110°C.

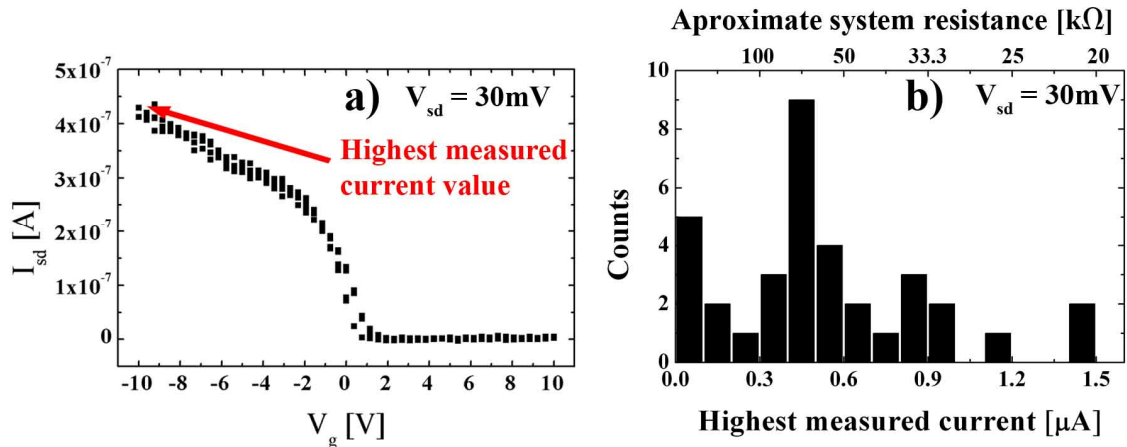


Figure 4.26: a) Gate sweep measurement (pulsed method) of a s-SWNT (Sample S3 Chip D) integrated by the investigated UV lithography providing clean contact areas (see Figure 4.25 b). The high on-state current did not reach saturation at a minimum gate potential of -10V . b) Highest measured current values of 23 s-SWNTs and 16 SGS-SWNTs CNFETs measured in the limited measurement range of $+10\text{V}$ to -10V . The SWNTs were grown from size separated catalyst particles and have diameters of $2.1 \pm 0.32\text{nm}$.

4.3.5 Production of CNFETs with reproducible off-state potentials (threshold values)

As already discussed in the introductory part, CNFETs for the sensor market needs to have reproducible and long term stable device characteristics. Helbling et al. have recently shown, that it is possible to make CNFETs long term stable by passivating them with ALD Al_2O_3 [29]. Reproducibility in device characteristics in particular in the position of the hysteresis, the hysteresis width and the on-state current has only been mentioned by Rispal and Schwalke so far [101], but statistical data are still missing.

In this section, the CNFET gate sweep measurement results from sample S3 are presented. As already described in the previous section and shown in Figure 4.26 overall 23 s-SWNTs and 16 SGS-SWNTs (see bridging statistics of Figure 4.24) were measured after cleaning the devices for 72h in 60°C NMP and subsequent annealing of the sample at 400°C . After the first measurement session, the sample was annealed again and immediately coated by ALD Al_2O_3 for protection from environmental influences. 7 s-CNFETs and 9 SGS-CNFETs survived this additional process steps (on all 4 chips of sample S3). In the first part, CNFETs before and after passivation are compared. Then the effect of the time period the device was exposed to ambient air after annealing on the CNFET characteristics is shown. In the last part, the effect of annealing and ALD protection is presented, with the result, that all 16 CNFETs show reproducible off-state potential.

Effect of Al_2O_3 passivation on the CNFET characteristics

Figure 4.27 shows gate sweep measurements of a s-SWNT and of a SGS-SWNT before and after passivation with ALD Al₂O₃. The effect of ALD Al₂O₃ passivation on SWNTs with Cr/Au contacts was discussed thoroughly [29]¹⁰. Here, the effect of the passivation on SWNTs contacted by Pd electrodes is shown.

Figure 4.27 a) shows the pulsed gate sweep measurement of a non passivated s-CNFET. The n-branch is completely suppressed, while the p-branch does not reach saturation. Figure c) shows the same device after annealing and ALD passivation. The highest current value was decreased by a factor 12. A strong decrease in the highest current was observed in most s-CNFETs and in some of the SGS-CNFETs. Many devices were not measurable any longer after ALD passivation. Beside the strong reduction of the current, a slight increase of the n-branch can be seen, which was observed in all the measured s-CNFETs after ALD Al₂O₃ passivation. Therefore, the off-state potential can be determined. This is the potential of the minimum current between the p- and n- branch of a gate sweep characteristics (see chapter 2.2.2). With the complete suppression of the n-branch a minimum would not be determinable. Using the off-state potential instead of the threshold value allows comparing SGS-SWNTs with s-SWNTs.

Figure 4.27 b) shows a typical measurement of a SGS-SWNT. The on-state current is almost 1 μA. The off-state potential is situated at a gate voltage of 4V. In contrast to the s-CNFETs, most SGS-CNFETs showed only a slight current decrease in their on-state current after ALD of Al₂O₃ (Figure 4.27 d), and the device characteristics remain similar except for an off-state potential shift of almost -4V.

Influence of the time period between annealing and measuring of the CNFETs on the threshold value

Figure 4.28 shows the influence of the time period between unloading the sample from the annealing oven and the measurement of the device on the threshold value. This experiment was performed with the CNFETs of sample S3 before passivation. The CNFETs were annealed in vacuum at 400°C for 1h and then measured at different times. Figure a) shows gate sweep characteristics of the same CNFET measured 10min and 250min after unloading the sample from the annealing oven. A large shift in the threshold value¹¹ from -0.75V to 2.25V can be observed. Figure b) shows gate threshold values for 7 different s-CNFETs in dependence of the time which passed between the annealing of the sample and the measurement of the device. Each device represents one measurement point¹². The standard deviations results from the readout process of the threshold value. The saturation curve shows a clear dependence between the time after annealing and the threshold value. Here, only semiconducting devices were chosen in plotting this curve. However, the same dependence was also observed for the off-state potentials of SGS-CNFETs.

¹⁰ An important result from this publication for the understanding of the last part of this section is that ALD passivation results in CNFETs with stable threshold values.

¹¹ The gate thresholds was defined by the potential where the current starts to increase.

¹² Measuring several devices at the same time was not supported by the given measurement setup.

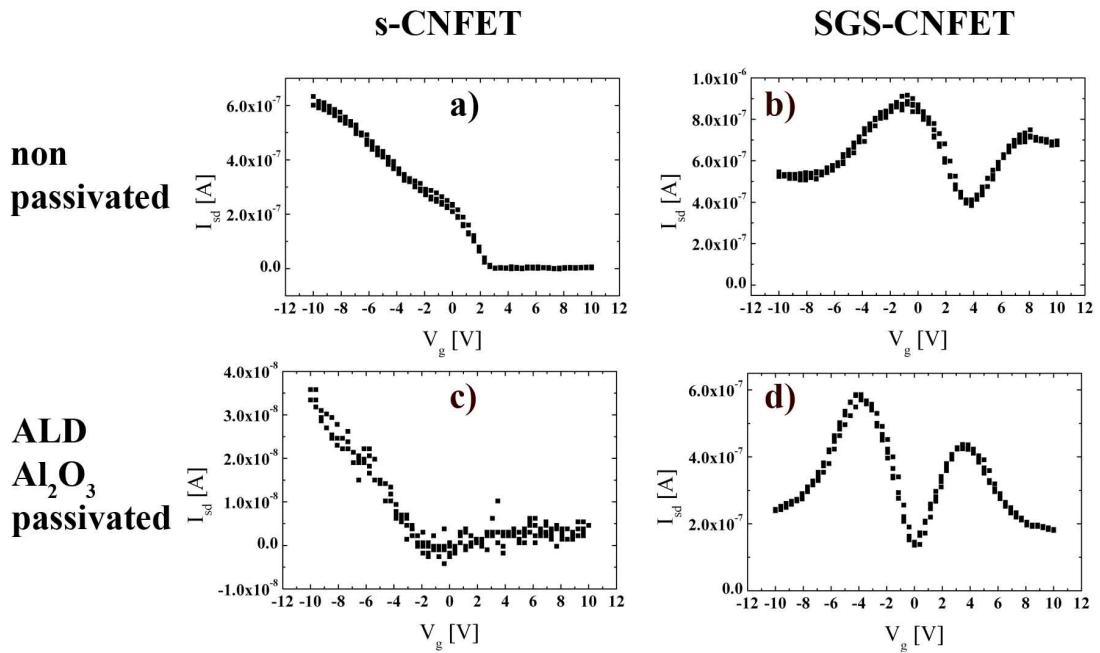


Figure 4.27: Gate sweep measurements of a s-CNFET and a SGS-CNFET before and after passivation with ALD Al_2O_3 . V_{sd} was 30mV in all measurements.

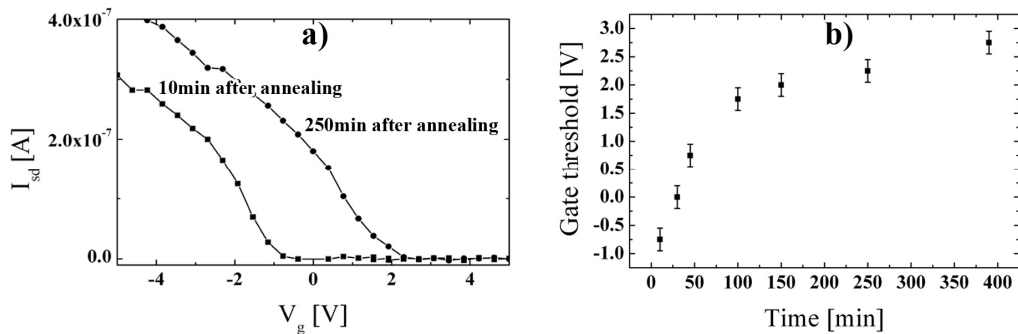


Figure 4.28: Dependence of the gate threshold value on the exposure time to ambient air after annealing. a) Gate sweep measurement of the same s-CNFET recorded 10min and 250min after annealing at 400°C in vacuum. b) Gate threshold values from different s-CNFET devices measured on the same chip at different times after the sample had been annealed. In all measurements, V_{sd} was 30mV.

Effect of annealing and ALD protection on the off-state potential

From the knowledge that ALD Al_2O_3 passivation results in stable threshold values in combination with the results obtained from the annealing experiment above, it can be thought that the threshold value of all devices could be fixed to only one potential by immediate passivation of the devices after the annealing step. The results of this experiment are shown in the following.

Figure 4.29 focuses on the off-state potentials of s- and SGS-CNFETs which were passivated by ALD immediately (~ 1 min) after the annealing procedure. The CNFETs are

from sample S3. The measurements were performed several days after ALD encapsulation and several hours passed between the first and the last measurement. Figure 4.29 a) shows the gate characteristics of the off-state current region of 7 SGS-SWNTs. All off-state potentials are situated between 0V and -1V. Figure 4.29 b) shows the measurement of 4 s-SWNTs. Their off-state potentials are also between 0V and -1V. Figure 4.29 c) shows the distribution of the off-state potentials¹³ of the 7 s-CNFETs and 9 SGS-CNFETs with the mean value at -0.7V and a standard deviation of ± 0.33 V.

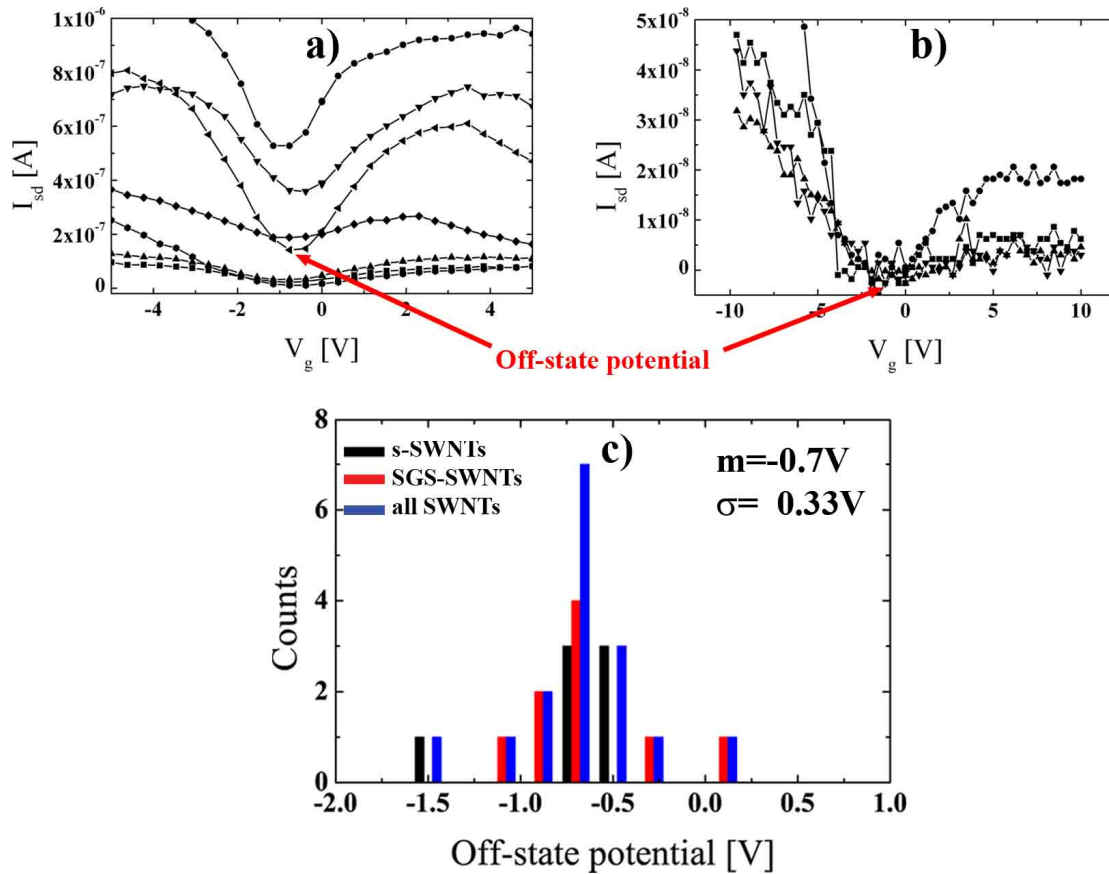


Figure 4.29: Investigations of the off-state potential of CNFETs that are all measured on sample S3 after annealing and immediate (~1min in ambient air) encapsulation by ALD Al_2O_3 . The SWNTs with diameters of 2.1 ± 0.32 nm were grown from size separated catalyst nanoparticles and were contacted with Pd by the described UV-lithography process. a) and b) are showing the off-state current area from gate sweep measurements of 9 SGS-CNFETs (normalized to the off-state current of 10^{-7} A) and 7 s-CNFETs, respectively. c) Off-state potential distribution determined from the measured SGS-SWNTs and s-SWNTs. All electrical measurements were performed with a V_{sd} of 30mV.

¹³ The off-state potential was defined by taking the minimum value of a second or third order polynomial fit through the data in the off-state potential region

4.3.6 Discussion

Growth at controlled location with controlled site density

A major advantage of the investigated integration process is that it is based on using ferritin for catalyst preparation. Therefore, all the advantages of SWNT growth from ferritin-based catalyst discussed in chapter 4.1.4 and 4.2.3 are maintained (eg. SWNT density and diameter control on the surface, growth of individual, clean and straight SWNTs). To maintain the quality in SWNT density control a NaOH dip is required after development, which removes remaining photoresist particles on the surface (Figure 4.22 b). Otherwise, the proteins stick to these photoresist residual particles and form agglomerations during the resist stripping process as shown in Figure 4.22 a), which leads to a loss in density control and in a larger particle size distortions.

To maintain the SWNT nucleation yield, as it was found in section 4.1, it is recommended to omit any plasma ashing treatments and to structure the markers by RIE etching, instead of metal evaporation (Cr/Au, Pd or Ti). We suggest that Cr or Au atoms diffuse at 850°C on the SiO₂ surface and adsorb on the surface of the catalysts, which reduces the strength of the catalytic reaction or binds the initial graphene layer stronger to the catalyst surface, which inhibits the SWNT nucleation. Ti is etched during the H₂ treatment at 850°C and Pd is itself a catalyst for the methane cracking reaction, which results in the formation of amorphous carbon on the surface. It is known, that the surface energy of the catalyst support material has an impact on the catalytic strength (see appendix 6.1.2). Therefore, it can be assumed that O₂ plasma treatment which changes the surface energy of SiO₂ due to dehydrogenation reactions and the insertion of charge traps has an influence on the SWNT nucleation yield. However, detailed investigations would be required to claim that O₂ plasma treatment indeed has an impact on the SWNT nucleation yield.

In conclusion, it is possible to grow SWNTs of high quality and straightness from defined locations (lift-off resolution approximately $\pm 0.5\mu\text{m}$) with the desired density and diameter.

Integration yield

The electrode design and the surface SWNT density control are the two important parameters for yielding a large percentage of CNFETs consisting of single-bridging individual SWNTs. The design was chosen in a manner that the SWNTs can grow in random directions. Direction control is still a target, but this process results in an acceptable yield for statistical studies. A second advantage of this design is that each electrode is placed on a growth pad. This helps to maximize the growth area, and hence the catalyst density can be kept low, which results in fewer SWNT bundles. As already mentioned, the design has not been optimized yet. That the integration yield of individual SWNTs can be controlled by the SWNT density, hence by the catalyst density on the surface, is shown in Figure 4.24. The data in this diagram originate only from three samples. Therefore, the optimum integration yield has not been determined yet. However, these are the first statistical data on the integration yield distinguishing between the type of SWNT

integration (single-, double-, triple-, multiple bridging events and the integration of SWNT bundles) in a batch process shown so far. An integration process yielding an average of 14 CNFET devices consisting of only individual SWNTs on an area of $4 \times 4 \text{mm}^2$ has not been reported yet. Extrapolated to an entire 4" wafer would make an average yield of almost 7'000 CNFETs, which is 7 times higher than the amount of devices produced on a wafer reported by Rispal and Schwalke [114]. The production of a large amount of CNFET devices by different processes has been reported by others (see-state-of-the-art in chapter 1.3.7). However, statistical data of the type of integration has not been considered in any of their publications.

Contact resistances

Figure 4.26 b) shows that it is possible to produce clean contact areas by UV photolithography, which is important for low CNFET on-state resistances. Four optimizations of the UV lithography enabled this residual free surface:

- Using hydrogenated SiO_2 surfaces reduces the adhesion quality to the photoresist
- Reduced UV exposure results in a reduced cross linking of the photoresist
- Applying of a reduced reversal bake temperature results in a reduced cross linking of the photoresist
- Overdeveloping of the structures increases the etch time of the residuals on the surface

These process optimizations result not only in residual free surface but also in a broadening of the structure by approximately $2.6 \mu\text{m}$. In an optimal process the inter-electrode distance is approximately $0.7 \mu\text{m}$. The CNFETs used for the data shown in Figure 4.26 had electrode-electrode gaps of approximately $1 \mu\text{m}$. This shows that for these devices on sample S3, the UV lithography process was not optimal regarding contamination free contact areas. This might be the reason for the approximately 10% inactive devices. Nevertheless, device resistances between $50 \text{k}\Omega$ and $100 \text{k}\Omega$ show that the high quality contacts obtained by the e-beam lithography integration process can be maintained. For comparison, consider also the work produced in our group ref. [29] where a CNFET(channel length of $1 \mu\text{m}$) with an on-state resistance of $44 \text{k}\Omega$ was presented. For a state-of-the-art comparisons consider also Table 1.4.

Nevertheless semiconducting SWNTs show still asymmetric gate sweep responses indicating, that a Schottky barriers are still present also for SWNT with diameters around 2nm . Therefore, I suggest increasing the mean SWNT diameter even to 2.5nm . The suppression of the n-branch shows additionally that contact doping is still present. Whether this doping is related to adsorbed molecules on the surface or to the SiO_2 surface cannot be determined yet. It might be interesting to see, if an annealing of the chip prior to metal evaporation in vacuum at approximately 150°C - 200°C would reduce this effect.

The bars in Figure 4.26 b) showing extremely high on-state currents might originate from devices with several SWNT or SWNT bundles.

The high device resistances of some devices might be related to the non-optimal process run. It would be interesting to see whether the distribution can be narrowed by a run resulting in absolutely clean contact areas. It might then be possible to distinguish between an individual bridging and a double bridging event just by measuring the on state current. Therefore, the use of a thinner SiO₂ layer as back gate is crucial. This would enable a stronger gate coupling, which would result in the observation of a saturation current in the gate sweep measurements which allow one to determine the proper on-state currents.

ALD passivation of Al₂O₃

ALD passivation of Al₂O₃ makes the CNFETs long term stable. This has been shown in our group by Helbling et al. [29]. The effect of ALD passivation of Al₂O₃ was investigated thoroughly in that publication. Therefore, here only differences to the results published by Helbling et al. are discussed. In the work of Helbling et al., it was shown that the on-state current decreases by passivating the device with ALD Al₂O₃. However, a decrease by more than a factor of 10, as shown in Figure 4.27, was not observed. This drastic current decrease could be related to the unloading of the sample from the annealing oven at 100°C. Furthermore, between lift-off and ALD passivation the sample was exposed to ambient air for approximately 72h (AFM imaging and electrical measurements). It is accepted that the oxidation of the metal at the SWNT-metal interface is the reason for device degradation over time [29]. This oxidation process might be increased at elevated temperatures. Therefore, this experiment needs to be repeated by performing the annealing directly in the ALD chamber. This change of the process procedure would avoid any oxidation of the contact metal.

In Figure 4.27 c) only a slight increase of the n-branches due to ALD Al₂O₃ passivation was observed, while for Cr/Au contacted devices, the curve became completely n-type as reported by Helbling et al.. This might either be related to the already oxidized contact areas, or to a different behavior of Pd metal in comparison to the Cr/Au combination. However, also here further investigations to improve the understanding of this effect need to be done.

Device production with reproducible off-state potentials

Figure 4.30 shows a model explaining the result of reproducible off-state potentials. This model is in correlation with the process steps which were applied.

a) The CNFETs were built by contacting **amorphous carbon free SWNTs** via an UV lithography structuring process followed by Pd evaporation and lift-off. This process results in a SiO₂ and SWNT surface which contains photoresist residuals and adsorbed molecules (eg. H₂O, NO₂, O₂, etc.).

b) The photoresist residuals were removed in **NMP at 60°C for 72h**. Only such a long cleaning time allow to remove resist nanoparticles from the surface. Photoresist is a polymer. Polymers in general can have charged or polar functional groups, support molecule adsorption and can up-take water. In the direct vicinity of the SWNT channel these properties can result in an electrical field causing gating effects.

c) Gating effects are well known for polar molecules such as NO_2 or H_2O , as thoroughly discussed in the introduction (section 1.2.1) and theory (section 2.2.2) chapter. The influence of ambient air on the threshold shift is shown in Figure 4.28. The **annealing at 400°C** of the CNFET causes desorption of most molecules from the SWNT and/or SiO_2 surface. Therefore, immediately after annealing, the SWNT is free of molecules that could cause an additional gating to the SWNT.

d) With increasing time **in ambient air, more and more molecules from the air adsorb** on the SWNT surface and/or on the SiO_2 surface and cause the shift of the gate threshold towards more positive potentials. This effect was observed for SGS- and for s-SWNTs. More surprising is the result shown in Figure 4.28 b). From this figure, it can be concluded that the threshold shift is device independent, and that therefore, all devices might have had the same threshold value at time zero immediately after unloading the sample from the annealing oven.

e) This assumption is verified in Figure 4.29. Both SGS- and s-CNFETs show stable off-state potentials in the same region around -0.7V in the case that **ALD Al_2O_3 passivation of the devices is done immediately ($\sim 1\text{min}$) after the annealing procedure**. As already mentioned, due to a slight increase in the n-on-state current after ALD passivation in s-CNFETs, an off-state potential can be determined. This has the advantage that s-CNFETs can be compared with SGS-CNFETs. And indeed, both types of devices have their off-state potential in the same region as shown in the off-state potential distribution of Figure 4.29 c).

In Table 4.3 conditions, which do or do not influence the position of the off-state are summarized.

The conditions which are responsible for an uncontrolled off-state potential shift were discussed above. Interestingly, the mean off-state potential is not at zero, but shifted towards negative potentials as shown in Figure 4.29, while an intrinsic CNFET would have its Fermi level in the middle of the conductance and the valence band. It can be assumed, that this shift is related to the Al_2O_3 -SWNT and SiO_2 -SWNT interface. Oxide are known to have polar or even charged surfaces, which might cause this negative gate potential to the SWNT channels¹⁴. The off-state potential deviation of $\pm 0.33\text{V}$ might result from slight local variations of this effect.

¹⁴ SiO_2 and Al_2O_3 have often hydroxyl (OH) groups on their surfaces, which is an electron donor group.

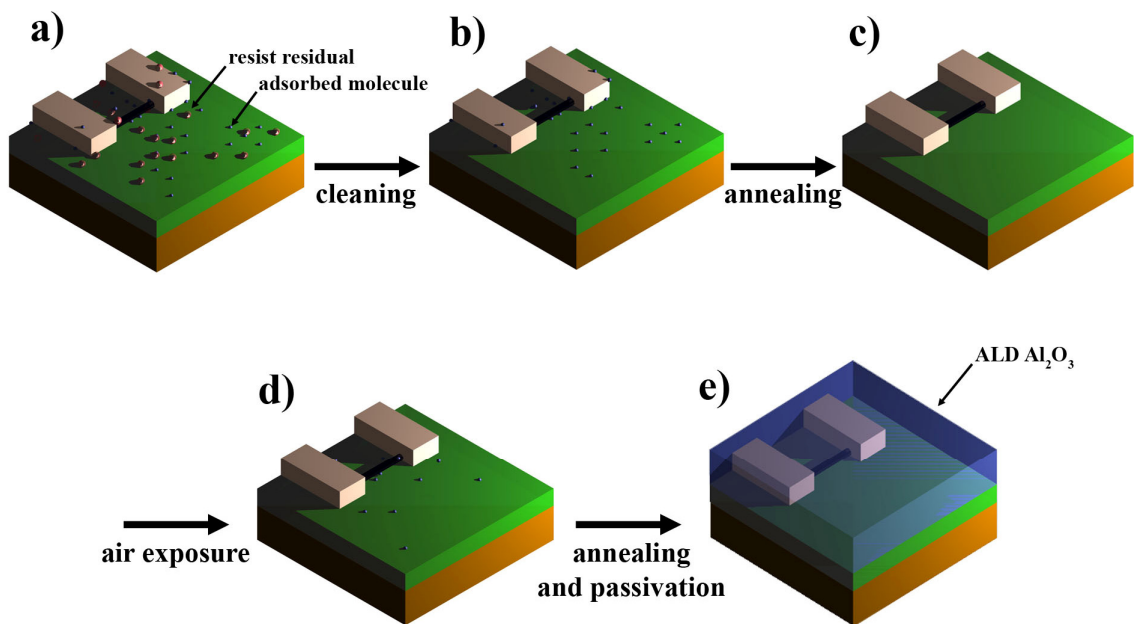


Figure 4.30: Model showing the reason for reproducible off-state potential in CNFETs. A) After the lift-off photoresist nanoparticles remain on the surface, causing additional uncontrolled gating to the CNFET channel. These particles can be removed by cleaning the devices in NMP at 60°C for 72h. b) The remaining gas and vapour molecules, which are well known for their gating effects on CNFETs, were removed by a vacuum annealing at 400°C. d) Exposing the unprotected molecular free devices to air results in a slowly re-adsorption of the gas molecules on the surface of the CNFET channel and on the surface of the gate oxide, which results in an uncontrolled CNFET threshold shift. e) To obtain CNFETs with reproducible and stable off-state potentials the device needs to be covered by a protecting layer for example ALD Al_2O_3 .

Conditions which do not influence the off-state potential are discussed next:

It is known, that the contacts have no influence on the Fermi level shift of a CNFET [133]. The shown gate sweep measurements after ALD passivation confirm this result. Up to a factor of 12 higher device resistances were obtained for s-CNFETs after ALD passivation. Nevertheless, this strong on-state reduction related to the degradation of the contacts has no influence on the off-state potential. In these investigations only SWNTs with diameters around 2nm and narrow diameter distributions were grown. It needs to be tested, whether a SWNT with a much larger band gap influence the position of the Fermi level due to a more dominating Schottky effect. Due to the investigations of Ilani et al. [131] and Heller et al. [133] as discussed in chapter 2.2.2 only a decrease in the sub-threshold slope is expected.

Table 4.3: Conditions which do/do not affect the position of the off-state potential

Influencing the threshold value of a CNFET	Reason	Most probably not influencing the threshold value of a CNFET	Reason
Dirt and resist particles in the direct vicinity of the SWNT channel Gas molecules adsorbed on the SWNT channel and/or on the SiO ₂ surface near the SWNT channel	Charged and polar molecules cause an electrical field and induce therefore a gate threshold shift	CNFET contact quality (needs to be verified)	- According to Heller et al. [133] the quality of the contacts only influences the on-state current - After ALD passivation, the on-state current of some devices were degraded, nevertheless also the off-state potential of these devices occur around -0.7V.
Oxide surface near the SWNT channel	Contain charged and polar surface groups which cause an electrical field and induce therefore a gate threshold shift	Band gap	SGS-SWNTs ($E_g \sim 50\text{meV}$) and s-SWNTs ($E_g \sim 400\text{meV}$ for $\sim 2\text{nm}$). have both their off-state potentials around -0.7V

The investigations shown in Figure 4.29 show, that the size of the band gap for $E_g < 400\text{meV}$ has no significant influence on the off-state potential. Devices consisting of SGS-SWNTs ($E_g \sim 50\text{meV}$) have the same off-state potential as devices consisting of s-SWNTs ($E_g \sim 400\text{meV}$ for $\sim 2\text{nm}$). From this it can be concluded, that it is not necessary to grow SWNTs with controlled type or even chirality for having CNFETs with reproducible off-state potentials. Since the band gap has no influence on the off-state potential, it can be imagined that kinks, bends, crossing SWNTs, bundles, networks, etc. which all have an influence on the band gap, have no influence on the off-state potential, too. Therefore, the integration of a large number of SWNTs might be advantageous in order to increase the signal level, reduce noise and therefore increase the resolution of the CNFET sensors. It still needs to be tested whether it would be possible to measure reproducible (averaged) CNFET gate sweep characteristics integrating many SWNTs in one CNFET.

5 Conclusions and Outlook

The growth of straight, clean, and individual SWNTs with low levels of defects and with controlled density and diameters has been successfully investigated. This success is based on using ferritin-based catalyst nanoparticles and a CVD process which suppresses amorphous carbon formation. The high standard of the SWNTs enabled the fabrication of high quality CNFETs. These devices were used for further investigations into NO₂ gas sensing mechanisms, CNFET-based pressure sensors and CNFET-based quantum dots. The growth of SWNTs with mean diameters around 2nm and diameter distributions below $\pm 0.3\text{nm}$ has been demonstrated, resulting in high quality SWNT metal contacts even in a batch fabrication process.

A new batch integration process based on large-scale compatible UV lithography has been introduced, thus permitting the high yield production of CNFETs that consist of single-bridging individual SWNTs while maintaining the SWNT growth achievements described above. In particular an integration yield of 22% of single-bridging individual SWNTs was reached, equal to around 14 devices per $4 \times 4 \text{mm}^2$ chip.

Based on the new integration process with post annealing and immediate ALD Al₂O₃ protection, the production of CNFETs with reproducible off-state potentials ($m = -0.7V$ $\sigma = \pm 0.33$) was demonstrated.

Synthesis of SWNTs free from amorphous carbon and with low levels of defects

In this field, my predecessor Alain Jungen made an excellent contribution by determining the optimal parameters for the growth of amorphous carbon-free SWNTs [54]. Here these growth parameters were slightly optimized. Further, a change from sputtered catalysts to ferritin-based catalysts resulted in a much less contaminated surface and in the possibility to visualize the catalyst particles by AFM for process optimization. Furthermore, Raman measurements show very small D peaks which indicate that the SWNTs have only low amounts of structural defects.

Synthesis of straight SWNTs

It was determined that the straightness of the SWNTs depends on their diameter. We observed, that SWNTs with diameters below 0.9nm are often curved, while SWNTs with diameters above 0.9nm are mainly straight. To obtain only straight SWNTs the mean SWNT diameter was chosen to be 2nm while the diameter distribution was reduced below 0.5nm by using size separated catalyst nanoparticles. Ferritin proteins were successfully

separated according to the size of the ferrihydrite particle loaded in the protein core by means of sedimentation velocity centrifugation in glycerol media.

Control of the SWNT density

It has been shown that the SWNT density can be controlled by the ferritin concentration in the adsorption solution. Therefore, it is possible to grow any desired SWNT density on the surface by first making a dilution series of a highly concentrated ferritin stock solution.

To facilitate this procedure in future, it might possible to first determine the ferritin concentration in the solution by standard protein concentration assays. However, this would only work when the protein solutions are free from aggregates.

Synthesis of individual SWNTs

It turned out, that bundle formation events are related to the sticking of two or several SWNTs caused by Van-der-Waals forces. Therefore bundle formation was avoided by drastically reducing the SWNT density on the surface to approximately 2 SWNTs in an area of $100\mu\text{m}^2$.

Synthesis of SWNTs with controlled diameters and narrow diameter distributions

The SWNT diameter can be controlled by the size of the catalyst particle. With increasing ferritin loading time the mean diameter of the resulting catalyst particles also increases, resulting in SWNTs with larger diameters. However, as expected [71, 86] the SWNT diameter distribution increases with increasing mean diameter. This undesired effect could be successfully reduced by using size-separated catalyst nanoparticles. With sedimentation velocity centrifugation of ferritin in glycerol media it was possible to separate the proteins by the size of the encapsulated ferrihydrite particles. This new method yielded catalyst nanoparticles with narrow diameter distributions. Using catalyst nanoparticles separated by this method it was possible to grow SWNTs with diameters around 2nm and standard diameter distributions around 0.3nm.

Using these tubes in the batch integration process resulted in state-of-the-art system resistances below 100k Ω .

Decreasing the catalyst mean diameter standard deviation further by improving the particle separation process might not decrease the SWNT diameter distribution due to the effect of catalyst diffusion into the amorphous SiO₂ surface as nicely shown and discussed by Jeong et al [171]. Therefore I recommend establishing SWNT growth on quartz substrates, where this should not occur.

However, the yield from the velocity centrifugation process is low and would need to be optimized for a high-throughput process.

Investigation of a large scale integration process

A new SWNT integration process based on large scale compatible UV lithography was established, with high yields of CNFETs consisting of single-bridging individual SWNTs. This process is based on ferritin adsorption in patterned photoresist holes and placing electrodes on top of these islands after the growth of SWNTs from the ferritin-based catalyst nanoparticles. In this manner, the previous progress in the growth of straight clean

individual SWNTs with low defect densities, controlled diameters, and narrow diameter distributions was upheld. It has been shown that it is possible to control the integration yield by tuning the amount of SWNTs grown from a catalyst growth island through the catalyst density on the surface. The highest integration yield obtained was 22% or 14 CNFETs on a chip area of $4 \times 4 \text{mm}^2$.

This integration process includes a newly developed UV lithography process that results in residual free surfaces on the electrode pad structures after development. This allows the production of CNFETs with high quality contacts and therefore high on-state currents (see also conclusion for SWNT diameter control).

It was possible to produce CNFETs with reproducible device characteristics, in particular having consistent off-state potentials in the same region ($-0.7\text{V} \pm 0.33\text{V}$). This result is an important step towards reproducible production of CNFET sensors. It was shown that this result is mainly based on a cleaning procedure that gives residual free surfaces, followed by an annealing step that desorbs gas molecules from the SWNTs and the subsequent device protection from environmental influences by ALD Al_2O_3 . It has also been shown that the band gap height of the SWNTs has not much influence on the position of the off-state potential (proven for band gaps $< 400 \text{meV}$). Therefore, SWNT type or chirality control might become less important than previously expected.

6 Appendix

6.1 Novel quantitative model based on thermodynamic and kinetic considerations for SWNT growth

A new quantitative model is proposed, which is based on combining thermodynamic considerations similar to the one of Wagg et al. with kinetic considerations similar to the one of Perez-Cabero et al. [152]. This model explains the influence of the growth parameters on the SWNT nucleation and is based on the following assumptions:

The SWNT nucleation step is an irreversible step and can therefore not be expressed by a thermodynamic equilibrium as proposed by Wagg et al. [149]. Moreover, it is assumed that also the carbon formation reaction on the surface, even if the reaction is reversible, does not reach equilibrium.

The SWNT formation process is divided into two parts. First, the formation of carbon atoms at the catalyst surface including chain formation and the formation of the graphene layer on the catalyst and second the formation of 3D higher ordered carbon species in (eg. SWNTs, amorphous carbon or graphite). A major role plays the amount of carbon atoms on the catalyst particles.

Wagg et al. describe that with a thermodynamic parameter “driving force”, which was not defined any further in the publication. This new model includes this thermodynamic energy via the carbon formation kinetics on the catalyst surface. The kinetics of the carbon formation on the catalyst surface defines whether the catalyst is underfed or a SWNT or amorphous carbon is formed, but does not describe the SWNT growth velocity.

The following simplifications were made:

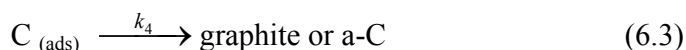
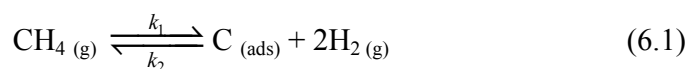
- Dehydrogenation of CH_4 has been reduced to be a one step reaction
- Diffusion of the carbon and the hydrogen atoms on the catalyst surface and into the catalyst was neglected

6.1.1 Determination of the model

The suggested model is based on the assumption that the amount of carbon on the catalyst plays a major role in the nucleation of SWNTs. In the following, the theoretical proof that the carbon atom concentration on the catalyst surface is the main driving force for underfeeding, SWNT nucleation and/or catalyst poisoning will be derived step by step.

Reactions (2.3) to (2.5) show the formation of carbon chains on a catalyst particle. All reactions are reversible except of reaction (2.5), which is assumed to be less reversible (indicated by disproportional arrows for the forward and backward reactions). The next step is the nucleation of higher ordered carbon species (e.g. amorphous carbon, CNTs, graphite, etc.). As soon as a higher ordered carbon species is nucleated it attaches only at its base to the catalyst. For the reverse reaction interaction with the catalyst would be required. The nucleation step is therefore irreversible. This assumption differs from Perez-Cabero et al. [152] and Wagg et al., who were both considering the formation of these carbon species as a reversible reaction step.

With the suggested approach an overall formation reaction of higher carbon species can be divided into the reversible carbon formation reaction on the catalyst surface and the irreversible SWNT, graphitic or amorphous carbon (a-C) formation.



k_1 and k_2 are the kinetic constants of the forward and backward reaction, k_3 and k_4 are the kinetic constants of the SWNT and graphite or amorphous carbon formation, respectively.

It is known that three possible reaction products can be formed on the surface of a small catalyst during CVD growth of SWNTs [98], as shown in Figure 6.1:

1. Dehydrogenated carbon atoms are immediately rehydrogenated and CH_4 is formed (backward reaction of (6.1)). In this particular case the forward reaction velocity is equal or smaller than the backward reaction velocity. Therefore the catalyst is underfed.
2. The nucleation and growth of a SWNT (6.2).

- Amorphous carbon or graphitic carbon is formed on the catalyst surface (6.3), which leads to a deactivation of the catalysis. This is known as poisoning of the catalyst.

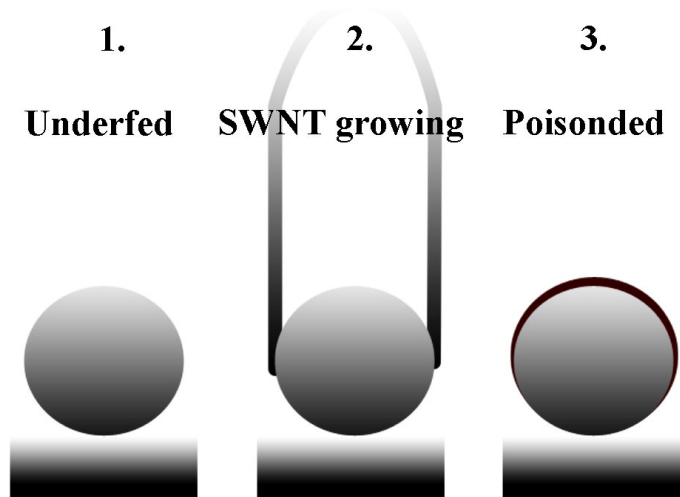


Figure 6.1: The three possible occurrences on a catalyst particle during the CVD process, adapted from [98].

Figure 6.2 shows the reaction coordinates of SWNT and amorphous carbon or graphitic carbon formation, respectively. This diagram is partially adapted from Wagg et al. While they show the whole reaction coordinates of the SWNT graphite and amorphous carbon formation from methane, here only the second part, the formation of these species from dehydrogenated carbon atoms is illustrated. This accentuates the importance of the Gibbs free energy (ΔG) on the formation of the dehydrogenated carbon atoms, which determines whether underfeeding of the catalyst, SWNT nucleation or poisoning of the catalyst takes place, as following described in more detail.

In this diagram the Gibbs free energy (ΔG) for the formation of these products is sketched. On the left side of the reaction coordinate, the formation energy of dehydrogenated carbon atoms is shown. In the middle the nucleation energy for SWNTs and for amorphous or graphitic carbon can be seen and on the right hand side the formation energy of these products is shown.

Of great importance is that the SWNT nucleation is energetically more favorable than amorphous carbon or graphite nucleation¹⁵. In order to enable a reaction, the ΔG of the

¹⁵ This can be determined from simple considerations. The Gibbs free formation energy is defined over the relation $\Delta G = \Delta H - T\Delta S$, where ΔH is the change of the enthalpy and ΔS the change of the entropy. In real crystal nucleation, the entropy plays a major roll. With increased order of structure the entropy decreases. The formation of a nucleus is an event where a higher ordered structure is formed and therefore the entropy decreases drastically. Therefore, the Gibbs nucleation energy is always higher than the Gibbs formation energy. The formation of graphite or amorphous carbon can be considered as real crystal nucleations, because higher ordered structures are formed, while the cap formation of a SWNT is in fact only a release of the already existing structure from the

reactants needs to be higher than the ΔG of the product. In the particular case of SWNT synthesis, ΔG for C_{ads} is higher than ΔG for SWNT nucleation and lower than ΔG for αC nucleation as shown in Figure 6.2.

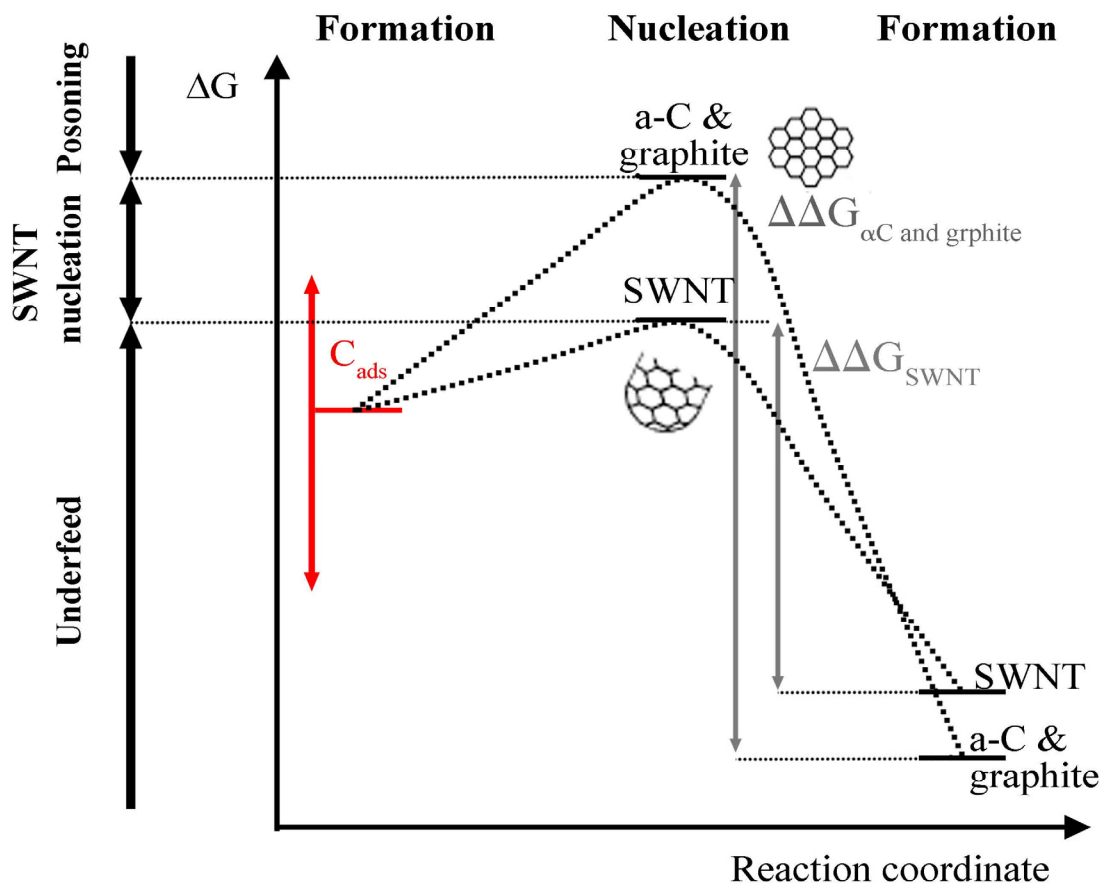


Figure 6.2: Reaction coordinates for the nucleation and formation of SWNTs and amorphous carbon (a-C) or graphite, partially adapted from [149].

From equation (6.1), the Gibbs free formation energy for the carbon formation on the catalyst surface can be determined as:

$$\Delta G_{C_{ads}} = \Delta G_{C_{ads}}^* + RT \ln \frac{p_{H_2}^2 a_C}{p_{CH_4}} \quad (6.4)$$

Where a_c is the activity of pure carbon which can be regarded as the carbon concentration on the particle surface. Assuming constant temperature, H_2 and CH_4 pressures during the reaction, the Gibbs free formation energy is only dependent on the concentration of free carbon on the catalyst. Consequently ΔG increases with increasing amount of carbon on the

catalyst surface (Figure 2.14) and not the formation of a new higher ordered structure. Therefore, the free Gibbs nucleation energy is much lower.

catalyst. Tuning ΔG of the carbon formation reaction (indicated by the arrow in Figure 6.2) leads to the three situations previously mentioned for further reactions:

1. The amount of carbon on the catalyst is low and therefore ΔG of the carbon formation reaction remains below the ΔG of the SWNT nucleation. In that case SWNT nucleation will not take place, nor will graphitic or amorphous carbon nucleate. This is called underfeed of the catalyst.
2. The amount of carbon on the catalyst is moderate and therefore ΔG of the carbon formation reaction exceeds the level of ΔG for SWNT nucleation. The SWNT nucleation occurs faster than the formation of the additional amount of carbon, which would be required to exceed the level of ΔG for amorphous carbon or graphite nucleation. In that case SWNT growth will take place.
3. If the amount of carbon on the catalyst surface increases to a level where nucleation of amorphous or graphitic carbon is enabled, both SWNTs and amorphous or graphitic carbon could theoretically be formed. However, since the formation of amorphous and graphitic carbon is most probably much faster than the nucleation and growth of SWNTs because $\Delta\Delta G_{\alpha C}$ is much larger than $\Delta\Delta G_{\text{SWNT}}$ (see Figure 6.2), catalyst covering by amorphous or graphitic carbon (poisoning) will therefore be the dominant process¹⁶. This procedure might happen in two stages: First during the nucleation (when the ΔG of the carbon formation reaction exceed ΔG of amorphous or graphitic carbon formation faster, than a SWNT nucleus is formed) and second during the growth of SWNTs (when the incorporation of C atoms in the growing structure is slow and therefore the carbon concentration on the catalyst steadily increases).

Consequently it can be assumed that the carbon formation velocity on the catalyst surface has a major impact on the SWNT nucleation and growth. The three reaction pathways can therefore be expressed by the carbon formation velocity at the catalyst as follows:

1. The carbon formation velocity is low \rightarrow underfeeding of the catalyst (no SWNT nucleation)
2. The carbon formation velocity is moderate \rightarrow SWNT nucleation and growth
3. The carbon formation velocity is fast \rightarrow amorphous or graphitic carbon nucleation and formation (poisoning of the catalyst)

¹⁶For picturing this situation lets make a comparison with a dam. At normal weather condition the water pipes from the dam to the power station have enough capacity to transport all the incoming water. At a thunderstorm the incoming water could exceed this capacity causing swamping of the water over the dam.

Analogous, the formation of SWNTs is slow, because there is only one carbon layer formed (1D structure) and all the carbon atoms need to be incorporated into the honeycomb lattice. On the other hand, the formation of for example amorphous carbons can occur more quickly, because the structure is disordered, 3D and the formation energy is lower than the one of a SWNT. When now the amount of incoming carbon atom exceeds the capacity of carbon transport from the catalyst, which is given by the formation and growth of a SWNT, amorphous carbon is formed, which can be regarded as the overflow.

To describe the carbon formation velocity, reaction kinetics of the reaction (6.1) need to be determined. Assuming that the partial pressure of a species i can be expressed as its concentration C_i , the kinetics of reaction (6.1) is defined as:

$$\frac{dC_{CH_4}}{dt} = -\frac{dC_C}{dt} = -2\frac{dC_{H_2}}{dt} \quad (6.5)$$

Where C_{CH_4} is the amount of CH_4 , C_C is the amount of carbon atoms at the catalyst, C_{H_2} is the amount of H_2 and t is the time.

In this particular case we are focusing on the carbon formation velocity on the catalyst, which is determined as:

$$\frac{dC_C}{dt} = k_1 C_{CH_4}(t) - k_2 C_C(t) (C_{H_2}(t))^2 \quad (6.6)$$

with the boundary conditions:

$$C_{CH_4}(t) = C_{CH_4}(0) - x(t) \quad (6.7)$$

$$C_C(t) = C_C(0) + x(t) \quad (6.8)$$

$$C_{H_2}(t) = C_{H_2}(0) + 2x(t) \quad (6.9)$$

Where $C_i(0)$ is the initial concentration of species i and $x(t)$ is the concentration of methane that was transformed within time t .

Substituting the variables of the formula 1.12 with 1.13-1.15 results in

$$\frac{dC_C}{dt} = [k_1 C_{CH_4}(0) - x(t)] - k_2 [C_C(0) + x(t)] [C_{H_2}(0) + 2x(t)]^2 \quad (6.10)$$

This formula shows the dependency of the initial reactant concentrations on the carbon formation velocity. The dependency of the temperature T and activation energy E_a is incorporated into this formula via the kinetic constant k via the Arrhenius equation:

$$k = A e^{-\frac{E_a}{RT}} \quad (6.11)$$

A is the pre-exponential factor or frequency factor which is dependent on the reaction.

With this basic model the influence of the different parameters on the SWNT nucleation and growth can be explained.

6.1.2 Discussion

Influence of the temperature

Considering the reaction kinetics, the temperature directly influences the kinetic constant described by the Arrhenius equation (6.11). An increase in the temperature by 10°C increases the kinetic constant by a factor of 2 to 3, which means that the carbon formation process on the catalyst surface becomes faster.

Influence of the partial pressures of CH₄ and H₂

From equation (6.10) it can be determined that an increase of the initial CH₄ partial pressure increases the carbon formation velocity on the catalyst. On the other hand, an increase in the H₂ partial pressure decreases the carbon formation velocity.

Influence of the catalyst strength and diameter

The influence of the catalyst is more complex. On one hand, the strength of the catalyst determines the reduction of the activation energy E_a which incorporates Arrhenius equation (6.11). With increasing catalyst strength E_a decreases to a larger extent, and therefore the carbon formation velocity increases.

However, the binding energy of the formed graphene layer to the catalyst and the size of the catalyst particle play an important role as well. Ding et al. [174] showed by molecular dynamics simulations that the binding energy to the catalyst defines whether a growing SWNT remains at the catalyst surface or terminates due to cap formation at the catalyst site. Therefore, catalysts like Ni, Fe and Co, with a high binding affinity to carbon, are favored over catalysts like Au, Cu, Pd and Pt.

Lu et al. [98] observed that with increasing CH₄ partial pressure, while maintaining the H₂ partial pressure constant, larger particles became more active and smaller particles became less active for SWNT nucleation. Similar observations were made by Cheung et al. [86] and Javey et al. [148] for increasing the reaction temperature.

Lu et al. explained this phenomenon as shown in Figure 6.3. At lower temperatures or CH₄ pressures, smaller particles are active, while larger particles do not have enough carbon on their surface for nucleation. At higher temperatures or CH₄ pressures, smaller particles are already poisoned while the larger particles become active.

Considering the determined model, it can be assumed that due to the lower surface to volume ratio of larger particles the carbon concentration on the catalyst surface increases slower than it does on smaller catalysts with higher surface to volume ratios under the same reaction conditions. Therefore, the activity for SWNT nucleation with increasing CH₄ partial pressure, increasing temperature or decreasing H₂ partial pressure shifts towards larger particles.

Additionally, it might be possible that smaller catalyst particles are catalytically more active than the larger catalyst particles. This phenomenon, known as catalyst size effect [175], again results in faster carbon formation defined by the Arrhenius equation (6.11).

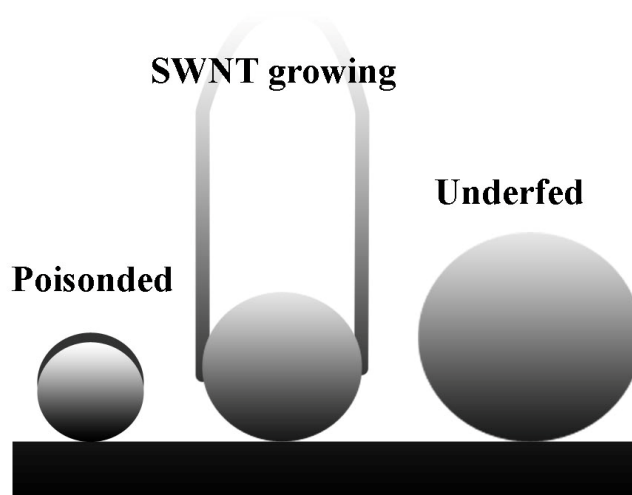


Figure 6.3: Schematics showing the catalyst size dependency of the SWNT nucleation, adapted from [98].

Influence of the catalyst support

The support surface has influence on the growing process due to physical and chemical interactions between the catalyst particles and the support surface [21]. Physical interactions, for example electrostatic forces and Van-der-Waals forces, or the surface roughness of the support surface decrease the thermally driven diffusion and the movement of the particle on the support surface. A surface can either act as Lewis acid, as Lewis base or neutral. A Lewis acid is an electron acceptor and a Lewis base an electron donor. Therefore, depending on the catalyst support surface, the electron density on the catalyst particle is varied, which leads to a variation in the catalytic activity, hence to a change of the carbon formation rate on the catalyst surface. A reduction of the electronic configuration of nanoparticles increases the decomposition rate of the catalyst [176-177].

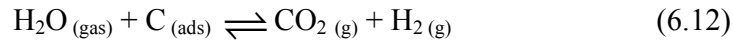
Influence of the type of reaction gas

Acetylene has a C-C triple bond containing more energy than the σ -bonds in methane, and is therefore higher energetic than methane (see Table 6.1). Therefore, acetylene provides a higher carbon formation velocity than methane and can be used for low temperature CVD growth (400-700°C).

Table 6.1: Free Gibbs standard formation energies for different carbon sources [178]

Molecule	Free Gibbs standard formation energy (ΔG^*) ($\text{JK}^{-1}\text{mol}^{-1}$)
Methane CH_4	-50
Acetylene C_2H_2	209
Ethylene C_2H_4	60
Ethan C_2H_6	-32
Carbon monoxide CO	-32
Ethanol $\text{C}_2\text{H}_5\text{OH}$	-168
Methanol CH_3OH	-166

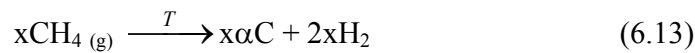
The use of alcohols, carbon monoxide or the addition of water is known to result in clean and ultra long SWNTs. Using these gases, an additional reaction resulting in a decreased carbon concentration at the catalyst surface has to be considered, here explained by the addition of water to the reaction gases.



Oxygen is known to be a strong reactant which steadily helps to reduce the carbon concentration at the catalyst particle.

Amorphous carbon formation by pyrolysis

Amorphous carbon can also be formed in the absence of the catalyst by pyrolysis according to the following reaction:



Amorphous carbon formed by pyrolysis is the main reason for SWNT contamination. In this reaction the temperature, the partial pressure of CH_4 and the partial pressure of H_2 are of high importance. Reducing the H_2 partial pressure and increasing the CH_4 partial pressure and the temperature will shift the reaction equilibrium towards the product side, which leads to enhanced amorphous carbon formation. This effect was shown experimentally in our group by Jungen et al. [54].

6.1.3 Conclusion

A new qualitative model to understand the influences of the growth parameters on the SWNT nucleation and catalyst poisoning based on the combination of thermodynamic and kinetic considerations was determined. In particular, in this model the Gibbs free energy of the carbon dehydrogenation reaction on the catalyst surface is influenced by the amount of carbon atoms on the surface, which on its share is mainly influenced by the velocity of the carbon formation on the catalyst described over the carbon formation kinetics.

In conclusion, the expected SWNT nucleation yield on catalyst nanoparticles with monodispersed size in dependence of the CH_4 and H_2 partial pressures, the temperature and the catalyst strength according to the determined model is sketched in Figure 6.4. With increasing CH_4 partial pressure, temperature and catalyst strength and with decreasing H_2 partial pressure, the SWNT nucleation yield increases until the poisoning becomes dominant, leading to a decrease of the SWNT nucleation yield. Additionally, the increase of these parameters and the decrease of the H_2 pressure lead to an increasing amount of amorphous carbon deposition on the sample and SWNT surface due to pyrolysis of CH_4 .

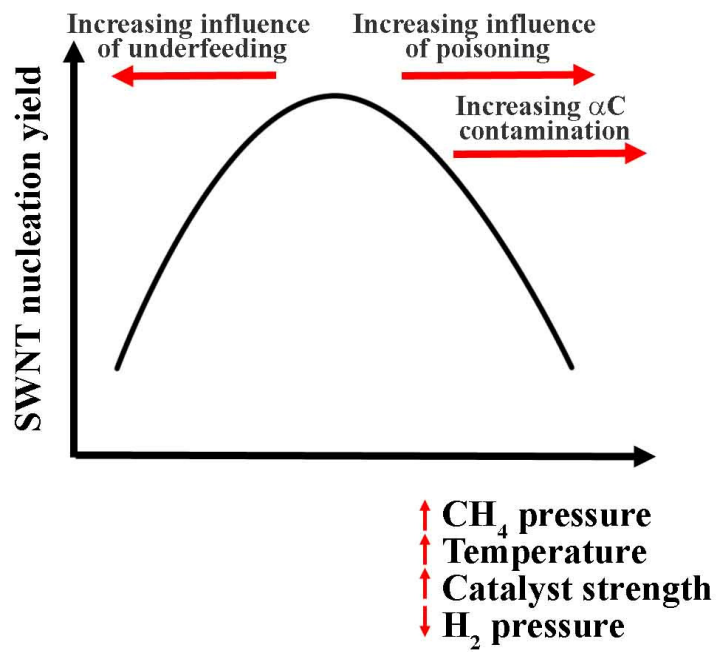


Figure 6.4: Sketch of the expected SWNT nucleation yield in dependence of different growth parameters according to the new determined nucleation model.

Bibliography

- [1] M. Reibold, P. Paufler, A. A. Levin, W. Kochmann, N. Patzke, and D. C. Meyer, "Materials - Carbon nanotubes in an ancient Damascus sabre," *Nature*, vol. 444, pp. 286-286, 2006.
- [2] R. Saito, G. Dresselhaus, and M. S. Dresselhaus, *Physical Properties of carbon nanotubes* London: Imperial College Press, 1998.
- [3] S. Iijima, "Helical Microtubules of Graphitic Carbon," *Nature*, vol. 354, pp. 56-58, Nov 1991.
- [4] S. Iijima and T. Ichihashi, "Single-Shell Carbon Nanotubes of 1-Nm Diameter," *Nature*, vol. 363, pp. 603-605, 1993.
- [5] D. S. Bethune, C. H. Kiang, M. S. Devries, G. Gorman, R. Savoy, J. Vazquez, and R. Beyers, "Cobalt-Catalyzed Growth of Carbon Nanotubes with Single-Atomic-Layerwalls," *Nature*, vol. 363, pp. 605-607, Jun 1993.
- [6] T. Helbling, S. Drittenbass, L. Durrer, C. Roman, and C. Hierold, "Ultra small single walled carbon nanotube pressure sensors " in *22nd IEEE International Conference on Micro Electro Mechanical Systems*, Sorrento, 2009.
- [7] C. Stampfer, A. Jungen, R. Linderman, D. Obergfell, S. Roth, and C. Hierold, "Nano-electromechanical displacement sensing based on single-walled carbon nanotubes," *Nano Letters*, vol. 6, pp. 1449-1453, Jul 2006.
- [8] V. N. Popov, "Carbon nanotubes: properties and application," *Materials Science & Engineering R-Reports*, vol. 43, pp. 61-102, Jan 2004.
- [9] E. Dervishi, Z. R. Li, Y. Xu, V. Saini, A. R. Biris, D. Lupu, and A. S. Biris, "Carbon Nanotubes: Synthesis, Properties, and Applications," *Particulate Science and Technology*, vol. 27, pp. 107-125, 2009.
- [10] Q. W. Li, C. H. Liu, X. S. Wang, and S. S. Fan, "Measuring the thermal conductivity of individual carbon nanotubes by the Raman shift method," *Nanotechnology*, vol. 20, p. 5, Apr 2009.
- [11] D. R. Lide, *Thermal Conductivity of Metals and Semiconductors as a Function of Temperature in the CRC Handbook of Chemistry and Physics*, 87 ed., 2003.

-
- [12] Z. Yao, C. L. Kane, and C. Dekker, "High-field electrical transport in single-wall carbon nanotubes," *Physical Review Letters*, vol. 84, pp. 2941-2944, 2000.
- [13] B. Q. Wei, R. Vajtai, and P. M. Ajayan, "Reliability and current carrying capacity of carbon nanotubes," *Applied Physics Letters*, vol. 79, pp. 1172-1174, 2001.
- [14] C. Wang, Y. J. Hu, C. M. Lieber, and S. H. Sun, "Ultrathin Au nanowires and their transport properties," *Journal of the American Chemical Society*, vol. 130, pp. 8902-+, 2008.
- [15] M. Dresselhaus, G. Dresselhaus, and G. Avouris, *Carbon Nanotubes: Synthesis, Structure, Properties and Application*. Berlin: Springer, 2001.
- [16] C. G. Hu, C. L. Cao, Y. F. Xiong, X. Y. Han, Y. Xi, and J. Miao, "Temperature dependent piezoresistive effect of multi-walled carbon nanotube films," *Diamond and Related Materials*, vol. 16, pp. 388-392, 02 2007.
- [17] C. Hierold, O. Brand, G. K. Fedder, J. G. Korvink, and O. Tabata, *Advanced Micro & Nanosystems*. Weinheim: WILEY-VCH 2008.
- [18] W. I. Milne, K. B. K. Teo, G. A. J. Amaratunga, P. Legagneux, L. Gangloff, J. P. Schnell, V. Semet, V. T. Binh, and O. Groening, "Carbon nanotubes as field emission sources," *Journal of Materials Chemistry*, vol. 14, pp. 933-943, 2004.
- [19] A. P. Graham, G. S. Duesberg, W. Hoenlein, F. Kreupl, M. Liebau, R. Martin, B. Rajasekharan, W. Pamler, R. Seidel, W. Steinhögl, and E. Unger, "How do carbon nanotubes fit into the semiconductor roadmap?," *Applied Physics a-Materials Science & Processing*, vol. 80, pp. 1141-1151, 2005.
- [20] Z. H. Chen, J. Appenzeller, Y. M. Lin, J. Sippel-Oakley, A. G. Rinzler, J. Y. Tang, S. J. Wind, P. M. Solomon, and P. Avouris, "An integrated logic circuit assembled on a single carbon nanotube," *Science*, vol. 311, pp. 1735-1735, Mar 2006.
- [21] H. J. Dai, "Carbon nanotubes: Synthesis, integration, and properties," *Accounts of Chemical Research*, vol. 35, pp. 1035-1044, Dec 2002.
- [22] S. N. Kim, J. F. Rusling, and F. Papadimitrakopoulos, "Carbon nanotubes for electronic and electrochemical detection of biomolecules," *Advanced Materials*, vol. 19, pp. 3214-3228, Oct 2007.
- [23] C. Hierold, "Concepts for carbon nanotube sensors," in *TRANSDUCERS '07 & Eurosensors XXI. 2007 14th International Conference on Solid-State Sensors, Actuators and Microsystems*, Lyon, France, 2007, pp. 5-10.
- [24] "Nanotube bike enters Tour de France," *nanotechweb.org*, p. <http://nanotechweb.org/cws/article/tech/22597>, 2005.
-

- [25] W. Göpel, J. Hesse, and Z. J.N., Eds., *Sensors A Coprehensive Survey* (Fundamentals and General Aspects. Weinheim: VCH, 1989, p.^pp. Pages.
- [26] W. Göpel, J. Hesse, and J. N. Zemel, Eds., *Sensors a Coprehensive Survey* (Micro- and Nanosensor Technology/Trends in Sensor Markets. Weinheim: VCH, 1995, p.^pp. Pages.
- [27] J. Kong, N. R. Franklin, C. Zhou, M. G. Chapline, S. Peng, K. Cho, and H. Dai, "Nanotube Molecular Wires as Chemical Sensors," *Science*, vol. 287, pp. 622-625, January 28, 2000 2000.
- [28] M. Mattmann, T. Helbling, L. Durrer, C. Roman, C. Hierold, R. Pohle, and M. Fleischer, "Sub-ppm NO₂ detection by Al₂O₃ contact passivated carbon nanotubes FETs," *Applied Physics Letters*, vol. 94, p. 183502, 2009.
- [29] T. Helbling, C. Hierold, C. Roman, L. Durrer, M. Mattmann, and V. M. Bright, "Long term investigations of carbon nanotube transistors encapsulated by atomic-layer-deposited Al₂O₃ for sensor applications," *Nanotechnology*, vol. 20, 2009.
- [30] T. Helbling, R. Pohle, L. Durrer, C. Stampfer, C. Roman, A. Jungen, M. Fleischer, and C. Hierold, "Sensing NO₂ with individual suspended single-walled carbon nanotubes," *Sensors & Actuators: B. Chemical*, vol. 132, pp. 491-497, 2008.
- [31] T. Helbling, C. Hierold, L. Durrer, C. Roman, R. Grundbacher, R. Pohle, and M. Fleischer, "Suspended and non-suspended carbon nanotube transistors for NO₂ sensing - A qualitative comparison," *physica status SolidiB*, vol. accepted, 2008.
- [32] N. Sinha, J. Z. Ma, and J. T. W. Yeow, "Carbon nanotube-based sensors," *Journal of Nanoscience and Nanotechnology*, vol. 6, pp. 573-590, Mar 2006.
- [33] D. W. Park, Y. H. Kim, B. S. Kim, H. M. So, K. Won, J. O. Lee, K. J. Kong, and H. Chang, "Detection of tumor markers using single-walled carbon nanotube field effect transistors," *Journal of Nanoscience and Nanotechnology*, vol. 6, pp. 3499-3502, Nov 2006.
- [34] T. W. Tomblor, C. W. Zhou, L. Alexseyev, J. Kong, H. J. Dai, L. Lei, C. S. Jayanthi, M. J. Tang, and S. Y. Wu, "Reversible electromechanical characteristics of carbon nanotubes under local-probe manipulation," *Nature*, vol. 405, pp. 769-772, 2000.
- [35] C. Stampfer, T. Helbling, D. Obergfell, B. Schoberle, M. K. Tripp, A. Jungen, S. Roth, V. M. Bright, and C. Hierold, "Fabrication of single-walled carbon-nanotube-based pressure sensors," *Nano Letters*, vol. 6, pp. 233-237, Feb 2006.

-
- [36] C. Stampfer, T. Helbling, A. Jungen, and C. Hierold, "Micromachined pressure sensors for electromechanical characterization of carbon nanotubes," *Physica Status Solidi B-Basic Solid State Physics*, vol. 243, pp. 3537-3541, Nov 2006.
- [37] P. Delaney, H. J. Choi, J. Ihm, S. G. Louie, and M. L. Cohen, "Broken symmetry and pseudogaps in ropes of carbon nanotubes," *Nature*, vol. 391, pp. 466-468, 1998.
- [38] R. J. Grow, Q. Wang, J. Cao, D. W. Wang, and H. J. Dai, "Piezoresistance of carbon nanotubes on deformable thin-film membranes," *Applied Physics Letters*, vol. 86, 2005.
- [39] M. Meyyappan, *Carbon Nanotubes Science and Applications*. New York: CRC Press.
- [40] Y. M. Li, D. Mann, M. Rolandi, W. Kim, A. Ural, S. Hung, A. Javey, J. Cao, D. W. Wang, E. Yenilmez, Q. Wang, J. F. Gibbons, Y. Nishi, and H. J. Dai, "Preferential growth of semiconducting single-walled carbon nanotubes by a plasma enhanced CVD method," *Nano Letters*, vol. 4, pp. 317-321, Feb 2004.
- [41] S. Suzuki, J. I. Hashimoto, T. Ogino, and Y. Kobayashi, "Electric property control of carbon nanotubes by defects," in *International Conference on Solid State Devices and Materials*, Tsukuba, JAPAN, 2007, pp. 3292-3295.
- [42] C. L. Kane and E. J. Mele, "Size, shape, and low energy electronic structure of carbon nanotubes," *Physical Review Letters*, vol. 78, pp. 1932-1935, 1997.
- [43] Personal communication with Prof. Jörg Appenzeller, Purdue University
- [44] J. M. Cowley, P. Nikolaev, A. Thess, and R. E. Smalley, "Electron nano-diffraction study of carbon single-walled nanotube ropes," *Chemical Physics Letters*, vol. 265, pp. 379-384, 1997.
- [45] L. Ding, A. Tselev, J. Y. Wang, D. N. Yuan, H. B. Chu, T. P. McNicholas, Y. Li, and J. Liu, "Selective Growth of Well-Aligned Semiconducting Single-Walled Carbon Nanotubes," *Nano Letters*, vol. 9, pp. 800-805, Feb 2009.
- [46] X. L. Liu, S. Han, and C. W. Zhou, "Novel nanotube-on-insulator (NOI) approach toward single-walled carbon nanotube devices," *Nano Letters*, vol. 6, pp. 34-39, Jan 2006.
- [47] S. J. Kang, C. Kocabas, T. Ozel, M. Shim, N. Pimparkar, M. A. Alam, S. V. Rotkin, and J. A. Rogers, "High-performance electronics using dense, perfectly aligned arrays of single-walled carbon nanotubes," *Nature Nanotechnology*, vol. 2, pp. 230-236, Apr 2007.
-

- [48] S. Lastella, G. Mallick, R. Woo, S. P. Karna, D. A. Rider, I. Manners, Y. J. Jung, C. Y. Ryu, and P. M. Ajayan, "Parallel arrays of individually addressable single-walled carbon nanotube field-effect transistors," *Journal of Applied Physics*, vol. 99, p. 4, Jan 2006.
- [49] Z. H. Chen, J. Appenzeller, J. Knoch, Y. M. Lin, and P. Avouris, "The role of metal-nanotube contact in the performance of carbon nanotube field-effect transistors," *Nano Letters*, vol. 5, pp. 1497-1502, Jul 2005.
- [50] J. Appenzeller, J. Knoch, M. I. Bjork, H. Riel, H. Schmid, and W. Riess, "Toward Nanowire Electronics," *Ieee Transactions on Electron Devices*, vol. 55, pp. 2827-2845, 2008.
- [51] J. Appenzeller, "Carbon nanotubes for high-performance electronics - Progress and prospect," *Proceedings of the Ieee*, vol. 96, pp. 201-211, Feb 2008.
- [52] W. Kim, A. Javey, R. Tu, J. Cao, Q. Wang, and H. J. Dai, "Electrical contacts to carbon nanotubes down to 1 nm in diameter," *Applied Physics Letters*, vol. 87, p. 173101, Oct 2005.
- [53] H. J. Dai, A. Javey, E. Pop, D. Mann, W. Kim, and Y. R. Lu, "Electrical transport properties and field effect transistors of carbon nanotubes," *Nano*, vol. 1, pp. 1-13, Jul 2006.
- [54] A. Jungen, C. Stampfer, L. Durrer, T. Helbling, and C. Hierold. (2007, Feb). Amorphous carbon contamination monitoring and process optimization for single-walled carbon nanotube integration. *Nanotechnology 18(7)*, 075603. Available: <Go to ISI>://000243874200010
- [55] A. Thess, R. Lee, P. Nikolaev, H. J. Dai, P. Petit, J. Robert, C. H. Xu, Y. H. Lee, S. G. Kim, A. G. Rinzler, D. T. Colbert, G. E. Scuseria, D. Tomanek, J. E. Fischer, and R. E. Smalley, "Crystalline ropes of metallic carbon nanotubes," *Science*, vol. 273, pp. 483-487, Jul 1996.
- [56] H. Dai, A. G. Rinzler, P. Nikolaev, A. Thess, D. T. Colbert, and R. E. Smalley, "Single-wall nanotubes produced by metal-catalyzed disproportionation of carbon monoxide," *Chemical Physics Letters*, vol. 260, pp. 471-475, 27 September 1996.
- [57] E. Flahaut, A. Govindaraj, A. Peigney, C. Laurent, A. Rousset, and C. N. R. Rao, "Synthesis of single-walled carbon nanotubes using binary (Fe, Co, Ni) alloy nanoparticles prepared in situ by the reduction of oxide solid solutions," *Chemical Physics Letters*, vol. 300, pp. 236-242, 1999.
- [58] A. M. Cassell, J. A. Raymakers, J. Kong, and H. J. Dai, "Large scale CVD synthesis of single-walled carbon nanotubes," *Journal of Physical Chemistry B*, vol. 103, pp. 6484-6492, Aug 1999.

- [59] H. M. Cheng, F. Li, G. Su, H. Y. Pan, L. L. He, X. Sun, and M. S. Dresselhaus, "Large-scale and low-cost synthesis of single-walled carbon nanotubes by the catalytic pyrolysis of hydrocarbons," *Applied Physics Letters*, vol. 72, pp. 3282-3284, Jun 1998.
- [60] K. Hata, D. N. Futaba, K. Mizuno, T. Namai, M. Yumura, and S. Iijima, "Water-assisted highly efficient synthesis of impurity-free single-walled carbon nanotubes," *Science*, vol. 306, pp. 1362-1364, 2004.
- [61] Y. Murakami, Y. Miyauchi, S. Chiashi, and S. Maruyama, "Characterization of single-walled carbon nanotubes catalytically synthesized from alcohol," *Chemical Physics Letters*, vol. 374, pp. 53-58, 2003.
- [62] M. Monthieux, B. W. Smith, B. Bouteaux, A. Claye, J. E. Fischer, and D. E. Luzzi, "Sensitivity of single-wall carbon nanotubes to chemical processing: an electron microscopy investigation," *Carbon*, vol. 39, pp. 1251-1272, 2001.
- [63] O. Zhou, H. Shimoda, B. Gao, S. J. Oh, L. Fleming, and G. Z. Yue, "Materials science of carbon nanotubes: Fabrication, integration, and properties of macroscopic structures of carbon nanotubes," *Accounts of Chemical Research*, vol. 35, pp. 1045-1053, Dec 2002.
- [64] R. Krupke, F. Hennrich, H. von Lohneysen, and M. M. Kappes, "Separation of metallic from semiconducting single-walled carbon nanotubes," *Science*, vol. 301, pp. 344-347, 2003.
- [65] M. C. Hersam, "Progress towards monodisperse single-walled carbon nanotubes," *Nature Nanotechnology*, vol. 3, pp. 387-394, Jul 2008.
- [66] M. S. Arnold, A. A. Green, J. F. Hulvat, S. I. Stupp, and M. C. Hersam, "Sorting carbon nanotubes by electronic structure using density differentiation," *Nature Nanotechnology*, vol. 1, pp. 60-65, 2006.
- [67] P. C. Collins, M. S. Arnold, and P. Avouris, "Engineering carbon nanotubes and nanotube circuits using electrical breakdown," *Science*, vol. 292, pp. 706-709, 2001.
- [68] S. Suzuki, J. I. Hashimoto, T. Ogino, and Y. Kobayashi, "Electric property control of carbon nanotubes by defects," *Japanese Journal of Applied Physics*, vol. 47, pp. 3292-3295, Apr 2008.
- [69] L. T. Qu, F. Du, and L. M. Dai, "Preferential syntheses of semiconducting vertically aligned single-walled carbon nanotubes for direct use in FETs," *Nano Letters*, vol. 8, pp. 2682-2687, Sep 2008.
-

- [70] Y. Qian, S. M. Huang, F. L. Gao, Q. R. Cai, L. J. Zhang, and W. B. Hu, "Superlong-oriented Single-Walled Carbon Nanotube Arrays on Substrate with Low Percentage of Metallic Structure," *Journal of Physical Chemistry C*, vol. 113, pp. 6983-6988, 2009.
- [71] Y. M. Li, W. Kim, Y. G. Zhang, M. Rolandi, D. W. Wang, and H. J. Dai, "Growth of single-walled carbon nanotubes from discrete catalytic nanoparticles of various sizes," *Journal of Physical Chemistry B*, vol. 105, pp. 11424-11431, Nov 2001.
- [72] A. Ismach, L. Segev, E. Wachtel, and E. Joselevich, "Atomic-step-templated formation of single wall carbon nanotube patterns," *Angewandte Chemie-International Edition*, vol. 43, pp. 6140-6143, 2004.
- [73] A. Ismach, D. Kantorovich, and E. Joselevich, "Carbon nanotube graphoepitaxy: Highly oriented growth by faceted nanosteps," *Journal of the American Chemical Society*, vol. 127, pp. 11554-11555, Aug 2005.
- [74] J. Kong, A. M. Cassell, and H. J. Dai, "Chemical vapor deposition of methane for single-walled carbon nanotubes," *Chemical Physics Letters*, vol. 292, pp. 567-574, 1998.
- [75] J. Kong, H. T. Soh, A. M. Cassell, C. F. Quate, and H. J. Dai, "Synthesis of individual single-walled carbon nanotubes on patterned silicon wafers," *Nature*, vol. 395, pp. 878-881, Oct 1998.
- [76] M. S. Strano, V. C. Moore, M. K. Miller, M. J. Allen, E. H. Haroz, C. Kittrell, R. H. Hauge, and R. E. Smalley, "The role of surfactant adsorption during ultrasonication in the dispersion of single-walled carbon nanotubes," *Journal of Nanoscience and Nanotechnology*, vol. 3, pp. 81-86, Feb-Apr 2003.
- [77] Y. Tu, Z. P. Huang, D. Z. Wang, J. G. Wen, and Z. F. Ren, "Growth of aligned carbon nanotubes with controlled site density," *Applied Physics Letters*, vol. 80, pp. 4018-4020, May 2002.
- [78] S. M. Huang, X. Y. Cai, C. S. Du, and J. Liu, "Oriented long single walled carbon nanotubes on substrates from floating catalysts," *Journal of Physical Chemistry B*, vol. 107, pp. 13251-13254, Dec 2003.
- [79] O. A. Nerushev, R. E. Morjan, D. I. Ostrovskii, M. Sveningsson, M. Jonsson, F. Rohmund, and E. E. B. Campbell, "The temperature dependence of Fe-catalysed growth of carbon nanotubes on silicon substrates," *Physica B-Condensed Matter*, vol. 323, pp. 51-59, Oct 2002.
- [80] Q. Fu, S. M. Huang, and J. Liu, "Chemical vapor depositions of single-walled carbon nanotubes catalyzed by uniform Fe₂O₃ nanoclusters synthesized using

-
- diblock copolymer micelles," *Journal of Physical Chemistry B*, vol. 108, pp. 6124-6129, 2004.
- [81] G. H. Jeong, S. Suzuki, Y. Kobayashi, A. Yamazaki, H. Yoshimura, and Y. Homma, "Effect of nanoparticle density on narrow diameter distribution of carbon nanotubes and particle evolution during chemical vapor deposition growth," *Journal of Applied Physics*, vol. 98, Dec 2005.
- [82] L. Delzeit, B. Chen, A. Cassell, R. Stevens, C. Nguyen, and M. Meyyappan, "Multilayered metal catalysts for controlling the density of single-walled carbon nanotube growth," *Chemical Physics Letters*, vol. 348, pp. 368-374, Nov 2001.
- [83] A. Iaia, L. Marty, C. Naud, V. Bouchiat, A. Loiseau, E. Di Muoio, T. Fournier, and A. M. Bonnot, "Oriented growth of suspended single wall carbon nanotube by Hot Filament CVD," *Thin Solid Films*, vol. 501, pp. 221-223, Apr 2006.
- [84] A. Javey and H. J. Dai, "Regular arrays of 2 nm metal nanoparticles for deterministic synthesis of nanomaterials," *Journal of the American Chemical Society*, vol. 127, pp. 11942-11943, Aug 2005.
- [85] C. Stampfer, A. Jungen, T. Helbling, L. Durrer, and C. Hierold, "Electromechanical transducers based on single-walled carbon nanotubes," *Proceedings of the SPIE - The International Society for Optical Engineering*, p. 70370E (8 pp.), 2008.
- [86] C. L. Cheung, A. Kurtz, H. Park, and C. M. Lieber, "Diameter-controlled synthesis of carbon nanotubes," *Journal of Physical Chemistry B*, vol. 106, pp. 2429-2433, Mar 2002.
- [87] G. H. Jeong, A. Yamazaki, S. Suzuki, H. Yoshimura, Y. Kobayashi, and Y. Homma, "Production of single-walled carbon nanotubes with narrow diameter distribution using iron nanoparticles derived from DNA-binding proteins from starved cells," *Carbon*, vol. 45, pp. 978-983, 2007.
- [88] M. Ishida, H. Hongo, F. Nihey, and Y. Ochiai, "Diameter-controlled carbon nanotubes grown from lithographically defined nanoparticles," *Japanese Journal of Applied Physics Part 2-Letters & Express Letters*, vol. 43, pp. L1356-L1358, Oct 2004.
- [89] H. C. Choi, W. Kim, D. W. Wang, and H. J. Dai, "Delivery of catalytic metal species onto surfaces with dendrimer carriers for the synthesis of carbon nanotubes with narrow diameter distribution," *Journal of Physical Chemistry B*, vol. 106, pp. 12361-12365, Dec 2002.
-

Bibliography

- [90] M. F. Zhang, M. Yudasaka, and S. Iijima, "Production of large-diameter single-wall carbon nanotubes by adding Fe to a NiCo catalyst in laser ablation," *Journal of Physical Chemistry B*, vol. 108, pp. 12757-12762, Aug 2004.
- [91] J. F. Geng, H. W. Li, D. J. Zhou, W. T. S. Huck, and B. F. G. Johnson, "A dendrimer-based Co-32 nanocluster: Synthesis and application in diameter-controlled growth of single-walled carbon nanotubes," *Polyhedron*, vol. 25, pp. 585-590, Jan 2006.
- [92] D. Ogrin, R. Colorado, B. Maruyama, M. J. Pender, R. E. Smalley, and A. R. Barron, "Single-walled carbon nanotube growth using $[\text{Fe-3}(\mu(3)\text{-O})(\mu\text{-O2CR})(6)(\text{L})(3)](n+)$ complexes as catalyst precursors," *Dalton Transactions*, pp. 229-236, 2006.
- [93] R. M. Kramer, L. A. Sowards, M. J. Pender, M. O. Stone, and R. R. Naik, "Constrained iron catalysts for single-walled carbon nanotube growth," *Langmuir*, vol. 21, pp. 8466-8470, Aug 2005.
- [94] P. Nikolaev, M. J. Bronikowski, R. K. Bradley, F. Rohmund, D. T. Colbert, K. A. Smith, and R. E. Smalley, "Gas-phase catalytic growth of single-walled carbon nanotubes from carbon monoxide," *Chemical Physics Letters*, vol. 313, pp. 91-97, 1999.
- [95] A. G. Nasibulin, P. V. Pikhitsa, H. Jiang, and E. I. Kauppinen, "Correlation between catalyst particle and single-walled carbon nanotube diameters," *Carbon*, vol. 43, pp. 2251-2257, Sep 2005.
- [96] L. Durrer, T. Helbling, C. Zenger, A. Jungen, C. Stampfer, and C. Hierold, "SWNT growth by CVD on Ferritin-based iron catalyst nanoparticles towards CNT sensors," *Sensors & Actuators: B. Chemical*, vol. 132, pp. 485-490, 2008.
- [97] P. B. Amama, M. R. Maschmann, T. S. Fisher, and T. D. Sands, "Dendrimer-templated Fe nanoparticles for the growth of single-wall carbon nanotubes by plasma-enhanced CVD," *Journal of Physical Chemistry B*, vol. 110, pp. 10636-10644, Jun 2006.
- [98] C. G. Lu and J. Liu, "Controlling the diameter of carbon nanotubes in chemical vapor deposition method by carbon feeding," *Journal of Physical Chemistry B*, vol. 110, pp. 20254-20257, Oct 2006.
- [99] A. Vijayaraghavan, S. Blatt, D. Weissenberger, M. Oron-Carl, F. Hennrich, D. Gerthsen, H. Hahn, and R. Krupke, "Ultra-large-scale directed assembly of single-walled carbon nanotube devices," *Nano Letters*, vol. 7, pp. 1556-1560, Jun 2007.
- [100] B. R. Burg, J. Schneider, M. Muoth, L. Durrer, T. Helbling, N. C. Schirmer, T. Schwamb, C. Hierold, and D. Poulikakos, "Aqueous Dispersion and

-
- Dielectrophoretic Assembly of Individual Surface-Synthesized Single-Walled Carbon Nanotubes," *Langmuir*, vol. 25, pp. 7778-7782, 2009.
- [101] L. Rispal and U. Schwalke, "Large-Scale In Situ Fabrication of Voltage-Programmable Dual-Layer High- κ Dielectric Carbon Nanotube Memory Devices With High On/Off Ratio," *IEEE Electron Device Letters*, vol. 29, p. 4, 2008.
- [102] S. J. Tans, M. H. Devoret, H. J. Dai, A. Thess, R. E. Smalley, L. J. Geerligs, and C. Dekker, "Individual single-wall carbon nanotubes as quantum wires," *Nature*, vol. 386, pp. 474-477, 1997.
- [103] J. C. Meyer, M. Paillet, and S. Roth, "Single-molecule torsional pendulum," *Science*, vol. 309, pp. 1539-1541, 2005.
- [104] C. Stampfer, A. Jungen, and C. Hierold, "Fabrication of discrete nanoscaled force sensors based on single-walled carbon nanotubes," *Ieee Sensors Journal*, vol. 6, pp. 613-617, Jun 2006.
- [105] J. Liu, M. J. Casavant, M. Cox, D. A. Walters, P. Boul, W. Lu, A. J. Rimerberg, K. A. Smith, D. T. Colbert, and R. E. Smalley, "Controlled deposition of individual single-walled carbon nanotubes on chemically functionalized templates," *Chemical Physics Letters*, vol. 303, pp. 125-129, 1999.
- [106] P. Hu, A. Fasoli, J. Park, Y. Choi, P. Estrela, S. L. Maeng, W. I. Milne, and A. C. Ferrari, "Self-assembled nanotube field-effect transistors for label-free protein biosensors," *Journal of Applied Physics*, vol. 104, p. 5, Oct 2008.
- [107] H. T. Soh, C. F. Quate, A. F. Morpurgo, C. M. Marcus, J. Kong, and H. J. Dai, "Integrated nanotube circuits: Controlled growth and ohmic contacting of single-walled carbon nanotubes," *Applied Physics Letters*, vol. 75, pp. 627-629, 1999.
- [108] L. Marty, A. Bonhomme, A. Iaia, E. Andre, E. Rauwel, C. Dubourdieu, A. Toffoli, F. Ducroquet, A. M. Bonnot, and V. Bouchiat, "Integration of self-assembled carbon nanotube transistors: statistics and gate engineering at the wafer scale," *Nanotechnology*, vol. 17, pp. 5038-5045, Oct 2006.
- [109] L. Marty, V. Bouchiat, A. M. Bonnot, M. Chaumont, T. Fournier, S. Decossas, and S. Roche, "Batch processing of nanometer-scale electrical circuitry based on in-situ grown single-walled carbon nanotubes," *Microelectronic Engineering*, vol. 61-2, pp. 485-489, Jul 2002.
- [110] L. Marty, A. Iaia, M. Faucher, V. Bouchiat, C. Naud, M. Chaumont, T. Fournier, and A. M. Bonnot, "Self-assembled single wall carbon nanotube field effect transistors and AFM tips prepared by hot filament assisted CVD," *Thin Solid Films*, vol. 501, pp. 299-302, Apr 2006.
-

- [111] L. Marty, V. Bouchiat, C. Naud, M. Chaumont, T. Fournier, and A. M. Bonnot, "Schottky barriers and Coulomb blockade in self-assembled carbon nanotube FETs," *Nano Letters*, vol. 3, pp. 1115-1118, Aug 2003.
- [112] W. Y. Lee, C. H. Weng, Z. Y. Juang, J. F. Lai, K. C. Leou, and C. H. Tsai, "Lateral growth of single-walled carbon nanotubes across electrodes and the electrical property characterization," *Diamond and Related Materials*, vol. 14, pp. 1852-1856, Nov-Dec 2005.
- [113] K. Matsumoto, S. Kinoshita, Y. Gotoh, K. Kurachi, T. Kamimura, M. Maeda, K. Sakamoto, M. Kuwahara, N. Atoda, and Y. Awano, "Single-electron transistor with ultra-high Coulomb energy of 5000 K using position controlled grown carbon nanotube as channel," *Japanese Journal of Applied Physics Part 1-Regular Papers Short Notes & Review Papers*, vol. 42, pp. 2415-2418, Apr 2003.
- [114] L. Rispal, T. Tschischke, H. Yang, and U. Schwalke, "Mass-Production of Passivated CNFETs: Statistics and Gate-Field Dependence of Hysteresis Effect " *ECS Transactions*, vol. 13, p. 6, 2008.
- [115] A. Jungen, S. Hofmann, J. C. Meyer, C. Stampfer, S. Roth, J. Robertson, and C. Hierold, "Synthesis of individual single-walled carbon nanotube bridges controlled by support micromachining," *Journal of Micromechanics and Microengineering*, vol. 17, pp. 603-608, 2007.
- [116] A. Jungen, C. Stampfer, J. Hoetzel, V. M. Bright, and C. Hierold, "Process integration of carbon nanotubes into microelectromechanical systems," *Sensors and Actuators a-Physical*, vol. 130, pp. 588-594, Aug 2006.
- [117] Y. G. Zhang, A. L. Chang, J. Cao, Q. Wang, W. Kim, Y. M. Li, N. Morris, E. Yenilmez, J. Kong, and H. J. Dai, "Electric-field-directed growth of aligned single-walled carbon nanotubes," *Applied Physics Letters*, vol. 79, pp. 3155-3157, Nov 2001.
- [118] E. Joselevich and C. M. Lieber, "Vectorial growth of metallic and semiconducting single-wall carbon nanotubes," *Nano Letters*, vol. 2, pp. 1137-1141, Oct 2002.
- [119] L. X. Zheng, M. J. O'Connell, S. K. Doorn, X. Z. Liao, Y. H. Zhao, E. A. Akhadorov, M. A. Hoffbauer, B. J. Roop, Q. X. Jia, R. C. Dye, D. E. Peterson, S. M. Huang, J. Liu, and Y. T. Zhu, "Ultralong single-wall carbon nanotubes," *Nature Materials*, vol. 3, pp. 673-676, Oct 2004.
- [120] S. M. Huang, M. Woodson, R. Smalley, and J. Liu, "Growth mechanism of oriented long single walled carbon nanotubes using "fast-heating" chemical vapor deposition process," *Nano Letters*, vol. 4, pp. 1025-1028, 2004.

-
- [121] M. Su, Y. Li, B. Maynor, A. Buldum, J. P. Lu, and J. Liu, "Lattice-oriented growth of single-walled carbon nanotubes," *Journal of Physical Chemistry B*, vol. 104, pp. 6505-6508, Jul 2000.
- [122] O. Englander, D. Christensen, and L. W. Lin, "Local synthesis of silicon nanowires and carbon nanotubes on microbridges," *Applied Physics Letters*, vol. 82, pp. 4797-4799, 2003.
- [123] E. O. Sunden, T. L. Wright, J. Lee, W. P. King, and S. Graham, "Room-temperature chemical vapor deposition and mass detection on a heated atomic force microscope cantilever," *Applied Physics Letters*, vol. 88, 2006.
- [124] A. Jungen, C. Stampfer, M. Tonteling, S. Schiesser, D. Sarangi, and C. Hierold, "Localized and CMOS compatible growth of carbon nanotubes on a $3 \times 3 \mu\text{m}^2$ microheater spot," in *13th International Conference on Solid-State Sensors, Actuators and Microsystems*, Seoul, SOUTH KOREA, 2005, pp. 93-96.
- [125] C. Kocabas, H. S. Kim, T. Banks, J. A. Rogers, A. A. Pesetski, J. E. Baumgardner, S. V. Krishnaswamy, and H. Zhang, "Radio frequency analog electronics based on carbon nanotube transistors," *Proceedings of the National Academy of Sciences of the United States of America*, vol. 105, pp. 1405-1409, 2008.
- [126] A. Tselev, K. Hatton, M. S. Fuhrer, M. Paranjape, and P. Barbara, "A photolithographic process for fabrication of devices with isolated single-walled carbon nanotubes," *Nanotechnology*, vol. 15, pp. 1475-1478, 2004.
- [127] N. Hamada, S. Sawada, and A. Oshiyama, "New One-Dimensional Conductors - Graphitic Microtubules," *Physical Review Letters*, vol. 68, pp. 1579-1581, 1992.
- [128] J. W. Mintmire, B. I. Dunlap, and C. T. White, "Are Fullerene Tubules Metallic," *Physical Review Letters*, vol. 68, pp. 631-634, 1992.
- [129] R. Saito, M. Fujita, G. Dresselhaus, and M. S. Dresselhaus, "Electronic-Structure of Chiral Graphene Tubules," *Applied Physics Letters*, vol. 60, pp. 2204-2206, 1992.
- [130] J. C. Charlier, X. Blase, and S. Roche, "Electronic and transport properties of nanotubes," *Reviews of Modern Physics*, vol. 79, pp. 677-732, 2007.
- [131] S. Ilani, L. A. K. Donev, M. Kindermann, and P. L. McEuen, "Measurement of the quantum capacitance of interacting electrons in carbon nanotubes," *Nature Physics*, vol. 2, pp. 687-691, 2006.
- [132] M. J. O'Connell, Ed., *Carbon Nanotubes Properties and Applications*. Boca Raton: CRC Press Taylor & Francis, 2006, p.^pp. Pages.
-

- [133] I. Heller, A. M. Janssens, J. Mannik, E. D. Minot, S. G. Lemay, and C. Dekker, "Identifying the Mechanism of Biosensing with Carbon Nanotube Transistors," *Nano Letters*, vol. 8, pp. 591-595, 2008.
- [134] A. Oberlin, M. Endo, and T. Koyama, "Filamentous Growth of Carbon through Benzene Decomposition," *Journal of Crystal Growth*, vol. 32, pp. 335-349, 1976.
- [135] K. Awasthi, A. Srivastava, and O. N. Srivastava, "Synthesis of carbon nanotubes," *Journal of Nanoscience and Nanotechnology*, vol. 5, pp. 1616-1636, Oct 2005.
- [136] R. Zhang, R. K. Tsui, J. Tresek, A. M. Rawlett, I. Amlani, T. Hopson, and P. Fejes, "Formation of single-walled carbon nanotubes via reduced-pressure thermal chemical vapor deposition," *Journal of Physical Chemistry B*, vol. 107, pp. 3137-3140, Apr 2003.
- [137] T. Kato, G. H. Jeong, T. Hirata, R. Hatakeyama, K. Tohji, and K. Motomiya, "Single-walled carbon nanotubes produced by plasma-enhanced chemical vapor deposition," *Chemical Physics Letters*, vol. 381, pp. 422-426, Nov 2003.
- [138] C. Stampfer, *Electrochemical transducers based on single-walled carbon nanotubes* vol. 1. Tönning: Der Andere Verlag 2007.
- [139] J. Gavillet, A. Loiseau, C. Journet, F. Willaime, F. Ducastelle, and J. C. Charlier, "Root-growth mechanism for single-wall carbon nanotubes," *Physical Review Letters*, vol. 87, Dec 2001.
- [140] X. Fan, R. Buczko, A. A. Puretzky, D. B. Geohegan, J. Y. Howe, S. T. Pantelides, and S. J. Pennycook, "Nucleation of single-walled carbon nanotubes," *Physical Review Letters*, vol. 90, Apr 2003.
- [141] R. S. Wagner and W. C. Ellis, "Vapor-Liquid-Solid Mechanism of Single Crystal Growth (New Method Growth Catalysis from Impurity Whisker Epitaxial + Large Crystals Si E)," *Applied Physics Letters*, vol. 4, pp. 89-&, 1964.
- [142] S. Helveg, C. Lopez-Cartes, J. Sehested, P. L. Hansen, B. S. Clausen, J. R. Rostrup-Nielsen, F. Abild-Pedersen, and J. K. Nørskov, "Atomic-scale imaging of carbon nanofibre growth," *Nature*, vol. 427, pp. 426-429, Jan 2004.
- [143] S. Hofmann, R. Sharma, C. Ducati, G. Du, C. Mattevi, C. Cepek, M. Cantoro, S. Pisana, A. Parvez, F. Cervantes-Sodi, A. C. Ferrari, R. Dunin-Borkowski, S. Lizzit, L. Petaccia, A. Goldoni, and J. Robertson, "In situ observations of catalyst dynamics during surface-bound carbon nanotube nucleation," *Nano Letters*, vol. 7, pp. 602-608, 2007.
- [144] J. Zhao, A. Martinez-Limia, and P. B. Balbuena, "Understanding catalysed growth of single-wall carbon nanotubes," *Nanotechnology*, vol. 16, pp. S575-S581, 2005.

-
- [145] H. W. Zhu, K. Suenaga, A. Hashimoto, K. Urita, K. Hata, and S. Iijima, "Atomic-resolution imaging of the nucleation points of single-walled carbon nanotubes," *Small*, vol. 1, pp. 1180-1183, 2005.
- [146] A. G. Nasibulin, P. Queipo, S. D. Shandakov, D. P. Brown, H. Jiang, P. V. Pikhitsa, O. V. Tolochko, and E. I. Kauppinen, "Studies on mechanism of single-walled carbon nanotube formation," *Journal of Nanoscience and Nanotechnology*, vol. 6, pp. 1233-1246, 2006.
- [147] J. B. Nagy, G. Bister, A. Fonseca, D. Mehn, Z. Konya, I. Kiricsi, Z. E. Horvath, and L. P. Biro, "On the growth mechanism of single-walled carbon nanotubes by catalytic carbon vapor deposition on supported metal catalysts," *Journal of Nanoscience and Nanotechnology*, vol. 4, pp. 326-345, Apr 2004.
- [148] A. Javey, M. Shim, and H. J. Dai, "Electrical properties and devices of large-diameter single-walled carbon nanotubes," *Applied Physics Letters*, vol. 80, pp. 1064-1066, 2002.
- [149] L. M. Wagg, G. L. Hornyak, L. Grigorian, A. C. Dillon, K. M. Jones, J. Blackburn, P. A. Parilla, and M. J. Heben, "Experimental Gibbs free energy considerations in the nucleation and growth of single-walled carbon nanotubes," *Journal of Physical Chemistry B*, vol. 109, pp. 10435-10440, May 2005.
- [150] A. A. Puretzky, D. B. Geohegan, S. Jesse, I. N. Ivanov, and G. Eres, "In situ measurements and modeling of carbon nanotube array growth kinetics during chemical vapor deposition," *Applied Physics a-Materials Science & Processing*, vol. 81, pp. 223-240, 2005.
- [151] A. Monzon, G. Lolli, S. Cosma, S. B. Mohamed, and D. E. Resasco, "Kinetic Modeling of the SWNT Growth by CO Disproportionation on CoMo Catalysts," in *2nd Workshop on Growth Mechanisms of Single-Wall Carbon Nanotubes (SWCNTs)*, Houston, TX, 2007, pp. 6141-6152.
- [152] M. Perez-Cabero, E. Romeo, C. Royo, A. Monzon, A. Guerrero-Ruiz, and I. Rodriguez-Ramos, "Growing mechanism of CNTs: a kinetic approach," *Journal of Catalysis*, vol. 224, pp. 197-205, 2004.
- [153] E. C. Theil, "Ferritin - Structure, Gene-Regulation, and Cellular Function in Animals, Plants, and Microorganisms," *Annual Review of Biochemistry*, vol. 56, pp. 289-315, 1987.
- [154] E. C. Theil, H. Takagi, G. W. Small, L. He, A. R. Tipton, and D. Danger, "The ferritin iron entry and exit problem," *Inorganica Chimica Acta*, vol. 297, pp. 242-251, Jan 2000.
-

- [155] X. F. Liu and E. C. Theil, "Ferritins: Dynamic management of biological iron and oxygen chemistry," *Accounts of Chemical Research*, vol. 38, pp. 167-175, Mar 2005.
- [156] P. M. Harrison and P. Arosio, "Ferritins: Molecular properties, iron storage function and cellular regulation," *Biochimica Et Biophysica Acta-Bioenergetics*, vol. 1275, pp. 161-203, 1996.
- [157] T. Douglas and D. R. Ripoll, "Calculated electrostatic gradients in recombinant human H-chain ferritin," *Protein Science*, vol. 7, pp. 1083-1091, 1998.
- [158] N. D. Chasteen and P. M. Harrison, "Mineralization in ferritin: An efficient means of iron storage," *Journal of Structural Biology*, vol. 126, pp. 182-194, Jun 1999.
- [159] L. Durrer, G. J., T. Helbling, M. Muoth, R. Riek, and C. Hierold. (2009, Narrowing SWNT diameter distribution using size-separated ferritin-based Fe catalysts. *Nanotechnology* 20, 7.
- [160] R. Flückiger, "Self Assembled Integration of Individual Single-walled Carbon Nanotubes towards Large Scale CNFET production," Master Micro and Nanosystems ETH Zürich Zürich, 2008.
- [161] M. Muoth, F. Gramm, K. Asaka, L. Durrer, T. Helbling, C. Roman, S. W. Lee, and C. Hierold, "Tilted-View Transmission Electron Microscopy-Access for Chirality Assignment to Carbon Nanotubes Integrated in MEMS," in *Eurosensor XIII*, 2009.
- [162] A. Jungen, C. Stampfer, L. Durrer, T. Helbling, and C. Hierold, "A method for enhanced analysis of specific as-grown carbon nanotubes," *Physica Status Solidi B-Basic Solid State Physics*, vol. 243, pp. 3138-3141, Nov 2006.
- [163] A. Jungen, V. N. Popov, C. Stampfer, L. Durrer, S. Stoll, and C. Hierold, "Raman intensity mapping of single-walled carbon nanotubes," *Physical Review B*, vol. 75, Jan 2007.
- [164] M. Mattmann, T. Helbling, D. Bechstein, L. Durrer, C. Roman, P. Pohle, M. Fleischer, and C. Hierold, "Hysteresis reduction and dynamic range enhancement of carbon nanotube based NO₂ gas sensors by pulsed gate voltages," in *EuroensorsXIII*, Lausanne, 2009.
- [165] W. Kim, A. Javey, O. Vermesh, O. Wang, Y. M. Li, and H. J. Dai, "Hysteresis caused by water molecules in carbon nanotube field-effect transistors," *Nano Letters*, vol. 3, pp. 193-198, Feb 2003.
- [166] M. Mattmann, C. Roman, T. Helbling, D. Bechstein, L. Durrer, P. Pohle, M. Fleischer, and C. Hierold, "Pulsed gate sweep strategies for hysteresis reduction in

-
- carbon nanotube transistors for low concentration NO₂ gas detection," *submitted to Nanotechnology*, 2009.
- [167] C. Thomsen, S. Reich, and J. Maultzsch, "Resonant Raman spectroscopy of nanotubes," *Philosophical Transactions of the Royal Society of London Series A-Mathematical Physical and Engineering Sciences*, vol. 362, pp. 2337-2359, Nov 2004.
- [168] S. Pisana, A. Jungen, C. Zhang, A. M. Blackburn, R. Sharma, F. Cervantes-Sodi, C. Stampfer, C. Ducati, A. C. Ferrari, C. Hierold, J. Robertson, and S. Hofmann, "Flying and crawling modes during surface-bound single wall carbon nanotube growth," *Journal of Physical Chemistry C*, vol. 111, pp. 17249-17253, 2007.
- [169] A. Jungen, S. Hofmann, J. C. Meyer, C. Stampfer, S. Roth, J. Robertson, and C. Hierold, "Synthesis of individual single-walled carbon nanotube bridges controlled by support micromachining," *Journal of Micromechanics and Microengineering*, vol. 17, pp. 603-608, Mar 2007.
- [170] G. H. Jeong, A. Yamazaki, S. Suzuki, H. Yoshimura, Y. Kobayashi, and Y. Homma, "Cobalt-filled apoferritin for suspended single-walled carbon nanotube growth with narrow diameter distribution," *Journal of the American Chemical Society*, vol. 127, pp. 8238-8239, Jun 2005.
- [171] G. H. Jeong, A. Yamazaki, S. Suzuki, Y. Kobayashi, and Y. Homma, "Behavior of catalytic nanoparticles during chemical vapor deposition for carbon nanotube growth," *Chemical Physics Letters*, vol. 422, pp. 83-88, 2006.
- [172] R. Leturcq, C. Stampfer, K. Inderbitzin, L. Durrer, C. Hierold, E. Mariani, M. G. Schultz, F. Von Oppen, and K. Ensslin, "Franck-Condon blockade in suspended carbon nanotube quantum dots," *Nature Physics*, vol. 5, pp. 327-331, 2009.
- [173] D. Rickwood, Ed., *Preparative Centrifugation* (The Practical Approach Series. Oxford: Oxford University Press, 1992, p.^pp. Pages.
- [174] F. Ding, P. Larsson, J. A. Larsson, R. Ahuja, H. M. Duan, A. Rosen, and K. Bolton, "The importance of strong carbon-metal adhesion for catalytic nucleation of single-walled carbon nanotubes," *Nano Letters*, vol. 8, pp. 463-468, Feb 2008.
- [175] C. R. Henry, "Surface studies of supported model catalysts," *Surface Science Reports*, vol. 31, pp. 235-325, 1998.
- [176] R. L. Vander Wal, T. M. Ticich, and V. E. Curtis, "Substrate-support interactions in metal-catalyzed carbon nanofiber growth," *Carbon*, vol. 39, pp. 2277-2289, 2001.
-

Bibliography

- [177] A. C. Dupuis, "The catalyst in the CCVD of carbon nanotubes - a review," *Progress in Materials Science*, vol. 50, pp. 929-961, Nov 2005.
- [178] P. Atkins, *Physikalische Chemie*, second edition ed. Weinheim: VCH, 1996.

Acknowledgments

I would like to thank my supervisor, Prof. Christofer Hierold, for his confidence and support.

Furthermore I would like to thank Prof. László Forró for acting as a co referee and for reviewing this work.

I would especially like to thank Thomas Helbling, Matthias Muoth, Moritz Mattmann, Shi-Wei Lee, Roman Cosmin, Alain Jungen, Christoph Stampfer and Ronald Grundbacher for the fruitful and supporting collaborations and discussions.

I would like to thank Jason Greenwald, Prof. Roland Riek and Linus Beck for their support in development the ferritin velocity centrifugation technique and the use of their bio-lab facilities and Dominik Leitz for the help by the determination of the reaction kinetics for the SWNT nucleation model.

I would like to thank the support team of CLA-FIRST and FIRST and the users of the CLA-FIRST and FIRST cleanrooms for some useful hints on processing and for support. Further I would like to thank Hansruedi Scherer und Sandro Tiegermann for their straightforward metal evaporation service.

I would like to thank all my students and student assistants who contributed to the progress of this work. They are: Christian Zenger, Ricardo Santos Roque, Matthias Muoth, Jean-Cleaud Tiguely and Ralf Flückiger. I very much appreciated the enjoyable collaboration, which was a great source of motivation for me.

Furthermore I would like to thank for the effort people have done correcting parts of my thesis especially to Tobias Süss, Cosmin Roman, Ronald Grundbacher, Miroslav Hulska, Sonja Huclova, Matthias Muoth. Jason Greenwald and Roswitha Durrer-Loher.

Last but not least I would like to thank all current and former member of the chair of micro and nanosystems and of the Bio-NMR group for support, fruitful discussions and welcome distraction.

Publications

Journal publications as 1st author

- L. Durrer, J. Greenwald, T. Helbling, M. Muoth, R. Riek, and C. Hierold, "Narrowing SWNT diameter distribution using size-separated ferritin-based Fe catalysts," *Nanotechnology*, vol. 20, 2009.
- W. Glatz¹⁷, L. Durrer¹⁷, E. Schwyter, and C. Hierold, "Novel mixed method for the electrochemical deposition of thick layers of $\text{Bi}_{2+x}\text{Te}_{3-x}$ with controlled stoichiometry," *Electrochimica Acta*, vol. 54, pp. 755-762, 2008.
- L. Durrer, T. Helbling, C. Zenger, A. Jungen, C. Stampfer, and C. Hierold, "SWNT growth by CVD on Ferritin-based iron catalyst nanoparticles towards CNT sensors," *Sensors and Actuators B-Chemical*, vol. 132, pp. 485-490, 2008.

Contribution to journal publications

- T. Helbling, C. Hierold, C. Roman, L. Durrer, M. Mattmann, and V. M. Bright, "Long term investigations of carbon nanotube transistors encapsulated by atomic-layer-deposited Al_2O_3 for sensor applications," *Nanotechnology*, vol. 20, 2009.
- B. R. Burg, J. Schneider, M. Muoth, L. Durrer, T. Helbling, N. C. Schirmer, T. Schwamb, C. Hierold, and D. Poulikakos, "Aqueous Dispersion and Dielectrophoretic Assembly of Individual Surface-Synthesized Single-Walled Carbon Nanotubes," *Langmuir*, vol. 25, pp. 7778-7782, 2009.
- M. Mattmann, T. Helbling, L. Durrer, C. Roman, C. Hierold, R. Pohle, and M. Fleischer, "Sub-ppm NO_2 detection by Al_2O_3 contact passivated carbon nanotube field effect transistors," *Applied Physics Letters*, vol. 94, 2009.

¹⁷ Contributed equally

-
- R. Leturcq¹⁷, C. Stampfer¹⁷, K. Inderbitzin, L. Durrer, C. Hierold, E. Mariani, M. G. Schultz, F. von Oppen, and K. Ensslin, "Franck-Condon blockade in suspended carbon nanotube quantum dots," *Nature Physics*, vol. 5, pp. 327-331, 2009.
 - C. Hierold, T. Helbling, C. Roman, L. Durrer, A. Jungen, and C. Stampfer, "Cht Based Sensors," *Smart Materials & Micro/Nanosystems*, vol. 54, pp. 343-349, 2009.
 - W. Glatz, E. Schwyter, L. Durrer, and C. Hierold, "Bi2Te3-Based Flexible Micro Thermoelectric Generator With Optimized Design," *Journal of Microelectromechanical Systems*, vol. 18, pp. 763-772, 2009.
 - T. Helbling, C. Hierold, L. Durrer, C. Roman, R. Pohle, and M. Fleischer, "Suspended and non-suspended carbon nanotube transistors for NO₂ sensing – A qualitative comparison," *physica status solidi (b)*, vol. 245, pp. 2326–2330, 2008.
 - T. Helbling, R. Pohle, L. Durrer, C. Stampfer, C. Roman, A. Jungen, A. Fleischer, and C. Hierold, "Sensing NO₂ with individual suspended single-walled carbon nanotubes," *Sensors and Actuators B-Chemical*, vol. 132, pp. 491-497, 2008.
 - A. Jungen, C. Stampfer, L. Durrer, T. Helbling, and C. Hierold, "Amorphous carbon contamination monitoring and process optimization for single-walled carbon nanotube integration," *Nanotechnology*, vol. 18, 2007.
 - A. Jungen, V. N. Popov, C. Stampfer, L. Durrer, S. Stoll, and C. Hierold, "Raman intensity mapping of single-walled carbon nanotubes," *Physical Review B*, vol. 75, 2007.
 - A. Jungen, L. Durrer, C. Stampfer, C. Roman, and C. Hierold, "Progress in carbon nanotube based nanoelectromechanical systems synthesis," *Physica Status Solidi B-Basic Solid State Physics*, vol. 244, pp. 4323-4326, 2007.
 - A. Jungen, C. Stampfer, L. Durrer, T. Helbling, and C. Hierold, "A method for enhanced analysis of specific as-grown carbon nanotubes," *Physica Status Solidi B-Basic Solid State Physics*, vol. 243, pp. 3138-3141, 2006.
 - E. Szocs, L. Durrer, R. Luginbuhl, N. Simic, A. S. Viana, L. M. Abrantes, R. Keese, and H. Siegenthaler, "STM investigations of Au(111) electrodes coated with vitamin B-12 derivatives," *Surface Science*, vol. 600, pp. 43-55, Jan 2006.
 - J. Rivier, J. Erchegyi, D. Kirby, W. Low, B. Waser, V. Eltschinger, R. Cescato, C. R. R. Grace, L. Durrer, S. C. Koerber, R. Riek, and J. C. Reubi, "DESIGN AND NMR STRUCTURES OF SOMATOSTATIN (SRIF) RECEPTOR-SELECTIVE LIGANDS," *Journal of Peptide Science*, vol. 10, pp. 117-117, 2004.
-

- C. R. R. Grace, L. Durrer, S. C. Koerber, J. Erchegyi, J. C. Reubi, J. E. Rivier, and R. Riek, "Somatostatin receptor 1 selective analogues: 4. Three-dimensional consensus structure by NMR," *Journal of Medicinal Chemistry*, vol. 48, pp. 523-533, Jan 2004

Proceedings and Conference presentations

- L. Durrer, T. Helbling, C. Zenger, A. Jungen, C. Stampfer, and C. Hierold, "SWNT growth by LPCVD on ferritin-based iron catalyst nanoparticles towards CNT sensors," *TRANSDUCERS '07 & Eurosensors XXI. 2007 14th International Conference on Solid-State Sensors, Actuators and Microsystems*, pp. 187-90, 2007.
- L. Durrer, R. Santos-Roque, M. Muoth, T. Helbling, C. Hierold, "Electrochemical formation of Ni and Fe catalyst nanoparticles on thin SiO₂ layers for SWNT growth", 5th ISE spring meeting, Dublin, May 2007.
- T. Helbling, S. Drittenbass, L. Durrer, C. Roman, and C. Hierold, "Ultra small single walled carbon nanotube pressure sensors," *2009 IEEE 22nd International Conference on Micro Electro Mechanical Systems. MEMS 2009*, pp. 575-8, 2009.
- T. Helbling, L. Durrer, C. Roman, V.M. Bright, C. Hierold, "Zero level packaging and long term stability of carbon nanotubes-based transistors in pressure sensors" *EurosensorsXXII*, Deresden, September 2008
- C. Stampfer, A. Jungen, T. Helbling, L. Durrer, and C. Hierold, "Electromechanical Transducers based on Single-Walled Carbon Nanotubes - art. no. 70370E," *Carbon Nanotubes and Associated Devices*, vol. 7037, pp. E370-E370, 2008.
- A. Jungen, J. Gauckler, C. Stampfer, L. Durrer, T. Helbling, and C. Hierold, "Temperature-dependent properties of an individual MEMs-integrated single-walled carbon nanotube," *Mems 2008: 21st IEEE International Conference on Micro Electro Mechanical Systems, Technical Digest*, pp. 733-736, 2008.
- A. Jungen, J. Gauckler, C. Stampfer, L. Durrer, T. Helbling, and C. Hierold, "Temperature-dependent properties of an individual MEMS-integrated single-walled carbon nanotube," *2008 21st IEEE International Conference on Micro Electro Mechanical Systems - MEMS '08*, pp. 733-6, 2007.
- A. Jungen, L. Durrer, C. Stampfer, and C. Hierold, "Nanoscale straining of individual carbon nanotubes by micromachined transducers," *TRANSDUCERS '07 & Eurosensors XXI. 2007 14th International Conference on Solid-State Sensors, Actuators and Microsystems*, pp. 1561-4, 2007.

- T. Helbling, L. Durrer, R. Pohle, C. Stampfer, A. Goyal, M. Fleischer, and C. Hierold, "NO/sub 2/ gas sensors based on individual suspended single-walled carbon nanotubes," *TRANSDUCERS '07 & Eurosensors XXI. 2007 14th International Conference on Solid-State Sensors, Actuators and Microsystems*, pp. 2553-6, 2007.
- C. R. R. Grace, S. C. Koerber, J. Erchegeyi, L. Durrer, J. C. Reubi, J. Rivier, and R. Riek, "Pharmacophore models for subtype-selective analogs of somatostatin (SRIF) based on NMR structures," *Peptides 2004, Proceedings*, pp. 726-727, 2005.

Patents

- L. Durrer, W. Glatz, and E. Schwyter, "Depositing alloy and/or chemical compound on substrate immersed in liquid electrolyte by applying constant or varying potential to substrate under voltage control and then under current control for respective time intervals," EP2072644-A1; WO2009080654-A1, 2009.

